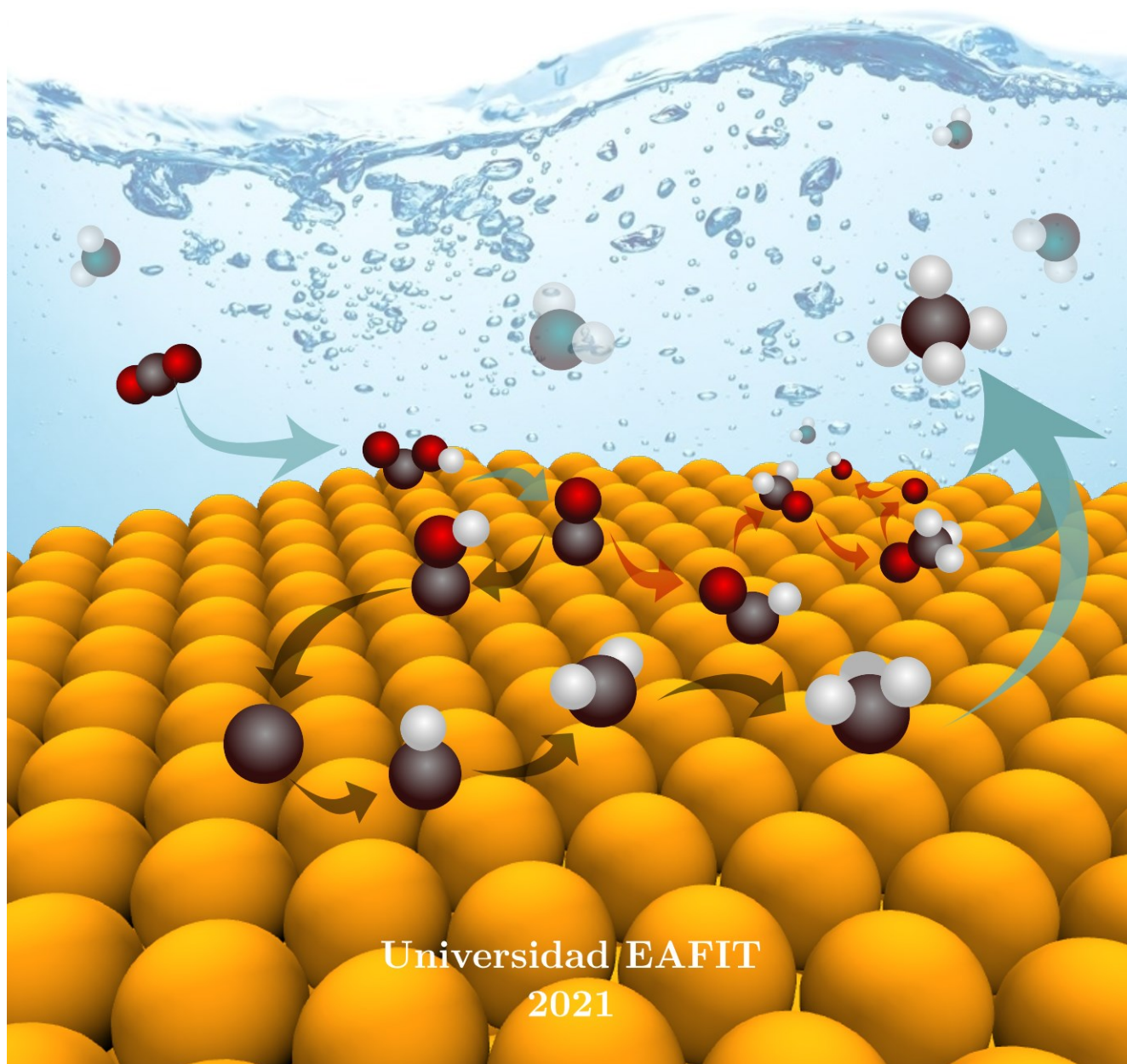


# Improving DFT-based approaches to study CO<sub>2</sub> electroreduction on transition metals

Alejandra Rendón Calle

PhD Thesis



# Improving DFT-based approaches to study CO<sub>2</sub> electroreduction on transition metals

Alejandra Rendón Calle

PhD Thesis



Escuela de Ingeniería  
Universidad EAFIT  
Carrera 49 No 7 sur 50, 050022,  
Medellín, Colombia

February 2021

# Preface

---

This thesis is submitted in candidacy for the PhD degree in Engineering from Universidad EAFIT. The work has been carried out over four years, from 2017 to 2021, at the Departamento de Ingeniería de Procesos, Universidad EAFIT and the Departament de Ciència de Materials i Química Física & Institut de Química Teòrica i Computacional (IQTCUB), Universitat de Barcelona. Financial support was provided by Universidad EAFIT.

Thesis supervisor:           Dr. Santiago Builes Toro  
  Professor at Universidad EAFIT.

Thesis co-supervisor:       Dr. Federico Calle Vallejo  
  Research fellow at Universitat de Barcelona.

## Acknowledgements

---

I would like to express all my gratitude towards my supervisor, Prof. Santiago Builes, who has been my mentor during these seven years working together, and to my co-supervisor, Prof. Federico Calle-Vallejo, who introduced me into the fascinating world of DFT. Without their good guidance and support this thesis would not be possible.

To all members of IQTCUB, Prof. Francesc Illas and Federico, thank you for your hospitality during my visit to Barcelona.

Special thanks to Universidad EAFIT for the invaluable support throughout my career. My life changed completely from the day I was received in such magnificent institution which was my second home for a decade and gave me the opportunity to explore and enjoy all the things I love in life: science, music, and birding.

Special thanks also to my family, my dear parents Luis and Mary, my extraordinary grandmother Adela, my dear Maite and Alberto and my wonderful children Amy and Tom: you are all my motivation, thank you for your help, care and love. Thanks also to my dear friend Elsa, who has always believed in me and encouraged me to pursue my dreams. And finally, thanks to Rafael, my soulmate, the one who makes it all make sense. I dedicate this work to you.

# Abstract

---

The industrial-scale conversion of electricity obtained from renewable sources is crucial to achieve an economy based on renewable energy. In that scenario, the electrochemical reduction of CO<sub>2</sub>, offers the possibility of producing some of the most demanded fuels and chemicals in a sustainable way. However, its efficient implementation on industrial scale is limited by factors as the high energy requirements for the product formation, the low selectivity and efficiency of electrolyzers, and the long-term deactivation of the catalysts. Understanding the many aspects that influence the reaction behavior is a challenging task because, apart from solvent and electrolyte effects, there are multiple intermediates, pathways, and products possible under similar operating conditions. In the recent decades this research field has been highly active in theory and experiments, and many studies have focused on finding the main factors that enhance the reaction performance. In this thesis, the electrochemical CO<sub>2</sub> reduction is studied using state-of-the-art density functional theory (DFT) simulations, incorporating solvation effects as a crucial factor for improving thermodynamic predictions. To this end, a systematic micro-solvation method was developed to determine the number of hydrogen-bonded water molecules in the first solvation shell and the energetic stabilization granted by those hydrogen bonds. The reduction of CO<sub>2</sub> to CO, CH<sub>4</sub> and CH<sub>3</sub>OH on Cu, was considered to test this method, finding very good agreement with experiments without the need to include calculations of reaction kinetics. The estimation of solvation contributions for the CO<sub>2</sub> reduction to CO has been extended to other transition metals such as Ag, Au, and Zn, finding significant variations between solvation corrections for the same adsorbates on different metals and finding very good agreement with experimental results. The increase in accuracy of the predictions make possible the development of a semiempirical method to explain the deactivation evidenced experimentally on Cu electrodes during CO<sub>2</sub>RR to CH<sub>4</sub>.

# Contents

---

<b>Outline .....</b>	<b>9</b>
<b>Chapter 1. Theoretical background .....</b>	<b>11</b>
1.1. Fundamentals of electronic structure calculations .....	11
1.1.1. The many-body problem and the Schrödinger equation .....	11
1.1.2. The Hartree-Fock method (HF) .....	12
1.1.3. Density Functional Theory (DFT) .....	14
1.1.4. Exchange-correlation functionals for DFT .....	17
1.2. Fundamentals of electrocatalysis.....	20
1.2.1. Basic thermodynamics.....	20
1.2.2. Electrocatalytic reactions.....	21
1.2.3. Electrochemical devices .....	22
1.2.4. Standard and reversible hydrogen electrodes .....	24
1.2.5. Computational hydrogen electrode (CHE) .....	24
1.2.6. Free energy calculations and free energy diagrams .....	25
1.2.7. Potential determining step .....	28
1.2.8. Symmetry factor .....	29
1.3. DFT calculations of CO <sub>2</sub> RR using VASP.....	29
1.3.1. Computational details .....	29
1.3.2. Liquid-phase, solvation and gas-phase corrections .....	32
<b>Chapter 2. Electrochemical reduction of CO<sub>2</sub>.....</b>	<b>34</b>
2.1. Reaction mechanism of the CO <sub>2</sub> RR on Cu .....	35
2.2. Scaling relations and volcano plots .....	38
2.3. Structural, pH and cation/anion effects .....	39
2.4. Oxide-derived Cu electrodes .....	41
2.5. Solvation effects .....	42
Summary .....	44

<b>Chapter 3. Developing a systematic micro-solvation method using DFT .....</b>	<b>46</b>
3.1. Adsorbate-water interactions .....	46
3.2. Water self-solvation .....	47
3.3. A decision criterion for adsorbate-water hydrogen bonding .....	50
3.4. Additional details for DFT calculations of the micro-solvation energy using VASP .....	52
Summary .....	53
<b>Chapter 4. Calculations of the CO<sub>2</sub>RR .....</b>	<b>54</b>
4.1. In vacuum CO <sub>2</sub> RR on Cu .....	54
4.2. Micro-solvated CO <sub>2</sub> RR on Cu .....	56
4.3. Micro-solvated CO <sub>2</sub> RR on other transition metals.....	60
4.4. Evaluating dispersion effects.....	64
4.5. Estimation of solvation contributions using DFT energies.....	68
4.6. Evaluation of the work function.....	69
Summary .....	69
<b>Chapter 5. Analysis of the deactivation of Cu catalysts during CO<sub>2</sub>RR to CH<sub>4</sub> .....</b>	<b>70</b>
5.1. Experimental CO <sub>2</sub> RR on polycrystalline and single-crystal Cu facets.....	71
5.2. Combining theory and experiments to analyze Cu deactivation.....	73
Summary .....	77
<b>Conclusions and future directions .....</b>	<b>78</b>
<b>References .....</b>	<b>80</b>

## Outline

---

This thesis is based on the following papers:

P1: A brief review of the computational modeling of CO<sub>2</sub> electroreduction on Cu electrodes.

Rendon-Calle, A., Builes, S., & Calle-Vallejo, F. (2018)

Current Opinion in Electrochemistry, 9, 158-165.<sup>1</sup>

P2: Substantial improvement of electrocatalytic predictions by systematic assessment of solvent effects on adsorption energies.

Rendón-Calle, A., Builes, S., & Calle-Vallejo, F. (2020)

Applied Catalysis B: Environmental, 276, 119147.<sup>2</sup>

P3: How symmetry factors cause potential- and facet-dependent pathway shifts during CO<sub>2</sub> reduction to CH<sub>4</sub> on Cu electrodes.

Rendón-Calle, A., Low, Q. H., Hong, S. H. L.; Builes, S., Yeo, B. S., Calle-Vallejo, F. (2021)

Applied Catalysis B: Environmental, 285, 119776.<sup>3</sup>

P4: A semiempirical method to detect and correct DFT-based gas-phase errors and its application in electrocatalysis.

Granda-Marulanda, L., Rendon-Calle, A., Builes, S., Illas, F., Koper, M. T., & Calle-Vallejo, F. (2020).

ACS Catalysis 10, 12, 6900–6907.<sup>4</sup>

In Chapter 1, an overview of some fundamental concepts behind electronic-structure calculations, introducing the approximations that make calculated values from theoretical studies comparable to electrocatalysis experiments is presented. The second chapter, contains a review of the literature of CO<sub>2</sub>RR on Cu focused in the crucial aspects for improving the computational modelling of this reaction, based on refs.<sup>1-3</sup> The third chapter contains a detailed description of the micro-solvation method proposed on ref.<sup>2</sup>. It includes the analysis of how water molecules interact with each other and how hydrogen bonding with the adsorbed species at the electrochemical interface occurs, alongside the assumptions to make calculations affordable and easy. In Chapter 4, the results of the implementation of the micro-solvation method for CO<sub>2</sub>RR on transition metal electrodes included in<sup>2</sup> are presented. And Chapter 5 contains the analysis of deactivation of Cu electrodes combining theoretical and experimental results. The last chapter contains general conclusions of this work.

# Chapter 1. Theoretical background

---

This chapter briefly describes the theoretical foundations of this thesis. In order to make these topics more accessible and understandable for an engineering audience, some of the models related to quantum chemistry are shown in a simplified way following a more intuitive and pedagogical approach. Interested readers can refer to the sources cited herein for a more rigorous treatment.

## 1.1. Fundamentals of electronic structure calculations

### 1.1.1. The many-body problem and the Schrödinger equation

Quantum mechanics describes with remarkable accuracy many aspects of our universe. In quantum mechanics the particles are not localized at specific points in space, they may behave as classical particles or as classical waves. Thus, systems of particles can be completely described by wave functions that characterize all their measurable properties. Such wave functions are mathematical representations of the quantum states of a particle set, the properties of which correspond to quantum mechanical operators.<sup>5, 6</sup>

The description of a system with  $N$  electrons can be done using the stationary form of the Schrödinger equation,

$$\hat{H}\psi = E\psi, \tag{1.1}$$

where  $\hat{H}$  is the Hamiltonian operator,  $E$  is a constant equal to the energy level, and  $\psi$  is the wave function ( $\psi = \psi(x_1, \dots, x_N)$ , with  $x = \{r, \omega\}$ ) of each one of the spatial ( $r$ ) and spin ( $\omega$ ) coordinates of the  $N$  electrons in the system.

An important assumption to simplify the calculation of wave functions in molecular systems is the Born-Oppenheimer approximation. This approximation considers that the nuclei are considerably heavier and slower than the electrons, so their motion can be treated separately. Thus, the interactions of the  $\hat{H}$  operator can be decoupled as the sum of the kinetic energy for electrons ( $\hat{T}_e$ ), the electron-electron interactions ( $\hat{V}_{ee}$ ), and the electron-nucleus interactions ( $\hat{V}_{en}$ ).<sup>7</sup>

$$\hat{H} = \hat{T}_e + \hat{V}_{ee} + \hat{V}_{en} = \frac{\hbar^2}{2m} \sum_{i=1}^N \nabla_i^2 + \sum_{i=1}^N \sum_{j<i}^N V_{ee}(r_i, r_j) + \sum_{i=1}^N V(r_i) \quad (1.2)$$

Where,  $m$  is the electron mass,  $\hbar$  is the reduced Planck constant, and  $\nabla$  is the Laplacian operator. Within the wave function theory, and following the variational principle, to find the ground-state energy ( $E_0$ ) of electrons we need to pick a trial  $\psi$  that minimizes the expectation value of  $\hat{H}$  over all the antisymmetric  $N$  wave functions:

$$E_0 = \min_{\psi} \langle \psi | \hat{H} | \psi \rangle \quad (1.3)$$

As all the information of the system is contained in such wave function, the resultant problem involves a function of  $3N$  coordinates\*. For this reason, the Schrödinger equation can be solved analytically only in a few cases (e.g. for a free particle, a harmonic oscillator, or a hydrogen atom). In most of the many-body cases, it evolves to a complicated problem where computational methods are required. In the following sections, two of the most common approaches to the many-body problem are described.

### 1.1.2. The Hartree-Fock method (HF)

The Hartree-Fock method is the simplest approach to approximate a solution for the stationary Schrödinger equation.<sup>6</sup> It results after applying the Born-Oppenheimer approximation. To understand it, we can first consider the analytical solution of a

---

\* The wave function depends on three spatial and one spin coordinates for every electron. The latter is neglected in this description. i.e. for a single molecule of  $\text{CO}_2$ , we have a system with 22 e<sup>-</sup> (6 + 8 + 8) and a 66-dimensional wave function.

hydrogen atom (which only has one electron). If we add a second electron to the system ( $H^-$ ), and if we assume that those electrons do not interact with each other, then we would obtain a separable Hamiltonian where  $\widehat{V}_{ee} = 0$ . In HF even larger systems are also assumed to have the same uncorrelated electron movements. For  $N$  electrons the wave function would be as described in (1.4), which is also known as a Hartree product (HP).

$$\psi^{HP}(r_1, \dots, r_N) = \phi_1(r_1), \dots, \phi_N(r_N) \quad (1.4)$$

To introduce the fermionic character of the electrons, this method uses an antisymmetric sum product of single-particle wave functions, the simplest representation of which is a Slater determinant. Such expression changes signs if two electrons are exchanged and disappears if the coordinates or wave functions of two electrons are the same, satisfying in this way the Pauli exclusion principle. Spatial orbitals,  $\phi(r)$ , are replaced with space-spin orbitals  $\chi(x)$  being  $\omega$  a generic spin coordinate, and  $x = \{r, \omega\}$ . Therefore, the Schrödinger equation for each electron becomes:

$$\left[ \frac{\hbar^2}{2m} \nabla^2 + V(r) + V_{HF}(r) \right] \chi_j(x) = E_j \chi_j(x) \quad (1.5)$$

The new term,  $V_{HF}$ , is called the Hartree-Fock potential and describes the average interaction of one of the electrons with the rest.  $V_{HF}$  is defined as follows:

$$V_{HF} = \sum_j J_j - K_j \quad (1.6)$$

where  $J_j$  and  $K_j$  are the Coulomb and exchange operators. In practical calculations, to solve (1.5) we need to define a finite amount of functions, or basis set, to approximate the exact spin orbitals (1.7). Thus, the basis set determines the accuracy and computational time requirements of the calculations.

$$\chi_j(x) = \sum_{i=1}^K \alpha_{j,i} \phi_i(x) \quad (1.7)$$

In (1.7), it is necessary to find the expansion coefficients  $\alpha_{j,i}$ , for  $i = 1, \dots, K$  and for  $j = 1, \dots, N$ , to define all the spin orbitals used in the HF method. However, as the HF is a self-consistent method, an iterative procedure is required to find such solution. Normally, the calculations start making an initial estimate of the spin orbitals (1.7) guessing the expansion coefficients  $\alpha_{j,i}$ , so that an electron density can be defined and the single-electron equations for spin orbitals can be solved. If the spin orbitals found coincide with those guessed at the beginning, then they are solutions, otherwise a new estimate must be made.

With the use of the HF method to solve the Schrödinger equation, the electron exchange is captured: when the coordinates of two or more electrons are exchanged, the wave functions from HF calculations keep the same properties. However, this method does not correctly describe the influence that an electron has over the others (an effect known as correlation), since their wave functions are noninteracting. For that reason, not even when an infinitely large basis set is used, can the energy obtained with HF be identical to that of the true electron wave function.

### 1.1.3. Density Functional Theory (DFT)

Density Functional Theory (DFT) is arguably the most widely used electronic-structure calculation method<sup>7, 8</sup>. Its modern approach arose from the works of Hohenberg, Kohn and Sham<sup>9, 10</sup>. In 1964, Hohenberg and Kohn developed a theorem<sup>9\*</sup> which proved the existence of an exact solution for the ground state of the many-body system based only on the electron density,  $\rho(r)$ . Following the variational principle, the ground state electron density minimizes the energy,  $E[\rho(r)]$ . In other words, the ground state energy

---

\* The Hohenberg-Kohn theorem comprehends two subsidiary theorems which state that: 1) external potentials are determined by the electron density, and 2) for any electron density, the variational principle of the energy is always valid.

( $E_0$ ) is obtained by minimizing the energy over all possible wave functions with density  $\rho(\mathbf{r})$ , and then minimizing over all densities<sup>11</sup>. If the ground state is degenerate (i.e. more than one state has a given energy), then any ground state electron density minimizes the energy.

$$E_0 = \min_{\rho(\mathbf{r})} E[\rho(\mathbf{r})], \quad (1.8)$$

Following the theorem, the energy is a functional of the electronic density,  $E[\rho(\mathbf{r})]$ , which satisfies the relation:

$$E[\rho(\mathbf{r})] = \int v_{\text{ext}}(\mathbf{r})\rho(\mathbf{r})d\mathbf{r} + F[\rho(\mathbf{r})] \quad (1.9)$$

where  $v_{\text{ext}}$  is an external potential ( $\int v_{\text{ext}}(\mathbf{r})\rho(\mathbf{r})d\mathbf{r} = V_{\text{ext}}[\rho(\mathbf{r})]$ ) and  $F[\rho(\mathbf{r})]$  is the universal functional of the density that contains the kinetic energy of the electrons ( $T_e[\rho(\mathbf{r})]$ ), and the non-classical electron-electron interaction energy ( $Q_{ee}[\rho(\mathbf{r})]$ ), so:

$$F[\rho(\mathbf{r})] = \min_{\psi \rightarrow n(\mathbf{r})} \langle \psi | \hat{T}_e + \hat{Q}_{ee} | \psi \rangle \quad (1.10)$$

where the electron density satisfies the following constraints:

$$N = \int \rho(\mathbf{r}) d^3r, \quad \text{with } \rho(\mathbf{r}) \geq 0. \quad (1.11)$$

For a many-electron system with electronic interactions, the electronic energy functional Equation (1.9) can be also defined as:

$$E[\rho(\mathbf{r})] = T_e[\rho(\mathbf{r})] + V_{\text{en}}[\rho(\mathbf{r})] + J_{ee}[\rho(\mathbf{r})] + Q_{ee}[\rho(\mathbf{r})], \quad (1.12)$$

Where  $J_{ee}[\rho(\mathbf{r})]$  is the classical electron-electron repulsion energy, and  $V_{\text{en}}[\rho(\mathbf{r})]$  is the nuclear-electron attraction energy. The terms  $V_{\text{en}}[\rho(\mathbf{r})]$  and  $J_{ee}[\rho(\mathbf{r})]$  can be easily calculated using Equations (1.13) and (1.14) respectively, while  $T_e[\rho(\mathbf{r})]$  and  $Q_{ee}[\rho(\mathbf{r})]$ , (i.e.  $F[\rho(\mathbf{r})]$ ), require approximate solutions.

$$V_{\text{en}}[\rho(\mathbf{r})] = - \sum_{A=1}^M \int \frac{Z_A}{|\mathbf{r} - \mathbf{R}_A|} \rho(\mathbf{r}) d\mathbf{r}, \quad (1.13)$$

$$J_{\text{ee}}[\rho(\mathbf{r})] = \frac{1}{2} \iint \frac{\rho(\mathbf{r}_1)\rho(\mathbf{r}_2)}{r_{12}} d\mathbf{r}_1 d\mathbf{r}_2 \quad (1.14)$$

In summary, the Hohenberg-Kohn theorem is the basis of a quantum theory based on the electron density. It states that since we do not know the functional of the electron density, we can choose a trial electron density and find the correct one by minimizing the energy from the functional. Therefore, the many-body problem is simplified from  $3N$  variables (the sum of the spatial variables of each electron) to only 3 variables (the spatial variables of the electron density). However, the theorem does not give instructions on how to find the universal functional  $F[\rho(\mathbf{r})]$  and, thus, it is not enough to estimate real electronic states.

In 1965, Kohn and Sham created a method (also called KS or KS-DFT)<sup>10</sup> for electronic-structure calculations, developing an exact formulation of the Hohenberg–Kohn theorem. In the KS method, the real system is replaced by a non-interacting electron set with the same electron density, where the independent-electron kinetic energy could be approximated by a single Slater determinant (of orbitals  $\{\psi_i\}$ ):

$$T_s[\{\psi_i\}] = \frac{1}{2} \sum_{i=1}^n \int \psi_i^*(\mathbf{r}) \nabla^2 \psi_i(\mathbf{r}) d\mathbf{r} \quad (1.15)$$

Since  $T_s[\{\psi_i\}] \neq T_e[\rho(\mathbf{r})]$ , the difference between these two terms together with  $Q_{\text{ee}}[\rho(\mathbf{r})]$  can be grouped into what is known as the exchange-correlation functional ( $E_{\text{xc}}[\rho(\mathbf{r})]$ ), which is the only term in the KS method without an analytic definition.

$$E_{\text{xc}}[\rho(\mathbf{r})] = T_e[\rho(\mathbf{r})] - T_s[\{\psi_i\}] + Q_{\text{ee}}[\rho(\mathbf{r})] \quad (1.16)$$

The exchange-correlation potential term,  $V_{\text{xc}}$ , can also be written as:

$$V_{\text{xc}}(\mathbf{r}) = \frac{\delta E_{\text{xc}}(\mathbf{r})}{\delta \rho(\mathbf{r})} \quad (1.17)$$

As mentioned above, in HF the exchange interaction between electrons is treated exactly but their dynamic correlation is neglected since the wave functions are uncorrelated. The main improvement of DFT (KS-DFT) over HF is the approximated treatment of exchange effects and dynamic correlation effects.

Note that in the KS method, as in HF, we also have a self-consistent loop that must be solved iteratively: a trial electron density must be chosen to solve the KS equations, so as to find their single-particle wave functions. Subsequently, the electron density can be calculated from those wave functions. If they are the same<sup>\*</sup>, the ground state electron density is found, otherwise, the trial electron density must be modified in an iterative process until the electron density is found.

#### 1.1.4. Exchange-correlation functionals for DFT

The exchange-correlation energy,  $E_{xc}[\rho(\mathbf{r})]$ , can be defined as the difference between classical and quantum mechanical electron-electron repulsion. To some extent, this term corrects the electron density of  $N$  non-interacting electrons to the same electron density of the true interacting system. Since its exact form remains unknown, approximate functionals are necessary to describe it.<sup>8, 12</sup> Importantly, the consistency and reliability of the data obtained from DFT mainly depends on the approximation chosen.

Kohn and Sham<sup>10</sup> proposed the first and simplest approximation to the exchange correlation energy functional: the local-density approximation (LDA). This approximation assumes that  $E_{xc}^{LDA}$  at a specific density of the inhomogeneous electron gas is the same as that of the homogeneous gas of the same density, and that such density is identical everywhere.

$$E_{xc}^{LDA} = \int \epsilon_{xc}^{hom}(\rho(\mathbf{r}))\rho(\mathbf{r})d^3r. \quad (1.18)$$

---

<sup>\*</sup> For approximate numerical solutions, a tolerance is required to establish how close the results are in order to be considered as “the same”. The lower the tolerance, the more iterations it takes to converge.

The term inside the integral is the exchange-correlation energy per particle of a homogeneous electron gas. Its generalization to include uniform spin densities (LSDA) is given by:

$$E_{xc}^{LSDA} = \int \epsilon_{xc}^{hom}(\rho_{\uparrow}, \rho_{\downarrow}) \rho(\mathbf{r}) d^3\mathbf{r}. \quad (1.19)$$

However, there are two main limitations in LDA: i) in a real molecular system the electron density is not uniform, so that there are peaks in the density at the nucleus. ii) the exchange correlation correction does not cancel the self-interaction term.<sup>5</sup> As a result, LDA usually overestimates the correlation term and underestimates the exchange energy<sup>13</sup>. Although it gives sufficiently accurate results for solid-state systems, it tends to overestimate the binding energy of molecules. In any case, the development of LDA was the first step that motivated the making of more sophisticated approximations to the exchange-correlation energy, such as the generalized gradient approximation (GGA) and the hybrid functionals.

The GGA, is a semi-local method where the exchange correlation term depends on the local gradient of the electron density<sup>14</sup> (1.20). Since there are many ways to include the gradient of the electron density in  $\epsilon_{xc}^{GGA}$ , there are many distinct GGA functionals, being the most common the Perdew-Wang 91 (PW91)<sup>15</sup>, the Perdew–Burke–Ernzerhof (PBE)<sup>16, 17</sup>, and its revised version (RPBE)<sup>18</sup>.

The GGA functionals significantly enhance the description of many-electron systems, and reduce the overbinding in molecules found with LDA<sup>19</sup>. Their versatility in the description of molecules and solid surfaces both separately and in adsorbed systems, combined with an affordable computational cost, make GGA functionals appropriate for interface calculations. For this reason, we employ them in this work.

$$E_{xc}^{GGA} = \int \epsilon_{xc}^{GGA}(\rho_{\uparrow}, \rho_{\downarrow}, \nabla\rho_{\uparrow}, \nabla\rho_{\downarrow}) \rho(\mathbf{r}) d^3\mathbf{r}. \quad (1.20)$$

In the search for more accurate functionals, other non-local approximations such as the meta-GGA<sup>20, 21</sup> (M-GGA) appeared. To calculate  $E_{xc}$ , M-GGA functionals include Laplacians of the electron density and the kinetic energy density,  $\tau(\mathbf{r})$ :

$$\tau(\mathbf{r}) = \frac{1}{2} \sum_i^{\text{occ}} |\nabla\psi_i(\mathbf{r})|^2 \quad (1.21)$$

Hybrids are another class of exchange-correlation functionals, in which a fraction of the exact exchange energy is included along with the correlation energy from GGAs. The most common hybrid functionals are PBE0 (with PBE and HF exchange energy)<sup>22</sup>, B3LYP (Becke exchange and Lee–Yang–Parr correlation)<sup>23, 24</sup>, and HSE (Heyd–Scuseria–Ernzerhof)<sup>25</sup>. Hybrid functionals improve the GGA predictions of molecular properties such as the bond-length, vibration frequencies, and atomization energies.

In range-separated hybrid functionals the electron–electron interaction is divided into two terms: short- and long-range. These hybrid functionals have demonstrated to be highly accurate for systems where long-range interactions, such as van der Waals (vdW) forces, are influential; i.e. aqueous systems.<sup>26-28</sup> Furthermore, in the random-phase approximation (RPA),<sup>29</sup> which uses unoccupied Kohn-Sham orbitals, the electron exchange is not approximated. RPA is a fully nonlocal approach that automatically includes long-range van der Waals interactions<sup>30</sup>.

However, it is important to note that for local or semi-local approaches, the KS equations can be swiftly solved using codes with plane-wave basis sets implementations, while the introduction of the non-local exact exchange in hybrid functionals causes a significant increase in numerical complexity, so that localized basis sets are more advisable<sup>6</sup>.

In the seek for the optimal functional for electronic-structure calculations, one we could call “universal”, many approaches have been proposed over the years. In a peculiar attempt to classify those functionals, Perdew<sup>31</sup> used the concept of Jacob’s ladder\*. The HF method is the earth on which the ladder stands, the rungs are the ingredients

---

\* Jacob’s ladder is a ladder leading to heaven described in Genesis 28:10–19.

included in the different DFT functionals, ordered hierarchically by their complexity and accuracy. Heaven is the chemical accuracy\*. Schematics of this ladder are shown in Figure 1.1.

However, it is important to note that the inclusion of more sophisticated ingredients does not necessarily guarantee an overall, systematic improvement in the accuracy of DFT<sup>32</sup>.

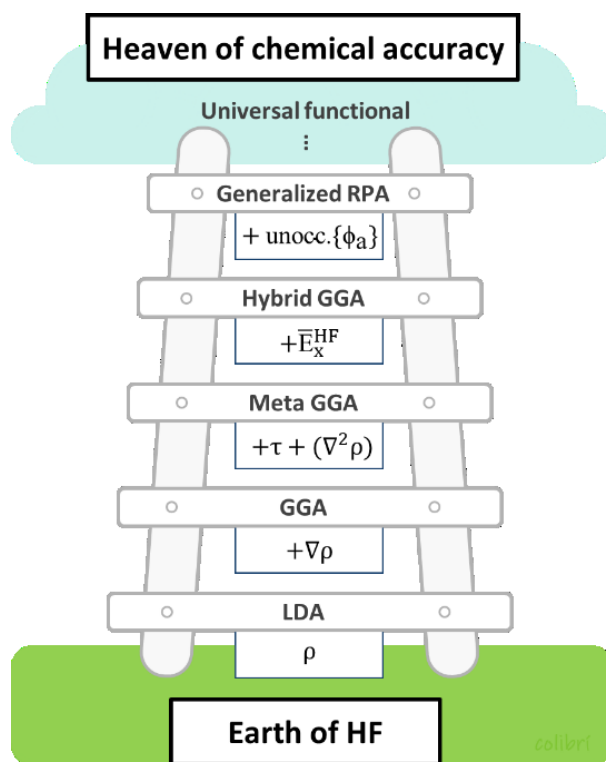


Figure 1.1. Jacob's ladder of the elements in the development of exchange-correlation functionals<sup>16</sup>.

## 1.2. Fundamentals of electrocatalysis

### 1.2.1. Basic thermodynamics

The second law of thermodynamics establishes that the entropy ( $S$ ) of an isolated system cannot decrease with time. This thermodynamic property dictates the direction

\* The accuracy required for chemical predictions to be considered realistic (0.041 eV).

of spontaneous processes. To some extent, it also accounts for the direction of time in the universe. According to the second law, if we consider a reacting system, the reaction will occur only if the sum of the entropy changes of the system and its surroundings is not negative.

Nevertheless, evaluating all the time the entropy of the universe is impractical. Instead, we can use the Gibbs energy (G) which is a property of state that depends on the entropy (S) and the enthalpy (H) of the system (not of the surroundings). Formally, G indicates the maximum energy that can be extracted from the system and used to do work at constant pressure (P) and temperature (T). But, like S, Gibbs energy can be used also as an indicator of the direction of spontaneous changes, with the advantage that it only depends on properties of the system and not on the surroundings. For a chemical reaction, a negative Gibbs energy change ( $\Delta G < 0$ ) between products and reactants at constant P and T indicates that the reaction is spontaneous, or exergonic.

### 1.2.2. Electrocatalytic reactions

Electrochemical reactions require the transfer of electrons to or from a species at an interface between an electronic conductor (electrode) and an ionic conductor (electrolyte). In these reactions, solids (often metals) are used as electrodes and at the same time as catalysts. Catalysts are species that modify the reaction pathway and normally such new pathways have lower activation energies. The catalyst are not consumed during the reaction\* and they can be used repeatedly to drive some non-spontaneous (or endergonic) processes or to accelerate the slow ones.<sup>18</sup>

A large portion of the electrochemical reactions that are currently studied involve the simultaneous transfer of protons and electrons. Each transfer constitutes a reaction step, leading to a series of reaction intermediates until the final products are obtained.

---

\* This statement is only valid in ideal cases. Deactivation of the catalysts by poisoning or degradation is one of the main challenges for implementation of electrocatalytic processes in the industrial scale.

The Sabatier principle states that the best catalyst is one that binds the key intermediates neither too strongly nor too weakly<sup>33</sup>. And such “moderate” interaction opens energetically favorable reaction pathways that simultaneously avoid catalytic inertness and poisoning.

### 1.2.3. Electrochemical devices

Electrochemical devices transform chemical bonds into electricity and vice versa. In fuel cells, an electric current is produced by an exergonic chemical reaction. In electrolyzers, the electrical energy is turned into chemical energy through an endergonic reaction caused by an externally supplied current.<sup>34</sup> A general schematic of an electrolyzer is provided in Figure 1.2.

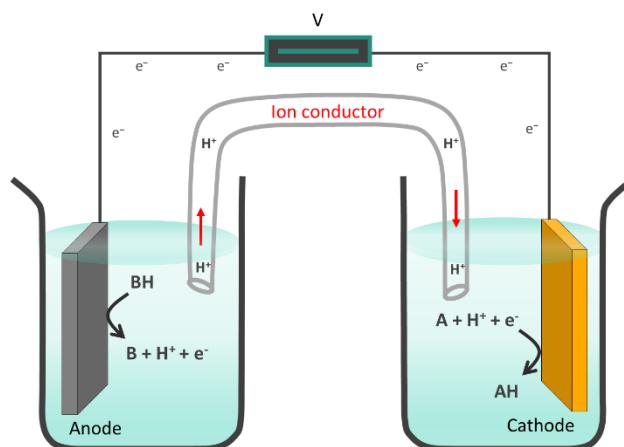
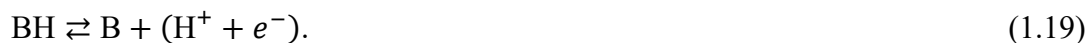


**Figure 1.2.** Schematics of an electrochemical cell. **A** and **BH** are the reactants of a redox reaction which produces **AH** and **B**. The anode is the electrode where the oxidation takes place, and the reduction reaction happens at the cathode. The two electrodes can be separated at an arbitrary distance, and the reactions can be reversed varying the external potential applied.

Following the notation in Figure 1.2, where **A** and **BH** are reactants of a redox reaction that produces **AH** and **B**, the overall electrochemical reaction is:



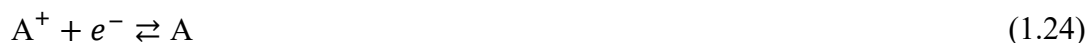
where reactions that take place in the cathode (reducing electrode) and in the anode (oxidizing electrode) are given respectively as:



As mentioned above, these electrochemical reactions normally involve multiple elementary steps separated by coupled or decoupled proton-electron transfers between reaction intermediates. In aqueous solutions, proton-electron coupled reactions can only occur at the electrode surface. As an example, consider the adsorption of A on a surface site \*, and its first and second reduction steps via coupled proton-electron transfers are:



However, in electrochemical processes reactions can also take place at the interface, or in the electrolyte. In the electrolyte, the pH of the environment determines the acid-base or ionization reactions. Reactions involving decoupled proton-electron transfers can be written, for example, as:



At the interface, reactions may deviate from the ideal proton-electron coupled transfers, as they are influenced by both the potential and pH, and they also depend on the size of the adsorbed intermediate species.

#### 1.2.4. Standard and reversible hydrogen electrodes

To compare the performance of a catalyst through experiments, a proper reference is necessary. A reference electrode is an electrode with a stable and well-known equilibrium potential. One of the most common reference electrodes is the standard hydrogen electrode (SHE). At 25°C, it has an absolute potential of  $4.44 \pm 0.02$  V<sup>35</sup>. However, to establish a basis for the thermodynamic scale of oxidation-reduction potentials, it is arbitrarily set to 0 V at any temperature in the so-called SHE scale.

Experimentally, platinum electrodes are often used because the redox reaction of hydrogen shows fast kinetics and quickly reaches the equilibrium on these electrodes.



However, the activity of protons changes with pH. Therefore, to be able to compare catalysts at different pH, a different thermodynamic scale is required. The reversible hydrogen electrode (RHE) is a hydrogen electrode the potential of which changes with the pH. The potentials (U) of these two reference electrodes are correlated by:

$$U_{\text{RHE}} = U_{\text{SHE}} - 0.059 \text{ V} \cdot \text{pH} \quad (1.26)$$

#### 1.2.5. Computational hydrogen electrode (CHE)

Atomic-scale calculations of the electrochemical interface, employing DFT and using the computational hydrogen electrode (CHE)<sup>36</sup> allow screening over numerous materials and active sites from a thermodynamic perspective. The CHE provides a simple way to evaluate the energy of protons and electrons using that of  $\text{H}_{2(g)}$ , avoiding the explicit treatment of solvated proton-electron pairs by considering their equilibrium with molecular hydrogen in solution (equation 1.25) at 1 atm and 0 V, for all values of pH and temperature.

The CHE model assumes that the bulk of the electrolyte and the electrodes are in equilibrium themselves and with the surface. It also considers the adsorption energy is relatively independent on the electrostatic field.

The chemical potential ( $\mu$ ) of a proton-electron pair in equilibrium can be simply described as in Equation (1.27). For systems in equilibrium, this potential is also equivalent to the partial molar Gibbs energy.

$$\mu_{\text{H}^+}^{\text{ref}} + \mu_{e^-}^{\text{ref}} = \frac{1}{2} \mu_{\text{H}_2(\text{g})} \quad (1.27)$$

where the superscript ref stands for  $\mu$  at the reference electrode. At any pH,  $\mu_{e^-}$  is related to  $\mu_{e^-}^{\text{ref}}$  through the potential difference between the working and the reference electrode ( $U_{\text{RHE}}$ ), and the electron charge ( $e$ ).

$$\mu_{e^-}^{\text{ref}} = \mu_{e^-} + eU_{\text{RHE}} \quad (1.28)$$

Since in the CHE the protons in the electrolyte are in equilibrium with the protons in the reference electrode ( $\mu_{\text{H}^+}^{\text{ref}} = \mu_{\text{H}^+}$ ):

$$\mu_{\text{H}^+} + \mu_{e^-} = \frac{1}{2} \mu_{\text{H}_2(\text{g})} - eU_{\text{RHE}} \quad (1.29)$$

The energies calculated within this approach are merely based on thermodynamics and presuppose that (i) protonation kinetic barriers are surmountable at room temperature, (ii) kinetics and thermodynamics are proportional (i.e. that they follow Brønsted-Evans-Polanyi relations<sup>37, 38</sup>), and (iii) that the final states of uphill electrochemical steps are commensurate with the corresponding transition states<sup>39</sup>.

This method allows for a consistent evaluation of the free energies of all species involved in an electrochemical reaction network.

### 1.2.6. Free energy calculations and free energy diagrams

DFT simulations of electrochemical systems are normally performed in vacuum, mainly due to the high computational cost that the simulation of the electrolyte implies.

Using DFT, the binding energy ( $\Delta E_{\text{DFT}}$ ) and the corresponding reaction of an adsorbate A on a surface site \* in vacuum, is obtained as follows:

$$\Delta E_{\text{DFT}} = E_{*A} - E_* - E_{A(\text{g})}, \quad (1.30)$$



The Gibbs energy of adsorption for such adsorbate can be defined as:

$$\Delta G = \Delta E_{\text{DFT}} + \Delta E_{\text{ZPE}} - T\Delta S + \int_0^T C_p dT, \quad (1.32)$$

where  $\Delta E_{\text{ZPE}}$  is the change in zero-point energy,  $T\Delta S$  stands for the entropy contributions extrapolated to standard conditions of temperature (298.15 K), and  $\int_0^T C_p dT$  is the enthalpy change between 0 and T. The latter term is typically neglected, since it has been shown that its contribution from 0 to 298.15 K does not significantly modify the adsorption energies<sup>40</sup>.

$\Delta E_{\text{DFT}}$  is obtained from Equation (1.30) using a conjugate gradient or a quasi-Newton algorithm to minimize the energies of initial and final states of the system respect to the nuclei coordinates (see Figure 1.3).  $\Delta E_{\text{ZPE}}$  of adsorbed species is calculated from the vibrational frequencies around the ground state within the harmonic oscillator approximation. For adsorbates only the vibrational contributions to the entropy are normally considered,  $\Delta S = \Delta S_{\text{vib}}$  at 298.15 K. For gases and liquids zero-point energies are determined using the harmonic oscillator approximation, and  $\Delta S$  corresponds to the total entropies taken from thermodynamic tables at 298.15 K and 1 atm ( $TS^0$ )<sup>41</sup>. The Gibbs energies of the bulk crystals are  $\Delta G \approx \Delta E_{\text{DFT}}$ , assuming that entropic contributions and zero-point energies are negligible in this kind of systems<sup>42</sup>. (In section 1.3, further details about DFT calculations are provided).

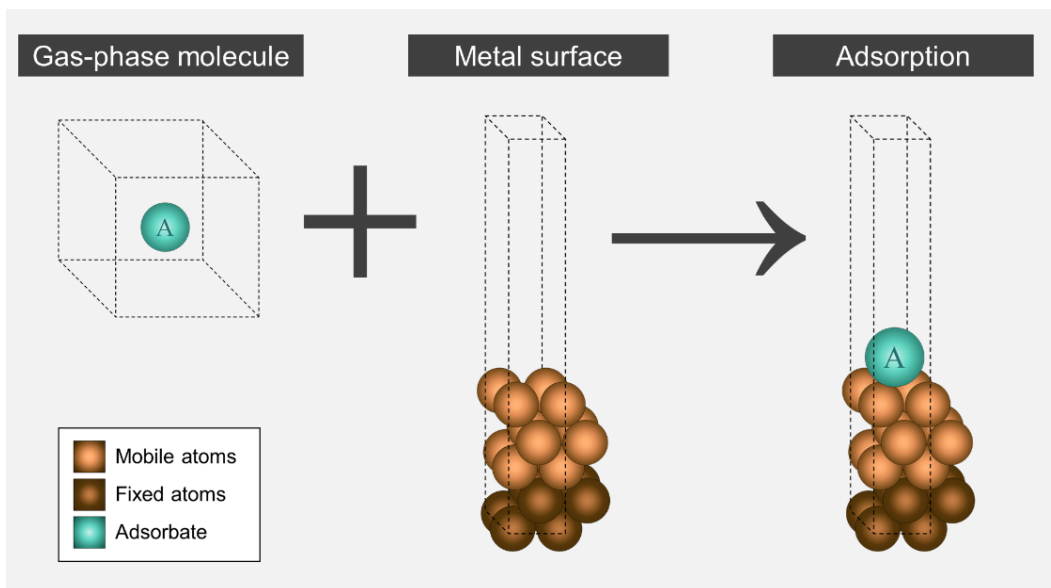


**Figure 1.3.** Schematics of the systems involved in calculations of  $\Delta E_{\text{DFT}}$  term in Equation (1.32).

For an electrochemical reaction with  $n$  proton-electron coupled transfers (where the chemical potential of the proton depends on the pH, and the chemical potential of the electron depends on the applied potential), the Gibbs energy change can be calculated by adding equations 1.29 and 1.32.

$$\Delta G(n, U_{\text{RHE}}) = \Delta E_{\text{DFT}} + \Delta E_{\text{ZPE}} - T\Delta S - n \cdot \left( \frac{1}{2} \mu_{\text{H}_2(\text{g})} - eU_{\text{RHE}} \right) \quad (1.33)$$

Taking the  $\text{CO}_2$  reduction reaction to  $\text{CO}_{(\text{g})}$  as an example, the reaction proceeds through  $^*\text{COOH}$  and  $^*\text{CO}$  intermediates. The corresponding elementary reactions can be written respect to the initial reactant as follows:



$\text{CO}_2$  reduction to  $\text{CO}$  is followed by the desorption of  $^*\text{CO}$  ( $^*\text{CO} \rightarrow ^* + \text{CO}_{(\text{g})}$ ), which is not an electrochemical step. Thus, considering this mechanism and evaluating the Gibbs energy (equation 1.33) for each step with respect to the reactant (indicated by

equations 1.34 and 1.35), we can build a free-energy diagram where the energy profile of each possible reaction pathway is analyzed and compared. An example of a conventional energy profile is provided in Figure 1.4.

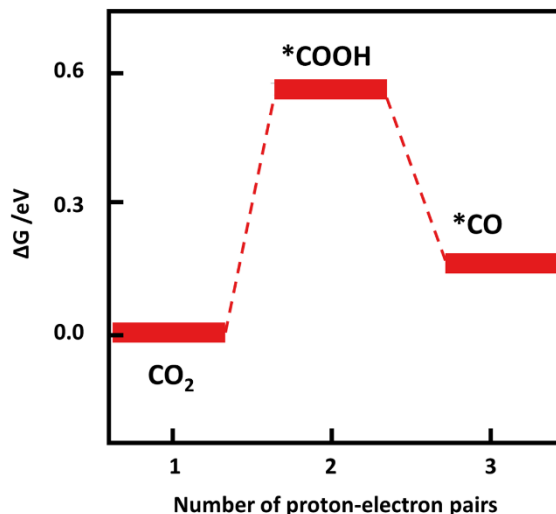


**Figure 1.4.** Energy profile for the CO<sub>2</sub> electroreduction reaction to \*CO on Cu(100)

The Gibbs energy difference between subsequent elementary steps can be calculated by rewriting equations (1.34) and (1.35) as follows:



Some experimental studies also suggest an alternative pathway for CO<sub>2</sub> reduction to CO where CO<sub>2</sub> is first activated by an electron transfer before adsorption, and then a hydrated cation close to the surface stabilizes the adsorbed species<sup>43-47</sup>. However, modeling such a decoupled proton-electron transfer is challenging from a DFT standpoint.

### 1.2.7. Potential determining step

The onset potential ( $U_{\text{onset, DFT}}$ ) along a given reduction reaction pathway is the additive inverse of the largest positive free energy  $\Delta G_{\text{max}}$  among all electrochemical steps<sup>36</sup>.

$$U_{\text{onset, DFT}} = -\Delta G_{\text{max}}/e \quad (1.35)$$

### 1.2.8. Symmetry factor

The symmetry factor,  $\beta_i$ , is a concept used for single-electron transfer steps in an electrochemical reaction. It is a number between 0 and 1 defined as the fraction of the electrostatic potential energy affecting the reaction rate.<sup>48, 49</sup> For example, for \*A hydrogenation,  $\beta_i$  is the fractional electron charge transferred up to the transition state (TS<sub>*i*</sub>), being *i* the hydrogenation product:



The potential-dependent Gibbs energy required to reach the transition state ( $\Delta G_{A \rightarrow TS_i}^\#$ ), is given by a constant value calculated at 0 V vs RHE ( $\Delta G_{TS_i} - \Delta G_A$ ) and a correction ( $\beta_i eU$ ) that accounts for the contribution to the Gibbs energy of the applied potential (U), (1.37). Experimentally, it is common to assume  $\beta = 0.5$ .

$$\Delta G_{A \rightarrow TS_i}^\# = \Delta G_{TS_i} - \Delta G_A + \beta_i eU \quad (1.37)$$

## 1.3. DFT calculations of CO<sub>2</sub>RR using VASP

### 1.3.1. Computational details

In this thesis the DFT calculations were performed using the Vienna Ab initio Simulation Package (VASP)<sup>50</sup>. The relaxations of the atoms were done until the maximum force on any atom was below 0.05 eV/Å, within the generalized-gradient-approximation (GGA) using the Perdew-Burke-Ernzerhof (PBE) as exchange-correlation functional, with a plane-wave cutoff of 450 eV. The ionic cores of the atoms were described by Projector Augmented Wave (PAW) potentials<sup>50</sup>, and the Methfessel-

Paxton method was used to smear the Fermi level<sup>51</sup> with an electronic temperature of 0.2 eV.

A comprehensive screening of different adsorption sites, rotations and conformers, for all intermediate adsorbed species on each metal (Cu, Ag, Au, and Zn) and facet ((100), (110) and (111) crystal surfaces) was done. From each of these sites and configurations an energy value was obtained, but only the minimum was associated to the ground-state Gibbs energy of Equation (1.32). An example of the different configurations calculated for CH<sub>2</sub> is shown in Figure 1.5.

Optimized lattice parameters in Table 1.1 were used to build the metal slabs, formed by four atomic layers with their two bottom layers fixed in all cases. The (110) facet was modeled with a missing row in the upper layer, corresponding to its commonly observed reconstruction<sup>52</sup>. As shown in Figure 1.5, periodic cells of 2×2 for (111) and (100), and 3×2 for (110) were used, keeping at least 14 Å between slabs. Dipole corrections were applied in the vacuum direction.

**Table 1.1.** Lattice parameters optimized using PBE for the metals included in this study, and their corresponding experimental values<sup>53</sup>. \*Although Zn is an hcp metal, we calculated Zn(0001) and fcc Zn(211), as a proxy to a Zn stepped surface.

Metal	Lattice parameter ( $a$ ) [Å]	
	PBE	Experimental
Cu	3.64	3.61
Au	4.17	4.08
Ag	4.16	4.09
Zn	3.77	*

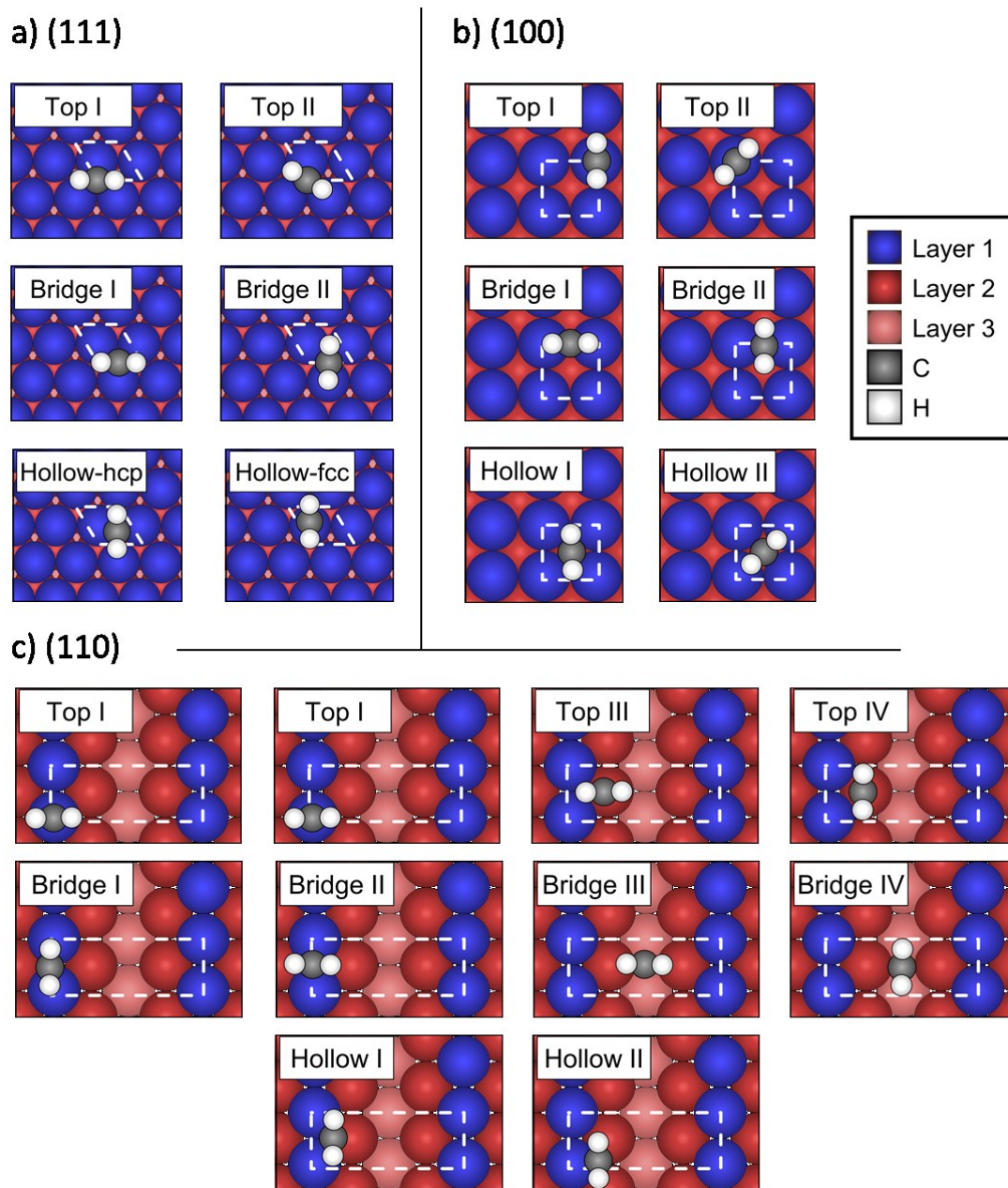


**Figure 1.5.** Top views of inequivalent adsorption sites and configurations on the three different facets included in this study. An adsorbed  $\text{CH}_2$  is used as an example. White dashed lines indicate the unit cell of each facet. After calculating all the possibilities, the site with the lowest DFT energy is the one taken as the ground state for in vacuum adsorption.

### 1.3.2. Liquid-phase, solvation and gas-phase corrections

In order to simulate bulk liquids using DFT, large cells with numerous explicit atoms are commonly required. This is computationally expensive and impractical. However, liquid species are inherently present in electrochemical reactions and it is necessary to account for their contributions correctly. For example, in the electrochemical reduction of CO<sub>2</sub> (CO<sub>2</sub>RR), we have liquid products (such as HCOOH, CH<sub>3</sub>CH<sub>2</sub>OH, and CH<sub>3</sub>OH) and an aqueous media where the reactions take place. For liquid water a common practice is to calculate the DFT energy of H<sub>2</sub>O<sub>(g)</sub> and subsequently add an entropic correction to determine the free energy of H<sub>2</sub>O<sub>(l)</sub><sup>36, 41, 54</sup>. Such liquid-phase correction is calculated through a semiempirical approach combining experimental data and DFT results. (See more details in references<sup>36, 41, 54</sup>). Note that the TS<sup>0</sup> correction of 0.67 eV in Table 1.2 for H<sub>2</sub>O<sub>(l)</sub> is neither that of liquid (0.22 eV) nor gas-phase water (0.58 eV). The same correction is done for other liquid products, as CH<sub>3</sub>OH<sub>(l)</sub>.

Moreover, as the reaction takes place in an aqueous media, interfacial water may modify the adsorption energies of the reaction intermediates. When in vacuum DFT simulations are performed, it is necessary to consider the additional stabilization that water may provide to the adsorbates by virtue of hydrogen bonding. Commonly, solvation corrections are added to energies obtained from calculations in vacuum. Such corrections are often called “ad hoc solvation corrections” and have been widely applied in mechanistic DFT studies<sup>36, 39, 54-60</sup>. Ad hoc solvation schemes are described by (1.37). Their accuracy mostly depends on how rigorously they were estimated for the particular systems.

$$\Omega_A = \Delta G_A^{solution} - \Delta G_A^{vacuum} \quad (1.37)$$

As the calculation of solvation corrections is one of the main topics of this dissertation, a complete discussion about other available solvation methods can be found in section 2.5. A detailed description of the solvation method developed in this work is provided in chapter 3.

It is well known that GGA functionals are advisable for modeling bulk metals and slabs, and hybrid functionals are advisable for molecules and solids with localized electrons<sup>61, 62</sup>. However, in electrochemical systems, metals and molecules interact with each other and must be simulated within the same DFT framework. For this reason, depending on the exchange-correlation functional used it is often necessary to apply suitable corrections.

Using GGAs, and considering the CO<sub>2</sub>RR intermediates, gas-phase corrections to the total energy of CO<sub>2</sub>, CO and CH<sub>3</sub>OH were applied in this work and are shown in Table 1.2.

**Table 1.2.** Zero-point energies, entropy contributions and gas-phase corrections (GPC) to the total energy for the fluid-phase species involved in the CO<sub>2</sub>RR to C<sub>1</sub> products. Corrections applied in this work were reported in<sup>39, 54, 63</sup>. All values are in eV.

Molecule	E <sub>ZPE</sub>	TS <sup>0</sup>	GPC
CO <sub>2(g)</sub>	0.31	0.66	0.19
H <sub>2(g)</sub>	0.27	0.40	-
H <sub>2</sub> O <sub>(l)</sub>	0.57	0.67	-
CH <sub>4(g)</sub>	1.19	0.58	-
CO <sub>(g)</sub>	0.14	0.61	-0.24
CH <sub>2</sub> O <sub>(g)</sub>	0.71	0.68	-
CH <sub>3</sub> OH <sub>(l)</sub>	1.36	0.79	0.04

A semiempirical procedure for detecting gas-phase errors based on the formation energies of reactants and products calculated with DFT was proposed in P4<sup>4</sup>. The results provided later in chapters 4 and 5 were used to test such method. With the use of the improved gas-phase corrections, it was shown that the accuracy and descriptiveness of DFT models for CO<sub>2</sub>RR increase considerably.

## Chapter 2. Electrochemical reduction of CO<sub>2</sub>

---

The electrochemical CO<sub>2</sub> reduction reaction (CO<sub>2</sub>RR) to hydrocarbons is a promising catalytic process. Copper (Cu) is well known for its singular ability to catalyze this reaction<sup>64</sup> toward a variety of hydrocarbons, fuels, alcohols and chemical feedstocks of up to five C atoms, such as methane, ethylene, ethanol and 1-propanol<sup>65-67</sup>. This process stands as an alternative to decrease atmospheric CO<sub>2</sub> levels and achieve the much-desired carbon-neutral cycle for chemical and fuel synthesis, provided that the process is efficient enough and its input energy comes from renewable sources. The large-scale implementation of CO<sub>2</sub>RR would have the advantage of producing fuels with low carbon footprint, while keeping the existing fossil-fuel infrastructure<sup>68, 69</sup>.

Since Hori and co-workers<sup>70</sup> first showed that CO<sub>2</sub>RR to hydrocarbons and alcohols was feasible on Cu surfaces, electrodes based on Cu and similar materials have been extensively studied<sup>68, 71-73</sup>. Initially, experimental studies focused on elucidating the CO<sub>2</sub> reaction mechanism on Cu electrodes by detecting reaction products.<sup>66, 74-76</sup> Using spectroscopy, some authors identified \*CO<sup>77</sup>, its hydrogenated dimer<sup>44</sup> and acetaldehyde<sup>78</sup> as products. More recently, Jaramillo et al<sup>67</sup> reported 16 different CO<sub>2</sub>RR products among C<sub>1</sub>, C<sub>2</sub> and C<sub>3</sub> species.

Beside the many possible products, it is known that the reaction is also affected by factors such as the catalysts' structure<sup>79, 80</sup> and reconstruction<sup>81</sup>, pH<sup>76, 77, 82</sup>, cation/anion effects<sup>46, 47, 82, 83</sup>, high current density<sup>84</sup>, applied voltage<sup>67, 82</sup>, temperature<sup>85, 86</sup>, and pressure<sup>86</sup>. The large overpotentials required and the low selectivity of electrolyzers hinder the large-scale implementation of CO<sub>2</sub>RR. Such complexity calls for an in-depth understanding of the reaction that eventually leads to process optimization.

Since experimental techniques cannot presently characterize surface active sites and detect all reaction intermediates involved in CO<sub>2</sub>RR, additional insight is obtained from

theoretical studies<sup>87, 88</sup>. The rational improvement of electrocatalysts requires detailed atomic-scale insight into the reaction mechanisms through which they transform reactants into products. Nevertheless, from an experimental standpoint, detecting reaction intermediates of electrocatalytic reactions is often technically challenging and, therefore, relatively uncommon<sup>77, 89, 90</sup>.

In the next sections, we present recent advances in the computational modeling of CO<sub>2</sub>RR, reviewing how structural sensitivity, redox treatments, pH and ions, and solvation are accounted for in the calculations and how they influence the catalytic activity and selectivity of this process. More in-depth reviews can be found in references<sup>68, 69, 71, 87</sup>.

## 2.1. Reaction mechanism of the CO<sub>2</sub>RR on Cu

An overview of the CO<sub>2</sub>RR network to C<sub>1</sub> and C<sub>2</sub> species appears in Figure 2.1.

Nørskov and co-workers<sup>39</sup> proposed the first DFT-based detailed mechanism to C<sub>1</sub> species. From adsorption energies on Cu(211) (see Figure 2.2), they concluded that the lowest-energy path was: CO<sub>2</sub> → \*COOH → \*CO → \*CHO → \*CH<sub>2</sub>O → \*CH<sub>3</sub>O → CH<sub>4</sub>+\*O → \*OH → H<sub>2</sub>O. Durand et al<sup>91</sup> used that pathway to calculate the free energies of all intermediate species on Cu facets, finding that adsorbates on the (211) exhibit the highest stability, followed by (100) and (111), in line with simple coordination rules<sup>92-95</sup>. From there on, such pathway was applied to different Cu facets<sup>96</sup> and alloys<sup>97, 98</sup>, other transition metals and alloys<sup>55, 99</sup>, and other types of materials<sup>100</sup>.

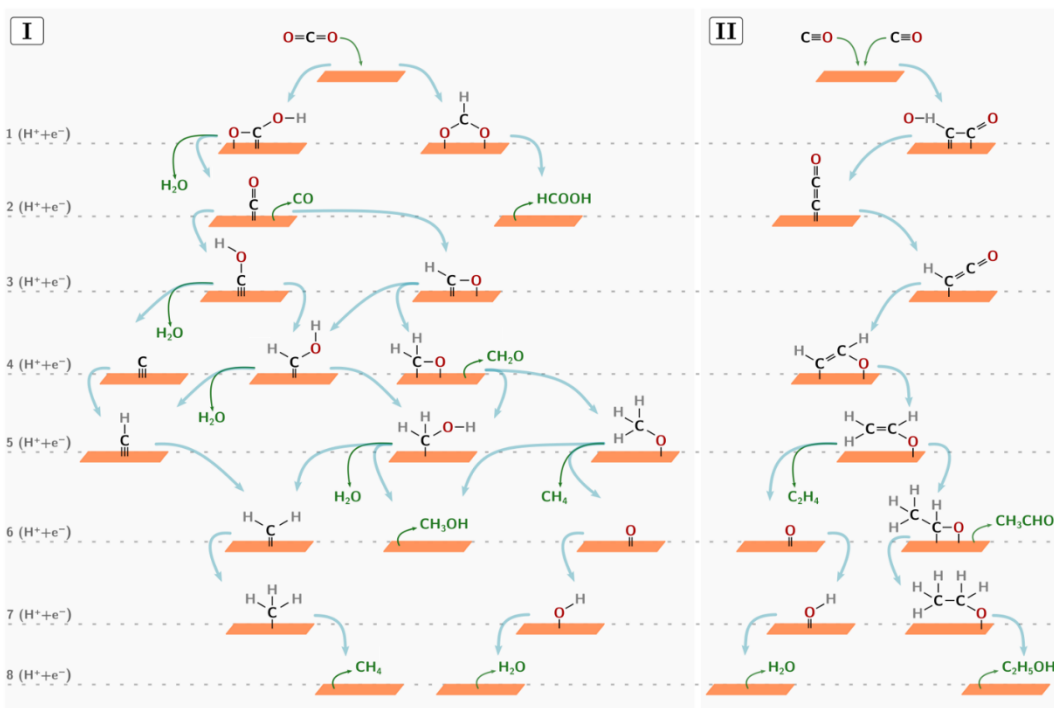


**Figure 2.1.** (I) A comprehensive reaction network for CO<sub>2</sub>RR to C<sub>1</sub> species. (II) Lowest-overpotential pathway for CO reduction to several C<sub>2</sub> species, redrawn from<sup>54</sup>. C, O and H atoms in CO<sub>2</sub> and adsorbed species are shown in black, red and gray, respectively. Arrows and species in green denote the desorbed products of CO<sub>2</sub>RR. Blue arrows connect adsorbates in the reaction network separated by a single proton–electron transfer. Only electrochemical steps of the reaction are included.

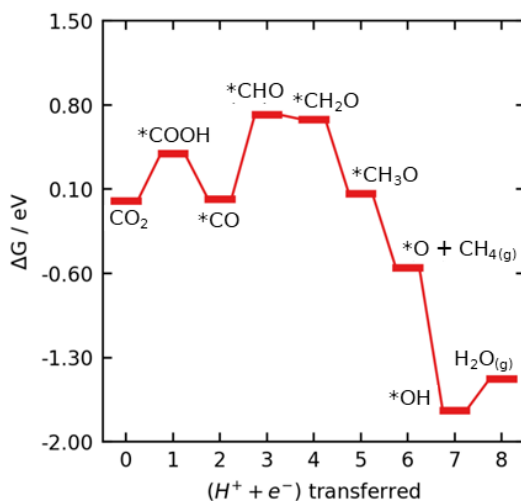


**Figure 2.2.** Free energy diagram for the lowest energy pathway on Cu(211) surfaces at 0 V vs RHE, redrawn with data from<sup>39</sup>.

The breaking of C–O bonds and the formation O–H, C–H and C–C bonds determine the kinetics of CO<sub>2</sub>RR on Cu electrodes. Nie et al<sup>101, 102</sup> evaluated the activation barriers of all transition states for CO<sub>2</sub>RR to methane, concluding that on Cu(111) the most favorable pathway goes via \*COH, instead of \*CHO, in agreement with other studies<sup>103</sup>. They also pointed out that the pathway continues through \*C, \*CH<sub>2</sub>, \*CH<sub>3</sub> and CH<sub>4</sub>. Later, Luo et al<sup>104</sup> showed that unlike for Cu(111), Cu(100) kinetically favors \*CHO over \*COH, attesting to a structure-sensitive mechanism dictated by elementary-step kinetics.

CO<sub>2</sub>RR to C<sub>2</sub> species such as ethylene and ethanol has also been explored thermodynamically. The electroreduction of CO (CORR), which is contained within CO<sub>2</sub>RR, is the most studied process. Calle-Vallejo and Koper<sup>105</sup> studied the CORR on Cu(100) considering \*CO dimerization as the first step toward ethylene, acetaldehyde and ethanol<sup>80</sup>. The \*CO dimer exhibits strong stabilization on square sites, justifying Cu(100)'s marked preference for ethylene production, while steps incline the selectivity to ethanol<sup>80</sup>. Cheng et al<sup>106</sup> proposed that Cu structures with stepped square sites provide enhanced catalytic activity and selectivity toward C<sub>2</sub> species. Garza et al<sup>107</sup> proposed reaction mechanisms for all reported C<sub>2</sub> products of CORR (ethylene, ethanol, acetaldehyde, ethylene glycol, glycolaldehyde, glyoxal, and acetate) on Cu(100) and Cu(111).

Montoya et al<sup>108</sup> determined the activation energies for the formation of C–C bonds on Cu in vacuum, finding that kinetic barriers depend on the hydrogenation of adsorbates. They concluded that \*CO dimerization is kinetically unfavorable in vacuum, compared to \*CO protonation and \*CHO-\*CHO coupling. However, they subsequently showed that water-solvated cations stabilize \*CO dimers, making \*CO-\*CO coupling surmountable under CORR conditions, particularly on Cu(100)<sup>109</sup>.

## 2.2. Scaling relations and volcano plots

Scaling relations are linear correlations between sets of adsorption energies<sup>110</sup>, that can be expressed as:  $\Delta E_2^i = m_{1,2}\Delta E_1^i + b_{1,2}^i$ . The slope  $m_{1,2}$  can be roughly estimated as the ratio of the valences of adsorbates 1 and 2<sup>110, 111</sup>, regardless of the adsorption site. For instance, the scaling between \*CH vs \*C has a slope  $\frac{3}{4}$ . The offset  $b_{1,2}^i$  linearly depends on the coordination number of facet  $i$ <sup>57, 92</sup>, so that (100) facets typically have lower offsets than (111) facets for a given adsorbate pair. These relationships are used to build volcano-type activity plots, which conveniently condense free-energy diagrams for numerous materials. This is shown for CO<sub>2</sub>RR to methane in Figure 2.3, in which the two potential-limiting steps are displayed as a function of the adsorption energy of CO ( $\Delta G_{\text{CO}}$ ). Thus, searching for optimal CO<sub>2</sub>RR catalysts in a complex optimization space is reduced to finding materials with  $\Delta G_{\text{CO}}$  close to the volcano apex, which can be performed via materials screening. Note, however, that CO<sub>2</sub>RR scaling-relation-based screening routines assuming a single mechanism for all materials and facets, which might not always be an appropriate simplification<sup>57, 112</sup>. This can be remediated using structure-sensitive scaling relations<sup>57, 92</sup>, as explained in section 2.3.

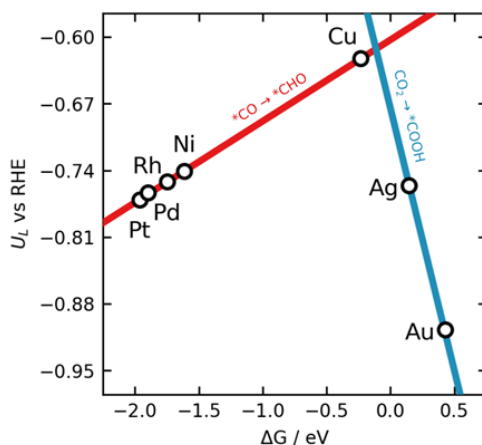


**Figure 2.3.** Scaling-relations-based volcano plot for CO<sub>2</sub>RR on 7 transition metal surfaces, redrawn with data from<sup>55</sup>; limiting potentials ( $U_L$ ) correspond to the two first elementary proton-electron transferences.

### 2.3. Structural, pH and cation/anion effects

Structural sensitivity, pH and ion effects are all coupled during CO<sub>2</sub>RR, and modify its mechanism. The products and corresponding onset potentials and faradaic efficiencies, depend on the metal used<sup>68, 113, 114</sup> and their surface structure<sup>79, 115</sup>. However, scaling-relation-based screening studies usually consider a single reaction mechanism<sup>55, 99, 116</sup>. Alternatively, Calle-Vallejo and Koper<sup>57</sup> showed that metal- and structure-sensitive bifurcating pathways can be incorporated into screening routines using scaling relations. This was illustrated on \*CO hydrogenation to \*COH and \*CHO on 5 different sites and 9 transition metals. Figure 2.4 shows that the preference between \*COH (dashed lines) or \*CHO (solid line) systematically depends on the coordination of the active sites.

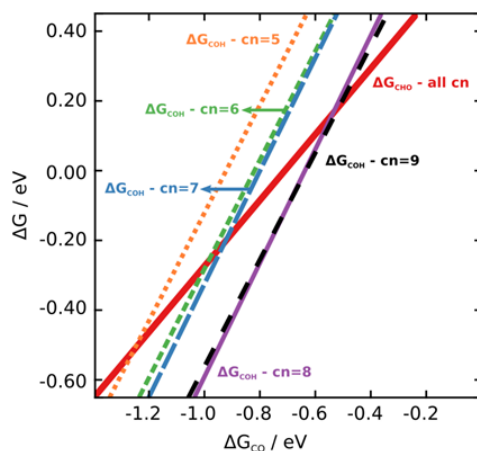


**Figure 2.4.** Structure-sensitive determination of pathway bifurcations during \*CO hydrogenation to \*CHO (solid line) or \*COH (dashed lines, each for a different coordination number) redrawn with data from<sup>57</sup>.

Furthermore, pH plays an essential role in the CO<sub>2</sub>RR mechanism. From a computational perspective, successive proton-coupled electron transfers are usually assumed in every step of the mechanism, so as to enable the use of the CHE<sup>39</sup>. Note that this model cannot capture pH effects, as the adsorption energies of all intermediates shift proportionally. This is problematic when analyzing CORR, which displays

distinct pH- and structure-dependent features: while CORR to CH<sub>4</sub> is favored on pristine and stepped Cu(111) and is pH-dependent in the SHE scale, C<sub>2</sub>H<sub>4</sub> prefers pristine Cu(100) terraces and is pH-independent in the SHE scale<sup>113, 117</sup>. According to Hori et al<sup>75</sup>, such dissimilar pH responses indicate that the rate-limiting step of CORR to CH<sub>4</sub> involves an H<sup>+</sup> transfer, whereas that of CORR to C<sub>2</sub>H<sub>4</sub> does not. This makes CO<sub>2</sub>RR and CORR toward CH<sub>4</sub> suitable for CHE models, whereas C<sub>2</sub>H<sub>4</sub> production should be analyzed cautiously.

Calle-Vallejo and Koper<sup>105</sup> studied CORR on Cu(100) to C<sub>2</sub> species, considering as the first step the reductive coupling of 2\*CO to \*COCO. Such step proceeds via a decoupled electron-then-proton transfer that forms first a negatively charged CO dimer. Such coupling leads to a pH-independent C<sub>2</sub> pathway that complies with experiments. The dimer exhibits a remarkable preference for Cu(100)<sup>93</sup> because of its square symmetry. However, the initial model showed high kinetic barriers for C–C coupling. Thus, apart from pH effects, one should consider additional features of experimental CORR such as cation effects.

Murata et al<sup>118</sup> showed that alkaline cations enhance the production of multi-carbon species. The smaller hydration sphere of larger cations supposedly favors their adsorption on cathodic surfaces, yielding more positive potential values, thereby increasing the selectivity toward C<sub>2</sub>H<sub>4</sub>. Bell and co-workers<sup>46</sup> explained cation effects based on the pK<sub>a</sub> values of their hydrolysis. Larger CO<sub>2</sub> concentrations near the cathode and lower local pH with increasing cation size are expected, which satisfactorily explains cation effects during CO<sub>2</sub>RR but not those observed during CORR.

Computationally, cation effects are accounted for implicitly or explicitly. Nørskov and co-workers opted for an implicit description of cations, applying an electric field instead. The field interacts with the adsorbates<sup>47, 119</sup> modifying the adsorption energies depending on the species' dipole moment. In contrast, Janik and co-workers include the ions explicitly. They suggested that specific halide adsorption on Cu may occur at negative electrode potentials<sup>104</sup>, and consequently, the specific adsorption of Cl<sup>-</sup>, Br<sup>-</sup>,

and  $I^-$  affects  $CO_2RR$ . This agrees with Varela et al's<sup>83</sup> experimental observations that  $Br^-$  increases 3.5 times the selectivity toward CO compared to  $Cl^-$ . Besides,  $I^-$  favors CO reduction to methane over CO desorption. Recently, Perez-Gallent et al<sup>82</sup> presented a joint computational-experimental study of cation effects on CORR. Explicitly including the cations, they observed that CO hydrogenation is considerably more difficult for monomers compared to dimers, because cations substantially stabilize  $C_2$  adsorbates and not  $C_1$  species. This attests to a more favorable CO dimerization than previously thought<sup>105</sup>, and plausibly explains why  $C_2H_4$  production exhibits earlier onset potentials than  $CH_4$ <sup>82</sup>.

## 2.4. Oxide-derived Cu electrodes

Inclining the  $CO_2RR/CORR$  selectivity toward ethanol is economically and technologically advantageous because of its relatively high market price, ease of storage and high energy density<sup>120</sup>. Kanan and co-workers<sup>121</sup> found that Cu catalysts prepared by successive redox processes (known as oxide-derived Cu, OD-Cu), yielded higher activity and selectivity for  $C_2$  products, especially ethanol, compared to polycrystalline and single-crystal Cu. They also found that OD-Cu's active sites possess remarkably strong CO adsorption energies which are probably located at grain boundaries<sup>122</sup>. Others suggest that OD-Cu's enhanced electrocatalytic activity is due to an oxide phase or to subsurface oxygen atoms retained from the redox treatments<sup>81, 123</sup>. Although some theoretical studies show that subsurface oxygen indeed enhances Cu's selectivity toward  $C_2$  products by increasing the coverage of  $*CO$ <sup>124, 125</sup>, it is argued that subsurface oxygen is highly unstable. Alternatively, Head-Gordon and co-workers<sup>126</sup> claim that calculations including dispersive interactions, solvation and applied voltage predict favorable  $CO_2$  chemisorption on Cu, precluding the need for subsurface oxygen and suggesting that OD-Cu's active sites are located at defects. Recent computational studies have concluded that the ethanol-producing active sites at OD-Cu electrodes are composed of square, undercoordinated Cu islands<sup>127</sup>, in agreement with the tremendous roughness of OD-Cu observed in experiments<sup>128</sup>.

## 2.5. Solvation effects

Electrocatalytic activities are determined, to a large extent, by the interplay of (i) adsorbates, (ii) substrates and (iii) solvents at the electrochemical interface. However, capturing the interactions of these three components is usually arduous. Thorough descriptions of reaction pathways can be made computationally by evaluating at each stage of the reaction adsorbate-substrate interactions, together with adsorbate-solvent and solvent-substrate interactions. While adsorbate-substrate interactions have been vastly explored for the past 20 years in electrocatalysis<sup>36</sup>, adsorbate-solvent and solvent-substrate interactions started to receive attention only in the past few years<sup>59, 129-133</sup>.

Since a great number of electrocatalytic reactions use water as a solvent, such as oxygen evolution and reduction, hydrogen evolution and oxidation, and CO<sub>2</sub> and CO reduction (CO<sub>2</sub>RR and CORR), it is vital to incorporate water-adsorbate interactions into computational electrocatalysis models<sup>1, 69, 88, 134</sup>. There are two main ways in which water molecules influence heterogeneous catalysis reactions: by hydrogen bonding with adsorbed species or by acting as co-catalysts<sup>135</sup>. Such influence is particularly strong for adsorbates able to create hydrogen bonds and can significantly modify the adsorbate-substrate interactions<sup>136</sup>.

The study of water-substrate interactions is an active field of research on its own. For instance, on close-packed transition metal surfaces several water configurations have been observed experimentally, such as rings forming stable water layers, small dissociated water clusters, and double-stranded lines along defects<sup>137-139</sup>. However, water-adsorbate interactions have received considerably less attention.

There are three general approaches to treating the interactions between adsorbates and water within DFT calculations (see Figure 2.5). The first is by explicitly considering the water molecules in the simulation<sup>129, 140-142</sup>. Although in terms of accuracy this is probably the most appropriate way to estimate water solvation effects, it is computationally demanding and, therefore, impractical for exploring complex reaction networks on extended surfaces and nanoparticles of different materials. In general,

within the explicit approach arduous molecular dynamics (MD) simulations are needed. For instance, the wetting of a relatively small nanoparticle with a diameter below 2 nm, requires  $\sim 700$  explicit water molecules<sup>143</sup>. In the same way, modeling a  $4 \times 4$  Cu(100) surface slab requires near 50 explicit water molecules<sup>144</sup>. In other studies using a multiscale sampling (MSS) approach which combines classical MD with DFT, 54 water molecules were needed to simulate the liquid solvent for a  $3 \times 3$  Pt(111) slab<sup>145</sup>. In a more recent attempt to explore a wide range of different materials and adsorbates, 15 and 25 explicit water molecules (3 layers) were required on  $3 \times 4$  fcc (111) and  $3 \times 1$  fcc (211) facets, respectively (on Au, Cu, and Pt), to ensure an accurate description of the interactions between water and adsorbates (i.e. \*OH, \*CO, \*COH, \*CHO, among others) using ab initio molecular dynamics (AIMD) simulations.<sup>142</sup> Moreover, two of the main issues of sampling the phase space of water molecules using MD are the prohibitive cost of the ab initio simulations, and the ill-defined interaction parameters for the surface adsorbates in the more affordable classical simulations<sup>135, 146, 147</sup>.

A second approach consists of the implicit modeling of water. These models normally estimate solvent effects by placing the solute in a cavity within the solvent, which is treated as a dielectric continuous medium. The way in which the cavity and the boundary conditions are defined, gives rise to different models<sup>134, 148-157</sup>. For instance, the conductor-like screening model (COSMO)<sup>158</sup>, and its self-consistent generalizations to real solvents, COSMO-RS<sup>159</sup> and direct COSMO-RS<sup>160</sup>, or models that also include the ionic effects of charged interfaces and adsorbates, such as the Poisson-Boltzmann or the specific smooth dielectric models<sup>161, 162</sup>. There are also other developments such as joint DFT models, which incorporate a classical DFT description of the liquid<sup>163</sup>, linear polarizable continuum models (linear PCM)<sup>151</sup>, and PCM with nonlinear dielectric response (nonlinear PCM)<sup>164</sup>, as well as implementations to plane-wave packages such as VASPsol<sup>149</sup>. Mixed approaches have also been devised, combining a few explicit water molecules in the first solvation layer(s) with a continuous medium beyond<sup>165, 166</sup>. A comprehensive analysis of the different implicit solvation methods can be found in specialized reviews<sup>134, 154</sup>. It is to be noted that although implicit solvation models are useful and generally inexpensive, their

description of hydrogen bonding and their estimation of reaction energies are still challenging<sup>146, 147, 167, 168</sup>, so they may lead to erroneous predictions when water-adsorbates interactions are strong, or when water participates in the reaction.

The third approach consists of adding specific or “ad hoc” solvation corrections to adsorption energies calculated in vacuum. In this context, ad hoc refers to solvent effects on adsorption energies assessed once for a specific material and adsorbate. In various DFT-based studies some corrections to the adsorption energies have been reported for \*R-OH (where R is a hydrocarbon chain, e.g. \*COH), \*OH, \*OOH, \*CO, \*CHO, \*NOH, \*NHO, \*NH<sub>x</sub>, among others<sup>36, 39, 54-60</sup>. The corrections were estimated either on Cu(111) or Pt(111) from the differences between the adsorption energies with and without explicit water molecules in the calculations, and their magnitudes are between -0.1 and -0.6 eV. A usual approximation is to assume that those corrections are identical for other transition metals<sup>55, 58</sup>. However, recent works on Pt-based near-surface alloys<sup>59, 169</sup>, late transition metals<sup>130</sup> and metalloporphyrins<sup>57</sup>, showed that solvation corrections may change significantly from one material to the next and cause significant changes in adsorption energies, reaction pathways, and calculated overpotentials obtained from simulations in vacuum.

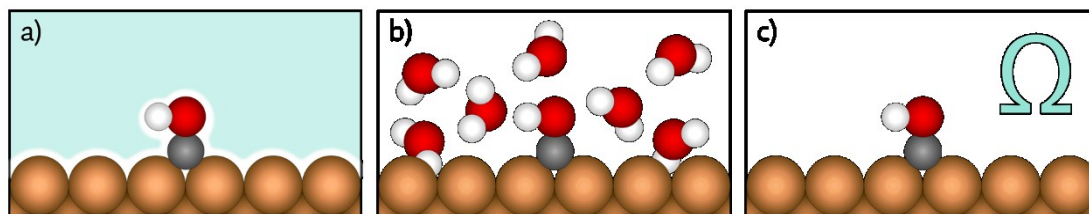


**Figure 2.5.** Schematics of the different solvation methods available to account for the solvent in simulations of electrochemical interfaces. \*COH is used to exemplify the adsorbate. a) Implicit solvation models, b) explicit incorporation of water molecules, and c) ad hoc or specific corrections calculated explicitly and applied to in vacuum calculations.

## Summary

During this chapter some of the many effects and interactions present in the CO<sub>2</sub>RR are presented. It is important to note that solvation, is perhaps one of the most excluded

(or miscalculated) effects, but it is highly important for the reaction. CO<sub>2</sub>RR takes place in aqueous media and the water presence produce adsorbate-water interactions through hydrogen bonds that alters the reaction performance. It is known that those interactions cannot be fully accounted by implicit methods, and although the explicit inclusion of the solvent is probably the most accurate method, it is computationally demanding and impractical. Therefore, adding solvation corrections to DFT calculations performed in vacuum seem to be the right way, but it still requires enhancing.

In this context, the following question arises: it would be possible to estimate solvation effects for specific systems in an affordable and accurate way? Although in this field, accuracy and affordability have commonly been anticorrelated, finding a midpoint between them was one of our goals in this work.

In our attempt to improving DFT-based approaches to study CO<sub>2</sub>RR, we developed a systematic and affordable method to calculate solvation effects on electrochemical systems which is explained in the following chapter.

## Chapter 3. Developing a systematic micro-solvation method using DFT

---

### 3.1. Adsorbate-water interactions

We define the adsorption of species A in vacuum in Equation (3.1), and in solution in Equation (3.2).



Where \* denotes a free surface site, \*A and  $n^*H_2O$  denote adsorbed A and  $n$  adsorbed water molecules, respectively, and the brackets indicate states in solution. In this context, the adsorption energies in vacuum ( $\Delta G_A^{vacuum}$ ) and in solution ( $\Delta G_A^{solution}$ ), both with respect to A in vacuum, can be written as:

$$\Delta G_A^{vacuum} = G_{*A} - G_A - G_* \quad (3.3)$$

$$\Delta G_A^{solution} = G_{[*A+n^*H_2O]} - G_A - G_{[n^*H_2O+*]} \quad (3.4)$$

The solvation energy ( $\Omega$ ) is generally defined as the energy obtained when a solute is transferred from an isolated state (in vacuum) to a state in which it is surrounded by the solvent.<sup>170</sup> For an adsorbate \*A that will be solvated by water, it is:



where  $[*A+n^*H_2O]$  denotes the adsorbate \*A solvated by  $n$  adsorbed water molecules, and  $[n^*H_2O+*]$  denotes a surface wet with  $n$  water molecules, and a free adsorption

site. The reaction energy of Equation (3.5), which is equivalent to the solvation energy of \*A, is given by:

$$\Omega_A = G_{[*_A+n*H_2O]} + G_* - G_{*_A} - G_{[n*H_2O+*]} \quad (3.6)$$

Alternatively,  $\Omega_A$  can be expressed in terms of the adsorption energies in vacuum and in solution as shown in Equation (3.7):

$$\Omega_A = \Delta G_A^{solution} - \Delta G_A^{vacuum} \quad (3.7)$$

Equation (3.7) is the basis of ad hoc solvation schemes (see sections 1.3.2 and 2.5), in which  $\Omega_A$  is calculated once for a given system and then transferred to many others<sup>55, 59, 171</sup>. In that way, adsorption energies in solution are rapidly estimated as in Equation (3.8), with the superscript # indicating an extrapolation to systems different than that where  $\Omega_A$  is calculated.

$$\Delta G_A^{solution, \#} \approx \Delta G_A^{vacuum, \#} + \Omega_A \quad (3.8)$$

Given that all species in Equation (3.5) are adsorbed and appear on both sides of the reaction, the changes in  $\Delta E_{ZPE}$  and  $T\Delta S$ , from Equation (1.32), are negligible, at least for small adsorbates. Therefore, we assume that  $\Omega_A$  can be estimated only using DFT energies. Results confirming this statement are provided later in section 4.4.

$$\Omega_A = \Delta E_A^{solution} - \Delta E_A^{vacuum} \quad (3.9)$$

However, we note that solvation entropy terms may in some cases be significant, in particular for large adsorbates and those making strong hydrogen bonds<sup>145</sup>.

## 3.2. Water self-solvation

It is well known that water molecules interact with metal surfaces by clustering<sup>139</sup>, and adsorbed water clusters usually adopt ice-like hexagonal configurations. In those, each water molecule on the surface forms three hydrogen bonds with surrounding water

molecules, resulting in building units of four water molecules. Following conventional solvation models<sup>172</sup>, and in order to make the simulations with the lowest number of water molecules<sup>173</sup>, we assume that four adsorbed water molecules that do not interact with each other are brought together so that three of them solvate the other one. As is shown in Figure 3.1, these 4-molecule building units can be found in water bilayers formed by different polygons<sup>174</sup>.

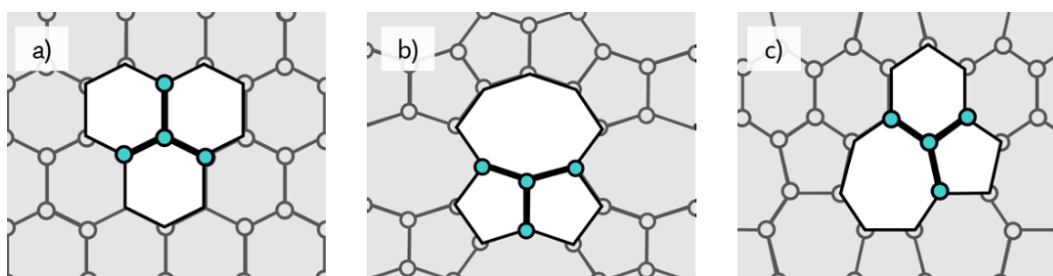


**Figure 3.1.** Examples of the possible configurations of the 4-molecule building units of water layers adsorbed at a surface. The water layers can be composed of a) hexagons, b) pentagons and octagons, c) pentagons, hexagons and heptagons, among others. Water molecules are represented as nodes and hydrogen bonds as blue lines. Vertices of polygons normally correspond to top positions of surface metal atoms.

There are three different possible configurations for the first solvation shell of an adsorbed water molecule on Cu(111), as is shown in Figure 3.2.

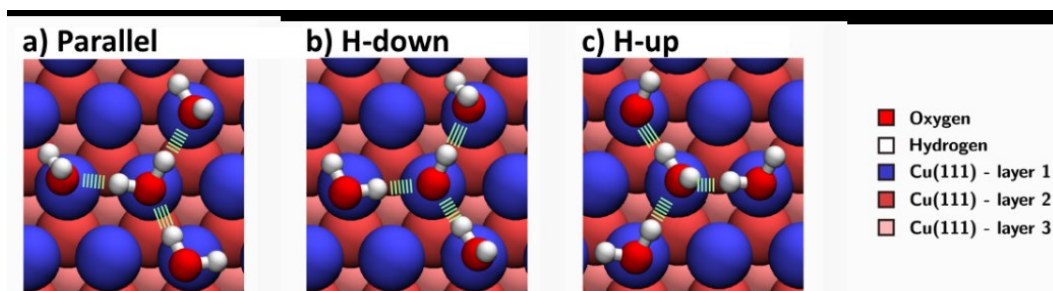


**Figure 3.2.** Top views of the atomic-scale schematics of specific configurations of the 4-molecule water clusters forming the first solvation shell of an adsorbed water molecule on Cu(111). The central molecule can have one H atom pointing down (H-down), up (H-up) or both H atoms in a plane parallel to the surface (parallel).

The water self-solvation process can be represented as:



Where the brackets on the right indicate that the water molecules are together and interacting. Then, the total self-solvation correction of adsorbed water in a micro-solvation (MS) environment is given by:

$$\Omega_{H_2O} = E_{[^*H_2O+3^*H_2O]} - 4E_{^*H_2O} \quad (3.11)$$

We can also define the adsorption of each water in vacuum as  $H_2O + * \rightarrow ^*H_2O$  and in the MS environment as  $4H_2O + 4* \rightarrow [^*H_2O+3^*H_2O]$ , obtaining:

$$\Delta E_{H_2O}^{MS} = E_{[^*H_2O+3^*H_2O]} - 4E_{H_2O} - 4E_* \quad (3.12)$$

$$\Delta E_{H_2O}^{vacuum} = E_{^*H_2O} - E_{H_2O} - E_* \quad (3.13)$$

From Equations (3.11) to (3.13), the total self-solvation can be rewritten as:

$$\Omega_{H_2O} = \Delta E_{H_2O}^{MS} - 4\Delta E_{H_2O}^{vacuum} \quad (3.14)$$

Equation (3.14) does look like Equation (3.9), since water behaves simultaneously as the solvent and the solute during its self-solvation process. Finally, the self-solvation correction in eV per hydrogen bond (eV/HB) is a third of  $\Omega_{H_2O}$  (Note that the central water molecule forms three hydrogen bonds), which leads to:

$$\Omega_{H_2O}^{HB} = \Omega_{H_2O}/3 = \frac{1}{3}\Delta E_{H_2O}^{MS} - \frac{4}{3}\Delta E_{H_2O}^{vacuum} \quad (3.15)$$

### 3.3. A decision criterion for adsorbate-water hydrogen bonding

As the process is based on the consecutive addition of water molecules to the system starting with  $n = 1$ , an energy comparison needs to be done in an iterative fashion. Since there are no solvent effects when A is adsorbed in vacuum,  $\Omega_A^0 = 0$  eV.

$$\Omega_A^n - \Omega_A^{n-1} \leq \Omega_{\text{H}_2\text{O}}^n - \Omega_{\text{H}_2\text{O}}^{n-1} \quad (3.16)$$

As is shown in Figure 3.2, there are three different configurations of the water building unit depending on the orientation of hydrogen atoms of the central water molecule. However, we have found that they are energetically similar in transition metals as can be seen in Table 3.1.

**Table 3.1.** Calculated  $\Omega_{\text{H}_2\text{O}}^{\text{HB}}$  in eV/HB for the different configurations of the first solvation shell of an adsorbed water molecule on different transition metals, following the notation used in Figure 3.3.

Configuration	$\Omega_{\text{H}_2\text{O}}^{\text{HB}}$			
	Cu(111)	Au(111)	Ag(111)	Zn(0001)
Parallel	-0.28	-0.28	-0.24	-0.28
H-down	-0.21	-0.22	-0.18	-0.23
H-up	-0.25	-0.25	-0.21	-0.27
Average	$-0.24 \pm 0.04$	$-0.25 \pm 0.03$	$-0.21 \pm 0.03$	$-0.26 \pm 0.02$

Note that with each change in the value of  $n$ , the state  $[n^*\text{H}_2\text{O}+^*]$  (from Equation 3.5) also changes. The following approximation can be applied:

$$\Omega_{\text{H}_2\text{O}}^n \approx n \cdot \Omega_{\text{H}_2\text{O}} \quad (3.17)$$

Then, having  $\Omega_{\text{H}_2\text{O}}^{\text{HB}}$  assessed from Equations (3.15) and (3.17) we can define our decision criterion as:

$$\Omega_A^n - \Omega_A^{n-1} < \Omega_{\text{H}_2\text{O}}^{\text{HB}} \quad (3.18)$$

Accordingly, the number of water molecules ( $n$ ) in the first solvation shell of adsorbate \*A can be determined by consecutively adding water molecules to the system and evaluating in each case whether the entire system is stabilized or not, not only taking as reference the adsorbate but also the water molecules. Every time the additional stabilization provided by the addition of a water molecule is larger than the previous calculated state and larger than the self-stabilization of water, one more hydrogen bond is formed between the adsorbate and water, and  $n$  is increased by one (see Figure 3.3).

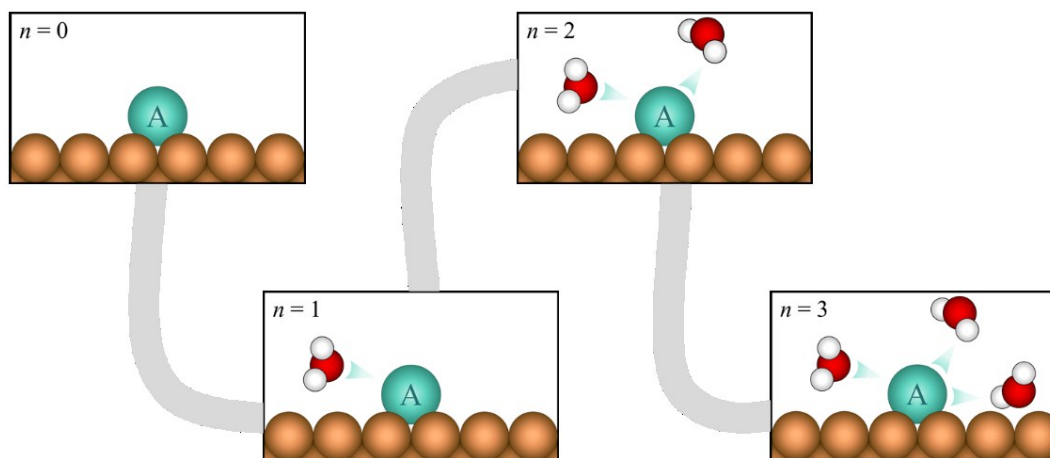


**Figure 3.3.** Schematics of every calculation step to determine the number of water molecules required in the first solvation shell of the adsorbate.

If the stabilization provided by the additional water-adsorbate hydrogen bond is not larger than the water self-stabilization, the number of water molecules interacting with the adsorbate is fixed at  $n - 1$ , being  $n = 1$  the lowest. Finally, the solvation energy  $\Omega_A$  is equivalent to the interaction energy between  $n$  water molecules and the adsorbate. A flow diagram of the calculation process exposed in this chapter is provided in Figure 3.4.

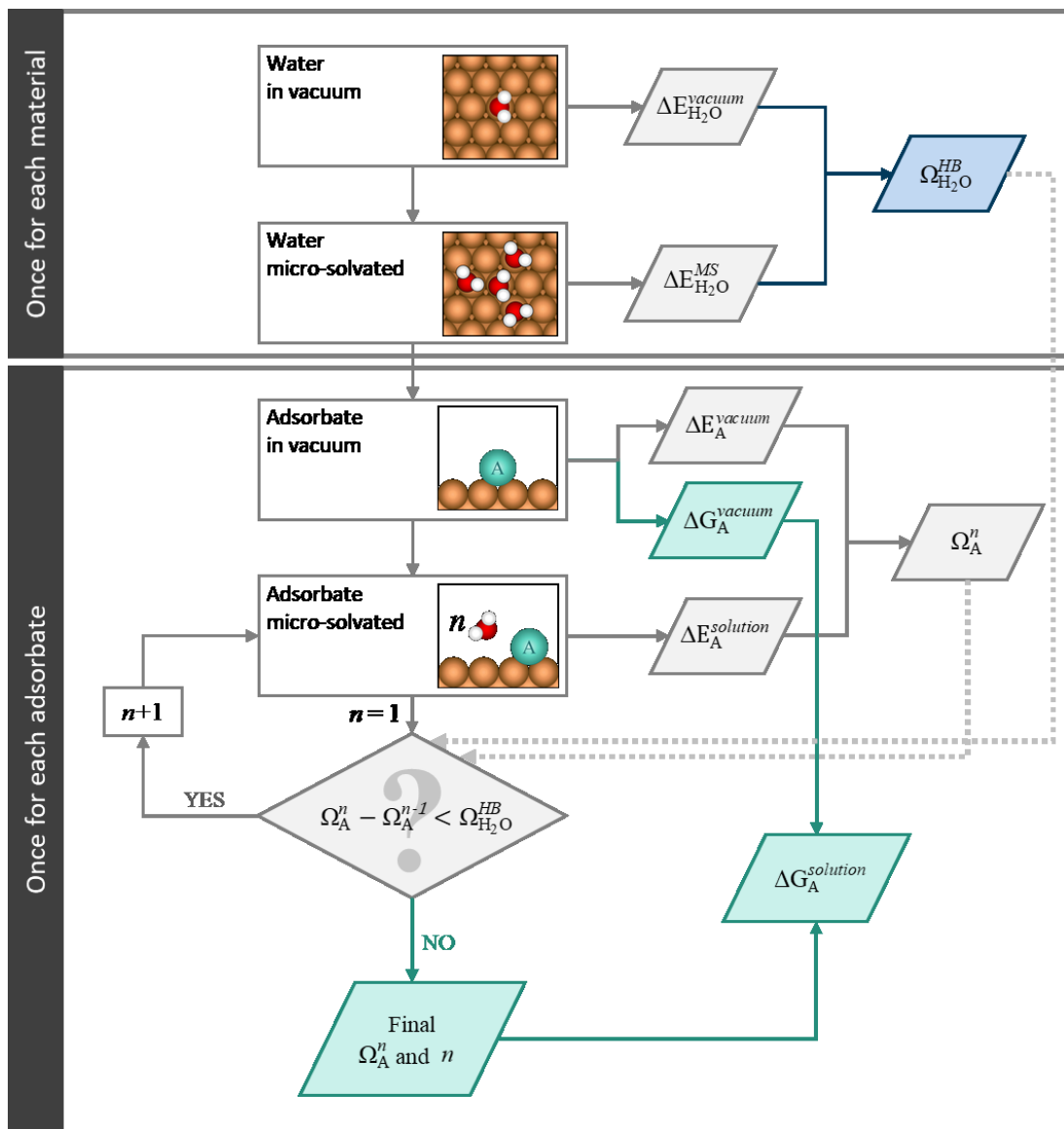


Figure 3.4. Flow diagram of the calculation steps to determine solvation contributions to the adsorption energies of electrochemical systems using the systematic micro-solvation method developed in this work.

### 3.4. Additional details for DFT calculations of the micro-solvation energy using VASP

Due to the explicit inclusion of water molecules, larger cells than those described in section 1.3.1 were necessary to avoid interactions between neighboring cell repetitions. Periodic  $4 \times 4 \times 3$  cells of (111) facets were used to determine the solvation energies of

the adsorbates and the self-solvation of water molecules. Initial geometries of adsorbed species were taken from the lowest energy configurations obtained from in vacuum screening (see Figure 1.5), and adsorbed water molecules were in the surroundings, following the ice-like configuration. Rotations of water molecules and conformers of the adsorbates were also tested, and, in some cases, changes in the adsorption site with respect to in vacuum positions were considered (see section 4.2).

## Summary

Adsorbate solvation via hydrogen bonding is one of the main factors that intervene in the reaction performance at the electrochemical interface. In this chapter, we explored the solvation as a likely surface event that only takes place if the interaction between  $n$  water molecules and the adsorbate decreases the total energy of the system. In other words, solvent-adsorbate hydrogen bonds only occur when they lead to a more stable state compared to that in which water molecules are solvating themselves.

Our method finds upon testing a collection of  $n\text{H}_2\text{O}$ -adsorbate configurations, the one that provides the largest stabilization to the system. If it is determined that an adsorbate-water hydrogen bond is made, such configuration is assumed to dominate over the rest in view of its greater stability. Thus, the solvation corrections calculated here may be considered as an upper bound to those found if the solvent were sampled via e.g. molecular dynamics (the lower bound provided by implicit methods).

In the next chapter we present the results of the implementation of the systematic micro-solvation method, applying it to the  $\text{CO}_2\text{RR}$  mechanism. First, we focused on Cu surfaces, and then we test the same procedure on different transition metals.

## Chapter 4. Calculations of the CO<sub>2</sub>RR

### 4.1. In vacuum CO<sub>2</sub>RR on Cu

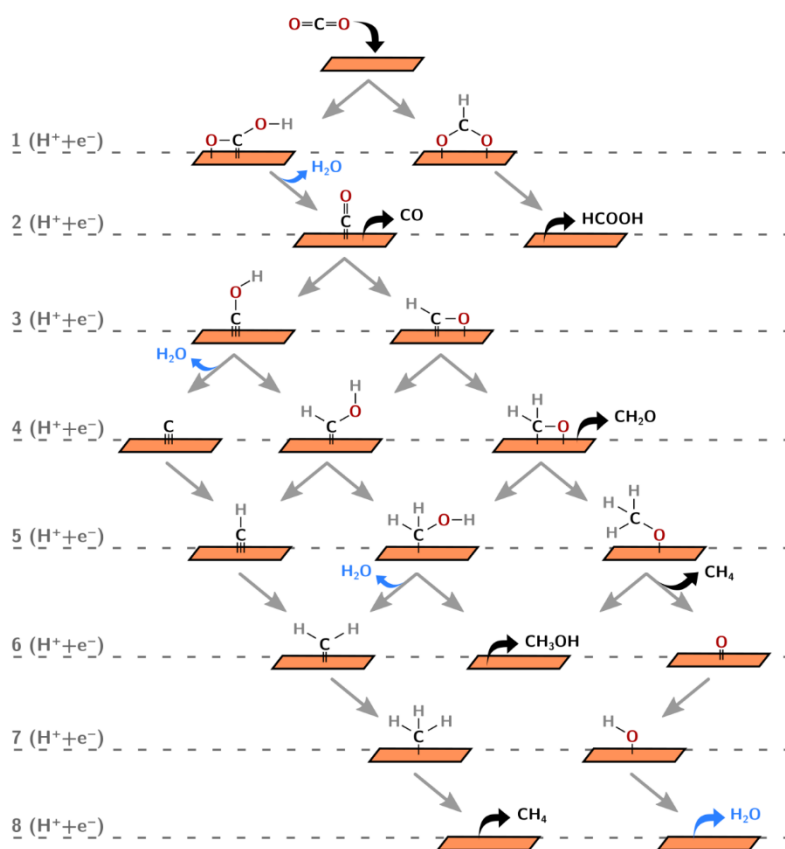


**Figure 4.1.** Reaction network of CO<sub>2</sub>RR to CO, CH<sub>2</sub>O, CH<sub>3</sub>OH and CH<sub>4</sub> on Cu. C, O and H atoms are shown in black, red and gray, respectively. The catalyst is shown in orange. Thin blue arrows denote desorbed products of CO<sub>2</sub>RR. Bold arrows connect adsorbates separated by a single proton and electron transfer.

CO<sub>2</sub>RR on Cu electrodes can produce over 16 different hydrocarbon products containing up to five carbon atoms.<sup>67</sup> In this work, we only considered the one-carbon

(C<sub>1</sub>) products, i.e. CO, CH<sub>2</sub>O, CH<sub>3</sub>OH and CH<sub>4</sub>, and the reaction pathways for their formation, as is shown in Figure 4.1.

In-vacuum calculations can provide a useful first approach to the electrochemical reduction of CO<sub>2</sub>. Although the effect of the water solvent in the system can cause significant differences in the reaction mechanism, in-vacuum results can provide valuable insight and serve as the basis for the calculations in solution. The adsorption energies in vacuum of the C<sub>1</sub> intermediates were determined after testing different configurations on all inequivalent sites of each Cu facet (see Figure 1.5).

A summary of the in-vacuum calculations is presented in Table 4.1, presenting the E<sub>ZPE</sub>, the vibrational entropies TS<sub>vib</sub> (at 298.15 K), and the formation energies from CO<sub>2</sub> (ΔG<sub>f</sub>) for the intermediates of the C<sub>1</sub> reaction pathway of the CO<sub>2</sub>RR. Note that under this assumption, the lowest-energy pathway on all the surfaces is: CO<sub>2</sub> → \*COOH → \*CO → \*CHO → \*CH<sub>2</sub>O → \*CH<sub>3</sub>O → \*O → \*OH → H<sub>2</sub>O.<sup>39</sup>

**Table 4.1.** Calculated formation energies (ΔG<sub>f</sub>) without solvation corrections, for all the intermediates of the CO<sub>2</sub>RR to CO, CH<sub>3</sub>OH, and CH<sub>4</sub> on Cu(111), Cu(100) and Cu(110). The symbol \* denotes adsorbed species. Zero-point energies (E<sub>ZPE</sub>), vibrational contributions to the entropy (TS<sub>vib</sub>) reported do not depend on the solvation correction used.

Adsorbate	E <sub>ZPE</sub>	TS <sub>vib</sub>	ΔG <sub>f</sub> /Cu(111)	ΔG <sub>f</sub> /Cu(100)	ΔG <sub>f</sub> /Cu(110)
*COOH	0.62	0.22	0.17	0.01	-0.20
*CO	0.16	0.14	-0.35	-0.24	-0.39
*CHO	0.46	0.14	0.34	0.13	0.06
*CH <sub>2</sub> O	0.74	0.15	-0.13	-0.41	-0.48
*CH <sub>3</sub> O	1.08	0.22	-1.21	-1.33	-1.51
*CH <sub>2</sub> OH	1.06	0.21	-0.33	-0.47	-0.71
*O	0.06	0.06	-1.75	-2.03	-2.02
*OH	0.35	0.10	-1.58	-1.73	-2.84
*COH	0.46	0.15	0.59	0.42	0.52
*CHOH	0.76	0.18	0.25	0.25	-0.03
*C	0.09	0.03	1.60	0.37	0.92
*CH	0.33	0.05	0.05	-0.45	0.02
*CH <sub>2</sub>	0.55	0.09	-0.56	-0.63	-0.79
*CH <sub>3</sub>	0.90	0.15	-1.56	-1.58	-1.90

## 4.2. Micro-solvated CO<sub>2</sub>RR on Cu

The micro-solvation approach presented in chapter 3 and the in-vacuum results were used to determine the reaction pathways for the CO<sub>2</sub>RR. The calculated value of  $\Omega_{\text{H}_2\text{O}}^{\text{HB}} = -0.24 \pm 0.04$  on Cu (see Table 3.1) was used to evaluate the number of hydrogen-bonded water molecules ( $n$ ) and their contribution to the adsorption energies ( $\Omega_{\text{A}}$ ) for the different adsorbates involved in the CO<sub>2</sub>RR to C<sub>1</sub> products. The solvation corrections along with the number of hydrogen-bonded water molecules for each adsorbate are presented in Table 4.2. For comparison, ad hoc solvation corrections from previous studies<sup>39, 55</sup> and those calculated using an implicit method<sup>149</sup> are also reported.

**Table 4.2.** Calculated solvation corrections ( $\Omega_{\text{A}}$ , in eV) with their corresponding number of hydrogen bonds formed with surrounding water molecules ( $n$ ) for species adsorbed on Cu(111), and hydrogen bond (HB) type ( $a$  if accepted or  $d$  if donated by the adsorbate).  $\Omega_{\text{OH}}^a$  is referred to fcc hollows (in vacuum), and  $\Omega_{\text{OH}}^b$  to atop.

Adsorbate	$n$	HB type	This work	Implicit <sup>149</sup>	Ad hoc 1 <sup>54</sup>	Ad hoc 2 <sup>36, 39</sup>
*COOH	1	$a$	-0.28	-0.24	-0.48	-0.25
*CO	0	-	0.00	-0.03	-0.10	-0.10
*CHO	0	-	0.00	-0.05	-0.10	-0.10
*CH <sub>2</sub> O	1	$a$	-0.21	-0.14	-0.10	-0.10
*CH <sub>3</sub> O	1	$a$	-0.26	-0.10	0.00	0.00
*CH <sub>2</sub> OH	1	$d$	-0.30	-0.19	-0.38	-0.25
*O	0	-	0.00	-0.11	0.00	0.00
*OH	3	$d \& a$	$-0.58^a (-1.27)^b$	-0.19	-0.50	-0.50
*COH	1	$d$	-0.45	-0.25	-0.38	-0.25
*CHOH	1	$d$	-0.27	-0.14	-0.38	-0.25
*C	0	-	0.00	-0.08	0.00	0.00
*CH	0	-	0.00	-0.04	0.00	0.00
*CH <sub>2</sub>	0	-	0.00	-0.04	0.00	0.00
*CH <sub>3</sub>	0	-	0.00	-0.06	0.00	0.00

To illustrate how the solvation values were obtained, let us consider \*COH as an example. When the first \*H<sub>2</sub>O is added to \*COH ( $n = 1$ ), the resulting stabilization is -0.45 eV. According to Table 3.1, the average solvation energy per hydrogen bond

( $\Omega_{\text{H}_2\text{O}}^{\text{HB}}$ ) for Cu is  $-0.24 \pm 0.04$  eV/HB. Since  $-0.45 \leq -0.20$  (the lower bound), then  $n = 1$  for \*COH. If we continue to  $n = 2$ , a total stabilization of  $-0.51$  eV, but  $-0.51 - (-0.45) \geq -0.20$ . Thus, it is unlikely that \*COH will be stabilized by a second water molecule, and we conclude that  $n = 1$ .

When in vacuum calculations of \*OH on Cu(111) are performed, the most stable site of adsorption is found at fcc hollows. However, in a solvated environment, \*OH is more stable on atop sites. Note that in Table 4.2, the solvation correction for \*OH of  $-1.27$  eV is substantially more negative than for the ad hoc methods, since it is based on atop \*OH in vacuum. If it were referred to \*OH in vacuum adsorbed at fcc hollows, the correction would be  $-0.58$  eV, which agrees with the ad hoc methods<sup>36, 39, 54</sup>.

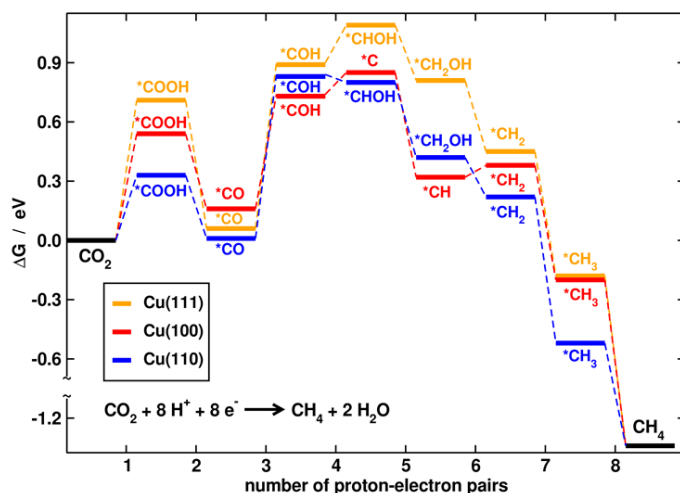
We rationalize the trends for OH-containing adsorbates in Table 4.2 based on the polarity of the O-H bonds. In the  $E_T^N$  scale, which is a dimensionless scale of solvent polarity<sup>175, 176</sup> that extends from 0 to 1, H<sub>2</sub>O has a polarity of 1 and is the most polar solvent. When a hydrogen atom is replaced in the structure by CH<sub>x</sub> groups to give e.g. CH<sub>3</sub>OH, CH<sub>3</sub>CH<sub>2</sub>OH and CH<sub>3</sub>CH<sub>2</sub>CH<sub>2</sub>OH, the polarity goes down to 0.762, 0.654, and 0.617. The same holds for carboxylic acids, such as HCOOH, CH<sub>3</sub>COOH, and CH<sub>3</sub>CH<sub>2</sub>COOH, the polarities of which are 0.728, 0.648, and 0.611. Thus, polarity decreases as CH<sub>x</sub> groups are added to -OH. The same occurs to the OH-containing adsorbates in this study when interacting with 1\*H<sub>2</sub>O (i.e.  $n = 1$ ), so that the strength of their hydrogen bonds with water progressively decreases. Indeed,  $\Omega_{\text{OH}} = -0.58$  eV, while  $\Omega_{\text{COH}} = -0.45$  eV, and \*CHOH, \*CH<sub>2</sub>OH and \*COOH have  $\Omega_i \approx -0.28$  eV. Previous results hinted toward a correlation between the strength of adsorbate-solvent hydrogen bonds, the solvent's polarity and the adsorbate's polarizability<sup>145</sup>.

Table 4.3 summarizes the  $E_{\text{ZPE}}$ , vibrational entropies  $TS_{\text{vib}}$  (at 298.15 K), and the formation energies from CO<sub>2</sub>, ( $\Delta G_f$ ) calculated using the micro-solvation corrections.

**Table 4.3.** Calculated formation energies ( $\Delta G_f$ ) with solvation corrections for intermediates of the CO<sub>2</sub>RR to CO, CH<sub>3</sub>OH, and CH<sub>4</sub>. All values are in eV. Note that Zero-point energies ( $E_{ZPE}$ ) and vibrational contributions to the entropy ( $TS_{vib}$ ) do not depend of the correction and correspond to those of Table 3.2.

Adsorbate	$E_{ZPE}$	$TS_{vib}$	$\Delta G_f / @Cu(111)$	$\Delta G_f / @Cu(100)$	$\Delta G_f / @Cu(110)$
*COOH	0.62	0.22	0.71	0.54	0.33
*CO	0.16	0.14	0.06	0.16	0.01
*CHO	0.46	0.14	1.11	0.90	0.84
*CH <sub>2</sub> O	0.74	0.15	0.76	0.48	0.41
*CH <sub>3</sub> O	1.08	0.22	-0.03	-0.15	-0.33
*CH <sub>2</sub> OH	1.06	0.21	0.81	0.67	0.42
*O	0.06	0.06	-0.48	-0.76	-0.75
*OH	0.35	0.10	-1.27	-1.42	-2.53
*COH	0.46	0.15	0.89	0.74	0.84
*CHOH	0.76	0.18	1.09	1.08	0.80
*C	0.09	0.03	2.08	0.85	1.41
*CH	0.33	0.05	0.82	0.32	0.80
*CH <sub>2</sub>	0.55	0.09	0.45	0.38	0.22
*CH <sub>3</sub>	0.90	0.15	-0.18	-0.20	-0.52

In Figure 4.2 a) and b) we present the most favorable energy diagrams from CO<sub>2</sub> to \*CH<sub>4</sub> on Cu(111), Cu(100), and Cu(110), obtained using this method.



**Figure 4.2. a)** Most favorable free-energy diagrams for the CO<sub>2</sub>RR to CH<sub>4</sub> on Cu(111) (orange), Cu(100) (red), and Cu(110) (blue) at 0 V vs RHE.

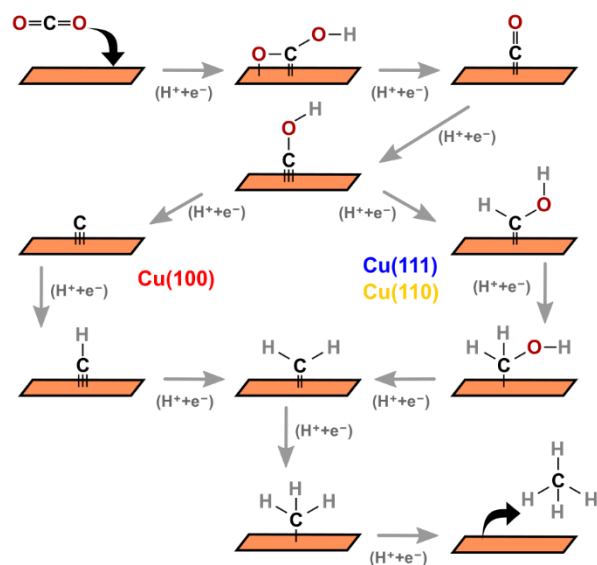


**Figure 4.2. b)** Schematics of the lowest-energy pathways to CH<sub>4</sub> found applying the micro-solvation method described in this work. There is a bifurcation upon \*COH hydrogenation to form either \*C (on Cu(100)) or \*CHOH (on Cu(111) and Cu(110)), and the separate pathways reunite on \*CH<sub>2</sub>.

Early computational studies based only on Gibbs energies<sup>39, 55</sup> and also those that incorporate the kinetic barriers<sup>177, 178</sup> of CO<sub>2</sub>RR, predicted the \*CO hydrogenation to \*CHO as the potential-determining step (PDS). By applying the solvation corrections found for Cu(111) to the other Cu facets, we observe that \*CO is hydrogenated to \*COH instead of \*CHO in all cases.

Two key experimental features to consider are the modest formation of methanol during CO<sub>2</sub>RR and the reduction of CH<sub>2</sub>O<sub>(g)</sub> almost exclusively to CH<sub>3</sub>OH<sup>179</sup>. Therefore, the reaction pathway to CH<sub>4</sub> should not proceed through \*CH<sub>2</sub>O, in contrast with early computational predictions<sup>39, 55</sup>. In agreement with these experimental observations, no pathway to CH<sub>4</sub> in Figure 4.2 goes via \*CH<sub>2</sub>O.

As can be seen, by using ad hoc solvation corrections<sup>36, 39</sup> it was predicted that \*CHO would predominate over \*COH on Cu. However, this trend was reversed when the strong hydrogen bonds between \*COH and water molecules and the weak stabilization

of \*CHO were considered. We note that similar arguments have been put forward for the stability of \*COH vs \*CHO on Pt<sup>103, 133, 180, 181</sup>.

Although \*CHO has a more negative adsorption energy than \*COH in vacuum, the strong hydrogen bonding with H<sub>2</sub>O makes \*COH more stable in solution (energies in vacuum in Table 4.1 and in solution in Table 4.3). Our thermodynamic results agree with those of more elaborate computational studies including kinetics of the electrochemical steps, which also predict the formation of \*COH<sup>101, 103, 181-183</sup>. This important observation will be assessed later in chapter 5, comparing the reaction mechanisms with experimental data and showing how CO<sub>2</sub> reduction to CH<sub>4</sub> on Cu occurs via two different potential-dependent pathways.

Nevertheless, at this point it is also important to verify if the micro-solvation method developed also improves the quantitative predictions of the onset potentials of CO<sub>2</sub>RR and associated reactions on transition metals other than Cu.

### 4.3. Micro-solvated CO<sub>2</sub>RR on other transition metals

We have used the calculated value of  $\Omega_{\text{H}_2\text{O}}^{\text{HB}}$  on Cu, Au, Ag and Zn (see Table 3.1) to evaluate the number of hydrogen-bonded water molecules ( $n$ ) and their contribution to the adsorption energies ( $\Omega_{\text{A}}$ ) for the following reactions: CO<sub>2</sub>RR to CH<sub>4</sub> on Cu single-crystal electrodes<sup>117, 184, 185</sup>, CO<sub>2</sub>RR to CO on polycrystalline (poly) and/or single-crystal electrodes of Cu, Ag, Au, and Zn<sup>114, 186-188</sup>, CO<sub>2</sub>RR to CH<sub>3</sub>OH on polycrystalline Cu<sup>114</sup>, CO reduction to CH<sub>4</sub> on Cu(100)<sup>44</sup>, and CH<sub>2</sub>O reduction to CH<sub>3</sub>OH on polycrystalline Cu<sup>179</sup>.

To represent polycrystalline electrodes, we calculated several facets and took the earliest onset potentials in each case. For the calculations on Ag and Au, the following surfaces were used: Ag(111), Ag(110), Ag(211), Au(111), Au(110), Au(211). For Zn we calculated Zn(0001) and fcc Zn(211), which was used as a proxy to a Zn stepped surface.

Onset potentials were calculated as described in section 1.2.7 for the CO<sub>2</sub>RR to produce CH<sub>4</sub>, CH<sub>3</sub>OH and CO, CORR to CH<sub>4</sub>, and CH<sub>2</sub>O reduction to CH<sub>3</sub>OH on Cu. Figure 4.3. we present a comparison of the calculated onset potentials and previously reported experimental values for these reactions. The specific values for Cu are in previous section (Tables 4.2 and 4.3), experimental onset potentials and specific values for the other metals are at the end of this section (Tables 4.4 to 4.6).

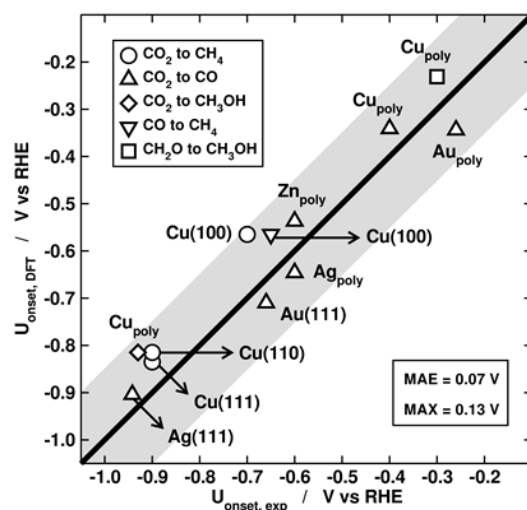


**Figure 4.3.** Parity plot for the calculated (y-axis) and experimental (x-axis) onset potentials  $U_{\text{onset}}$  (V vs RHE) on different transition metals for CO<sub>2</sub>RR to produce CH<sub>4</sub>, CH<sub>3</sub>OH and CO; CORR to CH<sub>4</sub>; and CH<sub>2</sub>O reduction to CH<sub>3</sub>OH. Experimental data taken from<sup>44, 76, 114, 117, 184, 186-188</sup>. Error bands of  $\pm 0.15$  V surround the parity line.

In all cases in Figure 4.3, the data obtained using the proposed method show good agreement with experimental values, being the mean absolute error (MAE) only 0.07 V and the maximum absolute error (MAX) 0.13 V in a window of potentials of  $\sim 0.7$  V. To compare the proposed method to different solvation methods available in the literature (implicit solvation<sup>149</sup>, Ad hoc<sup>154</sup>, and Ad hoc 2<sup>36, 39</sup>), in Figure 4.4 we present the results of calculations using these solvation approaches. MAEs and MAXs obtained are shown in Figure 4.5. We observe a MAE of 0.25 V when neglecting solvation, and MAEs around 0.11-0.16 V when other solvation methods were applied.

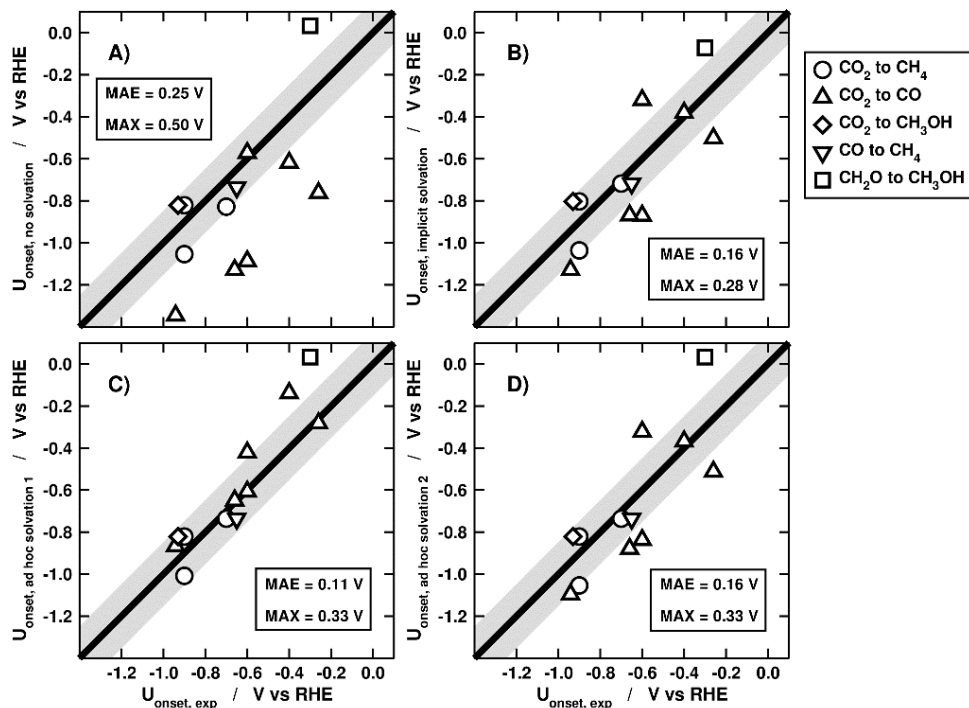


**Figure 4.4.** Parity plots for calculated (y-axis) and experimental<sup>44, 76, 114, 117, 184</sup> (x-axis) onset potentials ( $U_{\text{onset}}$ ) of CO<sub>2</sub>RR to produce CH<sub>4</sub>, CH<sub>3</sub>OH and CO; CORR to CH<sub>4</sub>; and CH<sub>2</sub>O reduction to CH<sub>3</sub>OH. A) No solvation included (in vacuum). B) Solvation included using an implicit method<sup>149</sup>, C) Ad hoc 1<sup>54</sup> corrections. D) Ad hoc 2<sup>36, 39</sup> corrections. Error bands of  $\pm 0.15$  V surround the parity line.

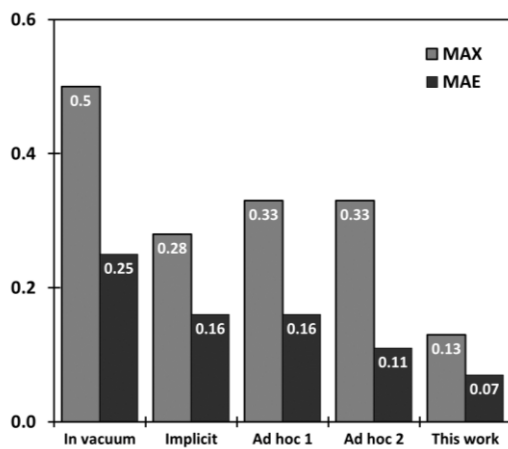


**Figure 4.5.** Mean absolute error (MAE) and maximum absolute error (MAX) of the calculated onset potentials compared to experimental measurements<sup>44, 76, 114, 117, 184</sup>. We include the case where no solvation corrections were applied, and also the cases where solvation was included implicitly<sup>149</sup>, or adding the Ad hoc 1<sup>54</sup>, Ad hoc 2<sup>36, 39</sup>, or our solvation corrections<sup>2</sup>.

The discrepancies between the solvation approaches may lead to mispredictions of the intermediates and onset potentials of electrocatalytic reactions. Therefore, not only neglecting solvation induces large errors in the predictions, the quality of the predictions eventually depends on the applied solvation corrections.

**Table 4.4.** Experimental onset potentials ( $U_{\text{onset}}$  in V vs RHE) for CO<sub>2</sub>RR and associated reactions on various electrodes.

Electrode and reaction	$U_{\text{onset}}$	Electrolyte (pH)	Data source
Cu(111), CO <sub>2</sub> RR to CH <sub>4</sub>	-0.90	0.1 M KHCO <sub>3</sub> (pH = 6.8)	184
Cu(100) CO <sub>2</sub> RR to CH <sub>4</sub>	-0.70	0.2 M phosphate buffers (pH = 7.0)	117
Cu(110) CO <sub>2</sub> RR to CH <sub>4</sub>	-0.90	0.1 M KHCO <sub>3</sub> (pH = 6.8)	184
Cu <sub>poly</sub> CO <sub>2</sub> RR to CO	-0.40	0.1 M KHCO <sub>3</sub> (pH = 6.8)	114
Ag <sub>poly</sub> CO <sub>2</sub> RR to CO	-0.60	0.1 M KHCO <sub>3</sub> (pH = 6.8)	186
Zn <sub>poly</sub> CO <sub>2</sub> RR to CO	-0.60	0.1 M KHCO <sub>3</sub> (pH = 6.8)	114
Au <sub>poly</sub> CO <sub>2</sub> RR to CO	-0.26	0.1 M KHCO <sub>3</sub> (pH = 6.8)	114
Au(111) CO <sub>2</sub> to CO	-0.66	0.1 M KHCO <sub>3</sub> (pH = 6.8)	187
Ag(111) CO <sub>2</sub> to CO	-0.94	0.1 M KHCO <sub>3</sub> (pH = 6.8)	188
Cu(100) CORR to CH <sub>4</sub>	-0.65	0.1 M KOH (pH = 13)	44
Cu <sub>poly</sub> CO <sub>2</sub> RR to CH <sub>3</sub> OH	-0.93	0.1 M KHCO <sub>3</sub> (pH = 6.8)	114
Cu <sub>poly</sub> CH <sub>2</sub> O to CH <sub>3</sub> OH	-0.30	0.2 M phosphate buffers (pH = 7.0)	179

**Table 4.5.** For \*COOH, we report: Zero-point energies ( $E_{\text{ZPE}}$ ), vibrational contributions to the entropy ( $TS_{\text{vib}}$ ), solvation corrections calculated with the presented method ( $\Omega_{\text{this work}}$ ), with an implicit method ( $\Omega_{\text{implicit}}$ ), and those of the ad hoc methods 1 and 2 ( $\Omega_{\text{ad hoc 1/2}}$ ), and formation energies ( $\Delta G_f$ ,  $\Delta G_f$ ) on various facets of Ag, Au, and Zn. (Values in eV)

Surface	$E_{\text{ZPE}}$	$TS_{\text{vib}}$	$\Omega$	$\Omega$	$\Omega$	$\Delta G_f$	$\Delta G_f$	$\Delta G_f$
			<i>this work</i>	<i>implicit</i>	<i>ad hoc 1 / 2</i>	<i>this work</i>	<i>implicit</i>	<i>ad hoc 1 / 2</i>
Ag(111)	0.59	0.26	-0.44	-0.22	-0.48 / -0.25	0.90	1.13	0.87 / 1.10
Ag(110)	0.59	0.28	-0.44	-0.22	-0.48 / -0.25	0.65	0.87	0.61 / 0.84
Au(111)	0.60	0.34	-0.42	-0.26	-0.48 / -0.25	0.71	0.87	0.65 / 0.88
Au(211)	0.60	0.34	-0.42	-0.26	-0.48 / -0.25	0.34	0.50	0.28 / 0.51
Zn(0001)	0.62	0.22	-0.50	-0.25	-0.48 / -0.25	0.84	1.08	0.85 / 1.08
Zn(211)	0.63	0.21	-0.50	-0.25	-0.48 / -0.25	0.08	0.32	0.09 / 0.32
Average	0.61	0.28	-0.45	-0.24	-0.48 / -0.25	-	-	-

**Table 4.6.** For \*CO, we report: Zero-point energies ( $E_{\text{ZPE}}$ ), vibrational contributions to the entropy ( $TS_{\text{vib}}$ ), solvation corrections calculated with the presented method ( $\Omega_{\text{this work}}$ ), with an implicit method ( $\Omega_{\text{implicit}}$ ), and those of the ad hoc methods 1 and 2 ( $\Omega_{\text{ad hoc 1/2}}$ ), and formation energies ( $\Delta G_{f, \text{this work}}$ ,  $\Delta G_{f, \text{implicit}}$ ,  $\Delta G_{f, \text{ad hoc 1/2}}$ ) on various facets of Ag, Au, and Zn. All values are in eV.

Surface	$E_{\text{ZPE}}$	$TS_{\text{vib}}$	$\Omega$ <i>this work</i>	$\Omega$ <i>implicit</i>	$\Omega$ <i>ad hoc 1 / 2</i>	$\Delta G_f$ <i>this work</i>	$\Delta G_f$ <i>implicit</i>	$\Delta G_f$ <i>ad hoc 1 / 2</i>
Ag(111)	0.16	0.26	0.00	0.00	-0.10 / -0.10	0.66	0.66	0.56 / 0.56
Ag(110)	0.16	0.25	0.00	0.00	-0.10 / -0.10	0.52	0.51	0.42 / 0.42
Au(111)	0.17	0.15	0.00	-0.05	-0.10 / -0.10	0.70	0.65	0.60 / 0.60
Au(211)	0.18	0.22	0.00	-0.05	-0.10 / -0.10	0.26	0.21	0.16 / 0.16
Zn(0001)	0.17	0.22	0.00	-0.04	-0.10 / -0.10	0.80	0.76	0.70 / 0.70
Zn(211)	0.17	0.17	0.00	-0.04	-0.10 / -0.10	0.61	0.58	0.51 / 0.51
Average	0.17	0.21	0.00	-0.03	-0.10 / -0.10	-	-	-

Note that each adsorbate on each metal has different solvation corrections, for instance,  $\Omega_{\text{COOH}}$  on Cu is -0.28 eV (Table 4.2), whereas it is -0.42 eV for Au, -0.44 eV for Ag, and -0.50 eV for Zn, (Tables 4.5). Recent works have shown that extrapolating the solvation corrections of a given adsorbate from one material to the next is not always advisable<sup>46, 142, 173, 189</sup>. And our results also attest to that.

#### 4.4. Evaluating dispersion effects

Recent works on micro-solvation have shown that only the first solvation shell of the adsorbate is needed to get a fair estimation of its solvation correction on Pt<sup>173</sup>. We evaluated this on Cu(111) by comparing  $\Omega_{\text{OH}}$  in a periodic water bilayer and in a micro-solvated environment (with and without dispersion corrections<sup>190</sup>, as well as with and without an implicit medium<sup>149</sup>). Since there are no sizable differences between the values of  $\Omega_{\text{OH}}$  obtained in a micro-solvated environment and a full water layer combined with an implicit solvent, without any loss of generality,  $n$  corresponds in the following analysis to the adsorbate’s first solvation shell (more precisely, to the number of water molecules connected to the adsorbate by hydrogen bonds). Our model assumes that the surface is large enough to accommodate \*A, that there are enough water

molecules in the system to solvate it and that the coverage of \*A enables its full solvation.

We have verified that the use of PBE and accounting only for the first solvation shell do not induce large errors in our approach. To do so, we compared the results of PBE to those obtained with the DFT-D3 method developed by Grimme et al<sup>190</sup>, as implemented in the VASP code, and the solvation corrections using the first solvation shell and a full water bilayer. We have taken \*OH as a case study. A 3×3 Cu(111) slab with 4 atomic layers (denoted 3×3×4) was used for the simulations. The dimensions of the cell were chosen to ensure that the adsorbed cluster did not interact with itself when periodic boundary conditions were applied. First, we simulated the first solvation shell of \*OH on the Cu slab, as is shown in (4.1).



The reaction energy of that process is  $\Delta G_{OH}^{MS}$ ,

$$\Delta G_{OH}^{MS} = \Delta G_{4^*H_2O} - \Delta G_{^*OH} - \Delta G_{3^*H_2O} - \Delta G_{(H^+ + e^-)} \quad (4.2)$$

where MS stands for micro-solvation to comply with the notation in ref<sup>173</sup>. Subsequently, the calculations were performed including a full (i.e. periodic) water layer on the same Cu slab, which can be described using the following the reaction:



The reaction energy of that process is  $\Delta G_{OH}^{WB}$ ,

$$\Delta G_{OH}^{WB} = \Delta G_{6^*H_2O} - \Delta G_{^*OH} - \Delta G_{5^*H_2O} - \Delta G_{(H^+ + e^-)} \quad (4.4)$$

where WB stands for water bilayer. In Figure 4.6. the configurations of both systems used to model solvated \*OH are shown. Note that the configurations for the water-only clusters to the left of (equation 4.1 and equation 4.3) are rather like those in Figure 4.6 and differ mostly on the fact that the central molecules are \*H<sub>2</sub>O instead of \*OH.

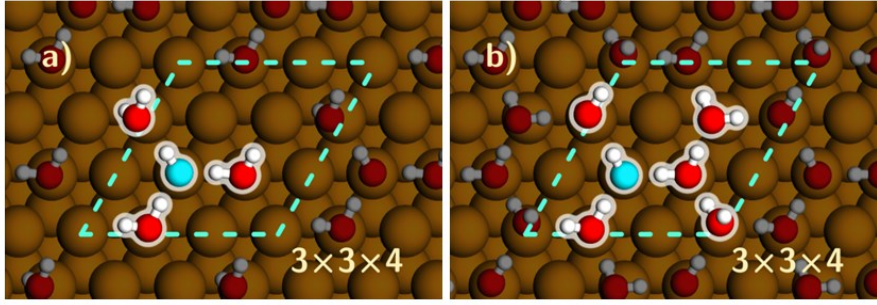


**Figure 4.6.** Top views of the two systems considered for the dispersion analysis of \*OH on Cu(111). H and O atoms are shown in white and red. Cu atoms are shown in different purple and pink shades depending on the layer. Adsorbed clusters included on each periodic cell are highlighted. a) \*OH, on a top site including only its first solvation shell ( $3^*H_2O$ ). b) \*OH, with a complete layer of adsorbed water molecules ( $5^*H_2O$ ). In both cases, we used  $3 \times 3 \times 4$  Cu(111) super-cells.

When comparing the solvation correction calculated with a full water bilayer ( $\Omega_{OH}^{WB}$ ) to the one obtained using only the first solvation shell ( $\Omega_{OH}^{MS}$ ) for a given level of theory, e.g. PBE, the difference should be close to zero if the first shell is indeed enough to capture the essence of solvation:

$$\Delta\Omega^i = \Omega_{OH}^{WB,i} - \Omega_{OH}^{MS,i} \approx 0 \quad (4.5)$$

Equation (4.5) should also hold if dispersion corrections are not strictly necessary for a fair assessment of the solvation corrections. On the other hand, one can show that the difference between the solvation corrections calculated with the full water bilayer and the first solvation shell is:

$$\Delta\Omega = \Delta G_{OH}^{WB} - \Delta G_{OH}^{MS} \quad (4.6)$$

As can be seen in Table 4.7,  $\Delta G_{OH}^{WB}$  changes from 0.04 to  $-0.12$  eV when including D3 dispersion corrections. Similarly,  $\Delta G_{OH}^{MS}$  changes from 0.08 to  $-0.05$  eV when including D3 dispersion corrections. These changes are expectable, as dispersion stabilizes water adsorption<sup>171, 173</sup>. However,  $\Delta\Omega$  is close to zero in both cases, which shows that there are no sizable differences in using all the molecules of the water layer

or using only the first solvation shell of the adsorbate, with or without including dispersion corrections.

**Table 4.7.** Adsorption and solvation corrections of \*OH within a full water bilayer (WB) and including the first solvation shell (MS) only. All values are in eV.

Method	$\Delta G_{\text{OH}}^{\text{WB}}$	$\Delta G_{\text{OH}}^{\text{MS}}$	$\Delta\Omega$
PBE	0.04	0.08	-0.04
PBE+D3	-0.12	-0.05	-0.07

Moreover, in Table 4.8 we provide results for a water bilayer with/without an implicit solvent (VASPsol<sup>149</sup>) in the calculations, the micro-solvation environment with/without an implicit solvent, and an implicit solvent with no explicit H<sub>2</sub>O molecules in the simulation.

**Table 4.8.** Adsorption energies of \*OH within an explicit full water bilayer with and without implicit solvation (WBI, WB, respectively), in the micro-solvation environment with and without implicit solvation (MSI, MS, respectively), and with implicit solvation only (I). All values are in eV and calculated using PBE.

Adsorbate	$\Delta G_{\text{OH}}^{\text{WB}}$	$\Delta G_{\text{OH}}^{\text{WBI}}$	$\Delta G_{\text{OH}}^{\text{MS}}$	$\Delta G_{\text{OH}}^{\text{MSI}}$	$\Delta G_{\text{OH}}^{\text{I}}$
*OH	0.04	0.12	0.08	0.05	0.86

The results in Table 4.8 hint toward two facts: first, the implicit solvent provided by VASPsol does not capture hydrogen bonds, as all values from calculations including some degree of explicit water are in the narrow range of 0.04-0.12 eV, and the result of the implicit method is considerably more positive (0.86 eV). Second, the micro-solvation environment approximates well the results of a more complete simulation including a full bilayer combined with an implicit medium; their difference for \*OH is 0.04 eV ( $\Delta G_{\text{OH}}^{\text{WBI}} - \Delta G_{\text{OH}}^{\text{MS}} = 0.12 - 0.08 = 0.04$  eV).

## 4.5. Estimation of solvation contributions using DFT energies

The method developed in chapter 3 calculates the solvation corrections  $\Omega_i$  directly from the differences in  $\Delta E_{\text{DFT}}$  instead of the full expression for  $\Delta G$ , that is, including  $E_{\text{ZPE}}$  and TS corrections. Thus, it is important to assess the validity of the approximation  $\Delta E_{\text{ZPE}} - T\Delta S \approx 0$  for the adsorption systems under study. \*COH is used as an example to show the effect of these corrections on the solvation contributions. As  $n = 1$  for \*COH, the process and the solvation contribution can be written respectively as:



$$\Omega_{\text{COH}} = \Delta G_{\text{f}}^{*\text{COH}+1*\text{H}_2\text{O}} - \Delta G_{\text{f}}^{*\text{COH}} - \Delta G_{\text{f}}^{*+1*\text{H}_2\text{O}} \quad (4.8)$$

According to the method developed in chapter 3, this was approximated as:

$$\Omega_{\text{COH}} \approx \Delta E_{\text{f}}^{*\text{COH}+1*\text{H}_2\text{O}} - \Delta E_{\text{f}}^{*\text{COH}} - \Delta E_{\text{f}}^{*+1*\text{H}_2\text{O}} \quad (4.9)$$

Table 4.9 shows the DFT and Gibbs energies of formation for this adsorbate-water system. The solvation correction of \*COH without accounting for  $E_{\text{ZPE}}$  and TS (equation 4.9) is  $\Omega_{\text{COH}} = 0.06 - 0.68 - (-0.17) = -0.45$  eV. Analogously, the solvation correction of \*COH accounting  $E_{\text{ZPE}}$  and TS (equation 4.6) is  $\Omega_{\text{COH}} = 1.36 - 1.45 - 0.36 = -0.45$  eV (values taken from the fifth column of Table 4.6). This suggests that zero-point energy and entropy corrections can be safely neglected when computing solvation corrections with the proposed method. Indeed, we find that  $\Delta E_{\text{ZPE}} = -0.03$  eV and  $T\Delta S_{\text{vib}} = -0.03$  eV, thus  $\Delta E_{\text{ZPE}} - T\Delta S_{\text{vib}} = 0$ .

**Table 4.9.** Zero-point energy and vibrational entropy contributions to the adsorption energies of \*COH solvated by 1\*H<sub>2</sub>O and in vacuum. All values are in eV.

Description	$E_{\text{ZPE}}$	$TS_{\text{vib}}$	$\Delta E_{\text{f}}$	$\Delta G_{\text{f}}$
*COH + 1*H <sub>2</sub> O	1.07	0.32	0.06	1.36
*COH	0.46	0.15	0.68	1.45
* + 1*H <sub>2</sub> O	0.63	0.20	-0.17	0.36
*	-	-	0.00	0.00

## 4.6. Evaluation of the work function

Finally, we calculated the changes in work function upon water co-adsorption on Cu(111) with \*COH adsorbed in vacuum, [\*COH + 1\*H<sub>2</sub>O], and [\*COH + 2\*H<sub>2</sub>O]. The obtained values were 4.68, 4.67, and 4.68 eV, respectively. Thus, we can conclude that in this case the work function does not significantly change as the number of adsorbed water molecules is moderately increased.

## Summary

In this chapter, we successfully applied our micro-solvation model to CO<sub>2</sub>RR on Cu and other transition metals. We used the same solvation corrections between facets of the same metal, and we found no apparent inconvenience. The discrepancies of some solvation approaches were evaluated, and it was found that by applying this method, the MAE and MAX errors in the onset potential calculations decrease. Our results also show that the magnitudes of the solvation interactions are significant for accurate modeling of the reaction.

However, the solvation energies for the same adsorbates may drastically change among metals. Therefore, opposite to common ad hoc solvation practices, we do not encourage the extrapolation of solvation corrections obtained for a given metal to another, since solvation energies not only depend on the adsorbate but also depend on the metal used.

Additionally, for the estimation of the solvation corrections, the dispersion effects, vibrational contributions to the entropy for  $\Omega$ , and work function changes were neglected. We have found that this is a safe approximation for small adsorbates, but we recommend a careful analysis of these considerations if different adsorbates are evaluated.

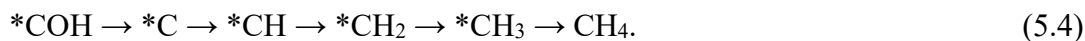
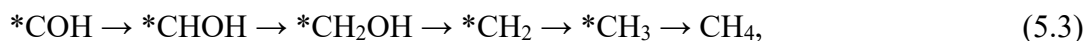
Our results of CO<sub>2</sub>RR on Cu using the micro-solvation method, suggest the formation of \*COH, agreeing with more elaborate computational studies. In the next chapter we explore in deep this observation and the subsequent catalytic routes enabled through this key reaction intermediate.

## Chapter 5. Analysis of the deactivation of Cu catalysts during CO<sub>2</sub>RR to CH<sub>4</sub>

---

The deactivation of Cu electrodes during long-term operation significantly affects the scalability and deployment of CO<sub>2</sub> electrolyzers. It has been observed that Cu surfaces that tend to deactivate are often CH<sub>4</sub>-selective<sup>191</sup>. On the other hand, oxide-derived Cu catalysts (OD-Cu), which reduce CO<sub>2</sub> dominantly to ethylene and ethanol, do not tend to deactivate rapidly<sup>192, 193</sup>. These facts suggest that there are reaction pathways in CO<sub>2</sub>RR that promote the deactivation, producing reaction intermediates that poison the surface. Moreover, such pathways should operate particularly while producing C<sub>1</sub> species, like CH<sub>4</sub>. A similar behavior has been often observed in gas-phase thermal catalysis<sup>194</sup>. However, in the field of CO<sub>2</sub>RR this possibility has been generally side-stepped.

Many possible routes to CH<sub>4</sub> have been suggested in literature<sup>39, 101, 183, 195-197</sup>. Starting from the \*CO hydrogenation products, they are:



Equation (5.4) shows that CO<sub>2</sub>RR can lead to \*C and \*CH, both of which could polymerize, thereby coking the electrode. However, few studies have suggested that CO<sub>2</sub> reduces to graphitic carbon<sup>198-200</sup>, and deactivation of Cu catalysts has been generally attributed to the cathodic deposition of Fe and Zn contaminants from the electrolyte onto the Cu cathode during CO<sub>2</sub>RR<sup>201</sup>, or to surface restructuring after operation<sup>202</sup>. Most common strategies to mitigate Cu deactivation, include the use of

ultrapure salts for preparing the electrolytes and cation-exchange resins to scavenge for these trace metal ions<sup>203</sup>.

The following sections contain the experimental results of the CO<sub>2</sub>RR on Cu electrodes<sup>3</sup> (Cu(100), Cu(110), and Cu(111) surfaces), and provide a joint theoretical-experimental analysis of the facet- and potential-dependent Cu deactivation pathways.

## 5.1. Experimental CO<sub>2</sub>RR on polycrystalline and single-crystal Cu facets

Experimental measurements of CO<sub>2</sub>RR activity were performed on different Cu electrodes\*. The results are condensed in Table 5.1.

**Table 5.1.** Summary of the chronoamperometric behavior of the CO<sub>2</sub>RR in aqueous 0.1 M KHCO<sub>3</sub> electrolyte measured over a two-hour period on polycrystalline Cu (Cu<sub>poly</sub>), Cu(111) and Cu(100) electrodes at -0.90, -1.05 and -1.20 V vs RHE<sup>3</sup>. (Averages of three sets of measurements).

Applied V	Cu <sub>poly</sub>	Cu(100)	Cu(111)
-0.90 V vs RHE	Small activity, $j_{\text{CH}_4}$ from -0.01 to -0.03 mA cm <sup>-2</sup>	Deactivation of 67%, $j_{\text{CH}_4}$ from -0.037 to -0.012 mA cm <sup>-2</sup>	Negligible activity
-1.05 V vs RHE	Deactivation of 66%, $j_{\text{CH}_4}$ from -2.3 to -0.8 mA cm <sup>-2</sup>	Deactivation of 57%, $j_{\text{CH}_4}$ from -3.0 to -1.3 mA cm <sup>-2</sup>	Deactivation of 89%, $j_{\text{CH}_4}$ from -0.92 to -0.10 mA cm <sup>-2</sup>
-1.20 V vs RHE	Not deactivated, average $j_{\text{CH}_4}$ of 11.1 mA cm <sup>-2</sup>	Not deactivated, average $j_{\text{CH}_4}$ of -10.0 mA cm <sup>-2</sup>	Deactivation of 62%, $j_{\text{CH}_4}$ from -11.3 to -4.4 mA cm <sup>-2</sup>

\* Experimental measurements were performed in collaboration with Qi Hang Low, Samantha Hui Lee Hong, and Professor Boon Siang Yeo, from the Solar Energy Research Institute of Singapore (SERIS), at National University of Singapore.

To identify the causes of Cu deactivation, a thorough characterization of the electrolyte and of Cu surfaces after CO<sub>2</sub>RR of Cu electrodes was done. Table 5.2 summarizes the main results of such analyses.

**Table 5.2.** Main characterization results after CO<sub>2</sub>RR for the aqueous 0.1 M KHCO<sub>3</sub> electrolyte and polycrystalline Cu (Cu<sub>poly</sub>), Cu(111) and Cu(100) electrodes.

Component	Technique	Parameters	Results
Electrolyte (0.1 M KHCO <sub>3</sub> )	ICP-OES: Plasma-Optical Emission Spectroscopy	Detection limit: ~ 0.003 ppm	No presence of metal contaminants
Cu <sub>poly</sub>	XPS: X-ray Photoelectron Spectroscopy	Energy regions: Zn: 1010-1050 eV Ni: 840-880 eV Fe: 40-70 eV	No signals observed in these regions
Single crystals Cu(100) Cu(111)	CV: Cyclic Voltammetry	Scan rate: 50 mV/s	Similar CVs. Surface orientation mainly unchanged.

The measurements in Tables 5.1 and 5.2 indicate that the deactivation of Cu electrodes did not result from changes in surface crystallography or the presence of metal contaminants on the catalyst. Instead, deactivation may be a consequence of coking by the generation of reaction intermediates during CO<sub>2</sub> electrolysis. As can be seen in Table 5.1, such deactivation is potential- and facet-dependent: the onset potential for the constant production of CH<sub>4</sub> is less negative on Cu(100) (-1.05 V vs RHE) compared to Cu(111) (-1.20 V vs RHE). Since changes in surface structure and poisoning by trace metals can be ruled out as the causes of this phenomenon, the evidence hints toward mechanistic formation of graphite during the catalytic cycles of CO<sub>2</sub>RR. We postulate that the “coking” pathway dominates at low applied overpotential, and at high applied overpotential there appears to be a non-coking pathway, where \*C (common cause for coking) is not formed during CH<sub>4</sub> production.

## 5.2. Combining theory and experiments to analyze Cu deactivation

Schematics of the CO<sub>2</sub>RR pathways to CH<sub>4</sub> on Cu are shown in Figure 5.1.

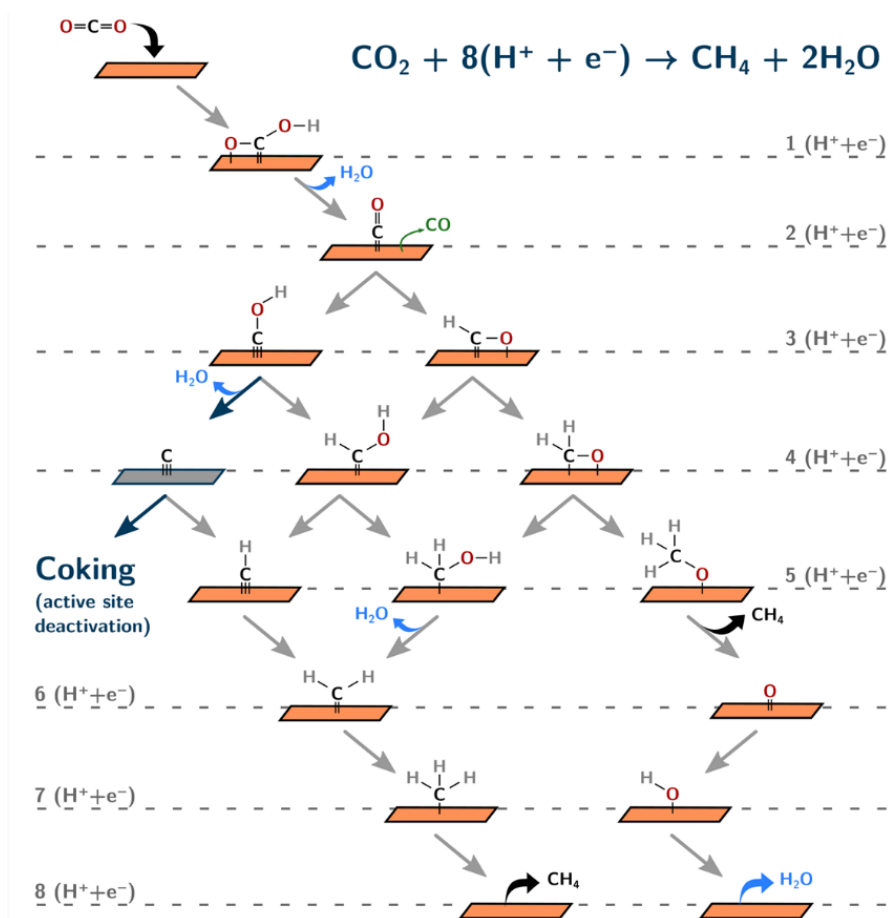


**Figure 5.1.** Schematics of the CO<sub>2</sub>RR to CH<sub>4</sub> on Cu electrodes. The bifurcation between the non-coking (right, via \*CHO) and coking (left, via \*COH) pathways occurs during \*CO hydrogenation. Steps along the reaction network are electrochemical, as the barriers of chemical steps for C-O bond scissions are considerably larger than the corresponding electrochemical barriers<sup>37, 195, 204</sup>.

CH<sub>4</sub> evolution on Cu likely proceeds via two different pathways as the potential is varied. The two pathways diverge from \*CO hydrogenation, as \*COH or \*CHO can be formed. At less negative potentials, CH<sub>4</sub> production proceeds through a mechanism that deactivates the electrode. At more negative potentials, an additional mechanism for CH<sub>4</sub> evolution, that does not poison the electrode, is opened. Importantly, the

analysis proceeds by reconsidering the usual experimental approximation that the symmetry factors (see section 1.2.8) of electrochemical steps ( $\beta_i$ ) are identical and equal to a half<sup>205</sup>.

The coking pathway proceeds via \*COH (route (d) mentioned before), and we suggest that \*C, rather than \*CH, is the coking species, as the formation of acetylene has not been reported on Cu during CO<sub>2</sub>RR<sup>67, 69, 206</sup>. On the other hand, a pathway via \*CHO will likely form \*CHOH<sup>69, 195</sup>, which avoids the formation of \*C.

In Figure 5.2, we show the adsorption energies of \*CO, \*CHO, and \*COH on Cu(111) and Cu(100) with respect to \*CO at 0 V vs RHE. The transition states to electroreduce \*CO to \*COH (TS<sub>COH</sub>, black) and \*CHO (TS<sub>CHO</sub>, red) are also shown for the lower-bound case in which the kinetic barriers coincide with the uphill energy differences. However, knowledge of the exact location of the transition states is not required in the following analysis. We will only assume that the thermodynamic differences at 0 V vs RHE of the transition states are equivalent to those of the final states, as is shown in Equation (5.1). This assumption is justified by Brønsted-Evans-Polanyi (BEP) relations<sup>3, 37, 207</sup>.

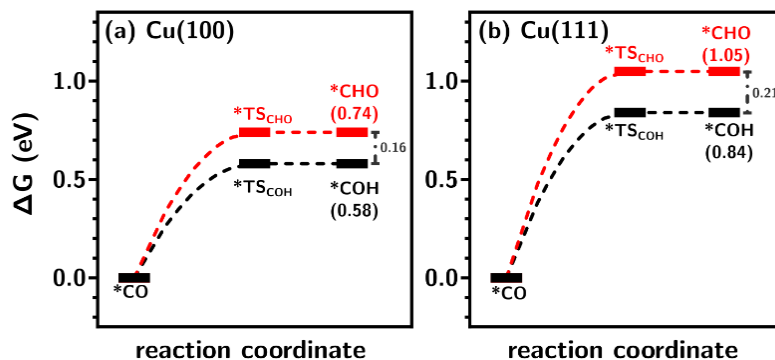


**Figure 5.2.** Gibbs energy diagrams for the hydrogenation of \*CO on (a) Cu(100) and (b) Cu(111) at 0 V vs RHE. The formation of \*COH (black) and \*CHO (red) is shown for both facets. The values in parentheses correspond to the energies of formation calculated with respect to \*CO, protons and electrons. For convenience and without any impact on the analysis, the transition states are set to the lower-bound case in which they are equal to the final states (see text for details). Dashed lines are merely a guide to the eye to connect initial, transition and final states.

$$\Delta G_{\text{TS}_{\text{CHO}}} - \Delta G_{\text{TS}_{\text{COH}}} \approx \Delta G_{\text{CHO}} - \Delta G_{\text{COH}} \quad (5.1)$$

According to Figure 5.2, the thermodynamic differences for the formation of \*COH and \*CHO are 0.16 and 0.21 eV on Cu(100) and Cu(111), respectively (see also Table 4.3). The assumption also seems reasonable when considering that earlier reports on Cu(111) showed differences of 0.25-0.27 eV in the kinetic barriers of \*CHO vs \*COH at 0 V vs RHE<sup>182, 195</sup>. Based on Equation (1.32), the potential-dependent difference of Gibbs energies between the transition states of two competing pathways, namely those via \*CHO and \*COH, is given by Equation (5.2).

$$\Delta G_{\text{TS}_{\text{CHO}}}^{\#} - \Delta G_{\text{TS}_{\text{COH}}}^{\#} \approx \Delta G_{\text{TS}_{\text{CHO}}} - \Delta G_{\text{TS}_{\text{COH}}} + (\beta_{\text{CHO}} - \beta_{\text{COH}})eU \quad (5.2)$$

The left side of this Equation (i.e.  $\Delta G_{\text{TS}_{\text{CHO}}}^{\#} - \Delta G_{\text{TS}_{\text{COH}}}^{\#}$ ) is potential-dependent because the kinetics may change as a function of the applied potential. The difference at the right side,  $\Delta G_{\text{TS}_{\text{CHO}}} - \Delta G_{\text{TS}_{\text{COH}}}$ , is independent of the applied potential and corresponds to the thermodynamic states at 0 V vs RHE. And the potential dependence is incorporated by the last term,  $(\beta_{\text{CHO}} - \beta_{\text{COH}})eU$ .

According to Figure 5.2, at 0 V vs RHE the \*COH-based pathway dominates, but a shift happens when there is a sign change in equation 5.2. In other words, the pathways will shift at the potential for which the difference in the energies of the transition state is zero ( $\Delta G_{\text{TS}_{\text{CHO}}}^{\#} - \Delta G_{\text{TS}_{\text{COH}}}^{\#} = 0$ ). Given that  $\Delta G_{\text{CHO}} - \Delta G_{\text{COH}} > 0$ , in Figure 5.3 this can only happen if  $\beta_{\text{CHO}} > \beta_{\text{COH}}$  and the potential is made increasingly negative. We emphasize that, based on equation 5.2, if the symmetry factors of competing elementary reactions are assumed equal, there should be no pathway shift at different applied potentials. However, if  $\beta_{\text{CHO}} \neq \beta_{\text{COH}}$ , it is possible to calculate the difference in symmetry factors as:

$$\beta_{\text{CHO}} - \beta_{\text{COH}} \approx (\Delta G_{\text{CHO}} - \Delta G_{\text{COH}})/-eU \quad (5.3)$$

Given that deactivation starts declining on Cu(100) at -1.05 V vs RHE and on Cu(111) at -1.20 V vs RHE (see Table 5.1), we conclude from Equation (5.3) that  $(\beta_{\text{CHO}} - \beta_{\text{COH}})_{\text{Cu(100)}} \approx 0.15$  and  $(\beta_{\text{CHO}} - \beta_{\text{COH}})_{\text{Cu(111)}} \approx 0.18$ . We note that equation 5.3 predicts the difference of the symmetry factors for two competing intermediates. To know one of the individual symmetry factors, it is necessary to know or assume the other one. For instance, assuming  $\beta_{\text{COH}} = 0.5$ , equation 5.2 predicts  $\beta_{\text{CHO}} = 0.65$  for Cu(100) and 0.68 for Cu(111). Alternatively, assuming  $\beta_{\text{CHO}} = 0.5$  we obtain  $\beta_{\text{COH}} = 0.35$  for Cu(100) and 0.32 for Cu(111).

These symmetry factors ( $\beta_{\text{COH}} = 0.5$  for both facets,  $\beta_{\text{CHO}} = 0.65$  for Cu(100) and 0.68 for Cu(111)) can be used to modify Figure 5.2 (made at 0 V vs RHE) so as to observe pathway shifts at -1.05 and -1.20 V vs RHE for Cu(100) and Cu(111), respectively. The resulting Gibbs energy diagrams are presented in Figure 5.3 at the applied potential required to shift the mechanisms from \*COH-based (coking pathway) to \*CHO-based (non-coking pathway). Altogether, Figures 5.2 and 5.3 show that thermodynamics makes the CO<sub>2</sub>RR pathway proceed initially via \*COH but, because of the smaller symmetry factors of \*COH, kinetics incline the pathway toward \*CHO as the potential is increasingly negative.

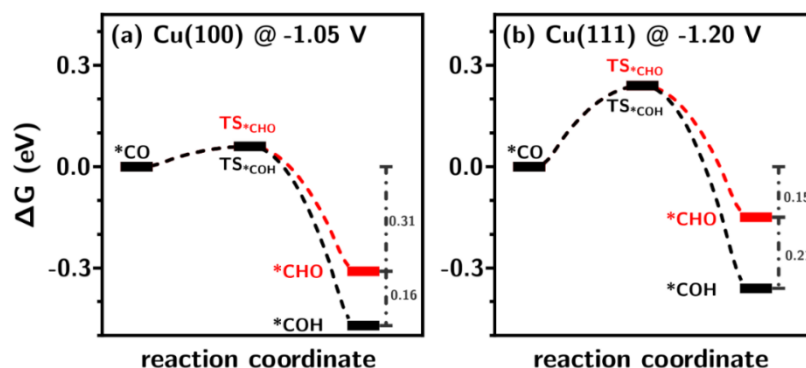


**Figure 5.3.** Gibbs energy diagrams for the hydrogenation of \*CO to \*COH (black) and \*CHO (red) at the potentials for which the non-coking pathway becomes kinetically more favorable than the coking pathway. (a) Cu(100) at -1.05 V vs RHE. (b): Cu(111) at -1.20 V vs RHE. The symmetry factors used are  $\beta_{\text{COH}} = 0.5$  for both Cu(111) and Cu(100), and  $\beta_{\text{CHO}} = 0.68$  for Cu(111) and  $\beta_{\text{CHO}} = 0.65$  for Cu(100). Dashed lines are merely a guide to the eye to connect initial, transition and final states.

The quality of the predictions made with equation 5.2 depends on the accuracy of the calculated adsorption energies in solution, which comprise adsorbate-solvent interactions. While different methods consistently predict low or null solvation stabilization for \*CO in H<sub>2</sub>O, significant differences (~0.2 eV) are observed for \*COH because hydrogen bonding is generally not captured by implicit solvation methods<sup>167, 173, 196</sup>. Thus, it is advisable to account for solvent-adsorbate effects by explicitly including H<sub>2</sub>O in the calculations using method described in Chapter 4.

## Summary

In this chapter we analyzed the two-existing potential-dependent pathways on Cu during CO<sub>2</sub>RR to CH<sub>4</sub> at different potentials. The lower overpotential pathway deactivates the electrodes, whereas the higher overpotential pathway does not. Using experimental findings and our calculations, we illustrate that the deactivation of Cu catalysts may not solely be due to contamination from trace metals, as commonly believed, but it may also be a consequence of a \*COH-based coking pathway. Therefore, to produce CH<sub>4</sub> at low overpotentials without electrode deactivation, it would be advisable to stabilize \*CHO with respect to \*COH and/or increase its symmetry factor.

## Conclusions and future directions

---

The work present in this dissertation explores strategies to improve DFT-based approaches for modeling the CO<sub>2</sub>RR in transition metals. To this aim, some of the most common assumptions and parameters in CO<sub>2</sub>RR modeling were reconsidered and recalculated.

It is well known that computational electrochemistry contributes to a richer understanding of CO<sub>2</sub>RR. However, alongside in-depth explanations of CO<sub>2</sub>RR experiments, the main goal and challenge is still the rational design of cost-effective, efficient and stable materials to be implemented in CO<sub>2</sub> electrolyzers. In this work we show that with the incorporation of new assumptions in calculations, the accuracy and descriptiveness of CO<sub>2</sub>RR models increased, and this not necessarily has a negative impact in computational time.

We present in this work, for the first time, a convenient and systematic method to calculate solvation in electrochemical reactions, in which only thermodynamic calculations are required. This method relies in the fact that the aqueous environment, (which could be the “universe” of in-vacuum DFT systems in terms of the second law) only form hydrogen bonds with adsorbates if such interaction provides a more stable state to the system.

Hence, in contrast to the conventional assumption of constant solvation interactions, we revealed that it is safe to extrapolate corrections to other facets of the same metal, but not between different adsorbates, much less between different metals. Correction values reported here can be used in future related studies of CO<sub>2</sub>RR within the same exchange correlation functional. And our results also served to prove that the errors of the gas phase are also important for the adsorbed phase.

Furthermore, the micro-solvation method could be applied to studies of other reactions with different adsorbates (e.g., with more than one carbon) or using different functionals. It would be interesting to evaluate if the method can be further simplified with energy decomposition models. And It would be also insightful to calculate the electrochemical barriers of CO<sub>2</sub>RR on Cu with the micro-solvated environment.

Our findings also provide an important explanation of deactivation of Cu during CO<sub>2</sub>RR to C<sub>1</sub> products at low overpotentials. Since there are two different potential-dependent pathways and one of them can lead to deactivation. We concluded that to avoid coking it would be advisable to stabilize \*CHO with respect to \*COH and/or increase its symmetry factor, instead of assuming them as equal.

Therefore, to conclude this thesis, I would like to remark that, all the advances obtained in this work arose from a careful approach to the thermodynamics of the electrochemical system.

## References

---

1. Rendón-Calle, A.; Builes, S.; Calle-Vallejo, F., A brief review of the computational modeling of CO<sub>2</sub> electroreduction on Cu electrodes. *Current Opinion in Electrochemistry* **2018**, *9*, 158-165.
2. Rendón-Calle, A.; Builes, S.; Calle-Vallejo, F., Substantial improvement of electrocatalytic predictions by systematic assessment of solvent effects on adsorption energies. *Applied Catalysis B: Environmental* **2020**, 119147.
3. Rendón-Calle, A.; Low, Q. H.; Hong, S. H. L.; Builes, S.; Yeo, B. S.; Calle-Vallejo, F., How symmetry factors cause potential- and facet-dependent pathway shifts during CO<sub>2</sub> reduction to CH<sub>4</sub> on Cu electrodes *Applied Catalysis B: Environmental* **2021**.
4. Granda-Marulanda, L. P.; Rendón-Calle, A.; Builes, S.; Illas, F.; Koper, M. T. M.; Calle-Vallejo, F., A Semiempirical Method to Detect and Correct DFT-Based Gas-Phase Errors and Its Application in Electrocatalysis. *ACS Catalysis* **2020**, 6900-6907.
5. Thijssen, J., *Computational physics*. Cambridge university press: 2007.
6. Sholl, D.; Steckel, J. A., *Density functional theory: a practical introduction*. John Wiley & Sons: 2011.
7. Mardirossian, N.; Head-Gordon, M., Thirty years of density functional theory in computational chemistry: an overview and extensive assessment of 200 density functionals. *Molecular Physics* **2017**, *115* (19), 2315-2372.
8. Burke, K.; Wagner, L. O., DFT in a nutshell. *International Journal of Quantum Chemistry* **2013**, *113* (2), 96-101.
9. Hohenberg, P.; Kohn, W., Inhomogeneous Electron Gas. *Physical Review* **1964**, *136* (3B), B864-B871.
10. Kohn, W.; Sham, L. J., Self-Consistent Equations Including Exchange and Correlation Effects. *Physical Review* **1965**, *140* (4A), A1133-A1138.
11. Levy, M., Electron densities in search of Hamiltonians. *J Physical Review A* **1982**, *26* (3), 1200-1208.
12. Capelle, K., A bird's-eye view of density-functional theory %J Brazilian Journal of Physics. **2006**, *36*, 1318-1343.
13. Becke, A. D., Perspective: Fifty years of density-functional theory in chemical physics. *The Journal of Chemical Physics* **2014**, *140* (18), 18A301.
14. Cramer, C. J., *Essentials of computational chemistry: theories and models*. John Wiley & Sons: 2013.
15. Wang, Y.; Perdew, J. P., Correlation hole of the spin-polarized electron gas, with exact small-wave-vector and high-density scaling. *J Physical Review B* **1991**, *44* (24), 13298-13307.
16. Perdew, J. P.; Burke, K.; Ernzerhof, M., Generalized Gradient Approximation Made Simple. *Physical Review Letters* **1996**, *77* (18), 3865-3868.
17. Ernzerhof, M.; Scuseria, G. E., Assessment of the Perdew–Burke–Ernzerhof exchange-correlation functional. *The Journal of Chemical Physics* **1999**, *110* (11), 5029-5036.
18. Hammer, B.; Hansen, L. B.; Nørskov, J. K., Improved adsorption energetics within density-functional theory using revised Perdew-Burke-Ernzerhof functionals. *J Physical review B* **1999**, *59* (11), 7413-7421.
19. Rushton, P. P. Towards a non-local density functiona description of exchange and correlation. Durham University, 2002.
20. Van Voorhis, T.; Scuseria, G. E., A novel form for the exchange-correlation energy functional. *The Journal of Chemical Physics* **1998**, *109* (2), 400-410.

21. Staroverov, V. N.; Scuseria, G. E.; Tao, J.; Perdew, J. P., Comparative assessment of a new nonempirical density functional: Molecules and hydrogen-bonded complexes. *The Journal of Chemical Physics* **2003**, *119* (23), 12129-12137.
22. Adamo, C.; Barone, V., Toward reliable density functional methods without adjustable parameters: The PBE0 model. *The Journal of Chemical Physics* **1999**, *110* (13), 6158-6170.
23. Becke, A. D., Density-functional thermochemistry. III. The role of exact exchange. *The Journal of Chemical Physics* **1993**, *98* (7), 5648-5652.
24. Lee, C.; Yang, W.; Parr, R. G., Development of the Colle-Salvetti correlation-energy formula into a functional of the electron density. *J Physical review B* **1988**, *37* (2), 785-789.
25. Heyd, J.; Scuseria, G. E.; Ernzerhof, M., Hybrid functionals based on a screened Coulomb potential. **2003**, *118* (18), 8207-8215.
26. Dion, M.; Rydberg, H.; Schröder, E.; Langreth, D. C.; Lundqvist, B. I., Van der Waals Density Functional for General Geometries. *Physical Review Letters* **2004**, *92* (24), 246401.
27. Román-Pérez, G.; Soler, J. M., Efficient Implementation of a van der Waals Density Functional: Application to Double-Wall Carbon Nanotubes. *Physical Review Letters* **2009**, *103* (9), 096102.
28. Wellendorff, J.; Lundgaard, K. T.; Møgelhøj, A.; Petzold, V.; Landis, D. D.; Nørskov, J. K.; Bligaard, T.; Jacobsen, K. W., Density functionals for surface science: Exchange-correlation model development with Bayesian error estimation. *Physical Review B* **2012**, *85* (23), 235149.
29. Furche, F., Molecular tests of the random phase approximation to the exchange-correlation energy functional. *J Physical Review B* **2001**, *64* (19), 195120.
30. Ren, X.; Rinke, P.; Joas, C.; Scheffler, M., Random-phase approximation and its applications in computational chemistry and materials science. *Journal of Materials Science* **2012**, *47* (21), 7447-7471.
31. Perdew, J. P.; Schmidt, K., *Density functional theory and its application to materials*. 2001; p 1-20.
32. Medvedev, M. G.; Bushmarinov, I. S.; Sun, J.; Perdew, J. P.; Lyssenko, K. A., Density functional theory is straying from the path toward the exact functional. **2017**, *355* (6320), 49-52.
33. Sabatier, P., Hydrogénations et déshydrogénations par catalyse. **1911**, *44* (3), 1984-2001.
34. Bagger, A.; Castelli, I. E.; Hansen, M. H.; Rossmeisl, J., Fundamental Atomic Insight in Electrocatalysis. In *Handbook of Materials Modeling: Applications: Current and Emerging Materials*, Andreoni, W.; Yip, S., Eds. Springer International Publishing: Cham, 2020; pp 1473-1503.
35. Trasatti, S., The absolute electrode potential: an explanatory note. *J Pure Appl. Chem* **1986**, *58* (7), 955-966.
36. Nørskov, J. K.; Rossmeisl, J.; Logadottir, A.; Lindqvist, L.; Kitchin, J. R.; Bligaard, T.; Jonsson, H., Origin of the overpotential for oxygen reduction at a fuel-cell cathode. *The Journal of Physical Chemistry B* **2004**, *108* (46), 17886-17892.
37. Wang, S.; Temel, B.; Shen, J.; Jones, G.; Grabow, L. C.; Studt, F.; Bligaard, T.; Abild-Pedersen, F.; Christensen, C. H.; Nørskov, J. K., Universal Brønsted-Evans-Polanyi Relations for C–C, C–O, C–N, N–O, N–N, and O–O Dissociation Reactions. *Catalysis Letters* **2011**, *141* (3), 370-373.
38. Wang, S.; Petzold, V.; Tripkovic, V.; Kleis, J.; Howalt, J. G.; Skúlason, E.; Fernández, E. M.; Hvolbæk, B.; Jones, G.; Toftelund, A.; Falsig, H.; Björketun, M.; Studt, F.; Abild-Pedersen, F.; Rossmeisl, J.; Nørskov, J. K.; Bligaard, T., Universal transition state

scaling relations for (de)hydrogenation over transition metals. *Physical Chemistry Chemical Physics* **2011**, *13* (46), 20760-20765.

39. Peterson, A. A.; Abild-Pedersen, F.; Studt, F.; Rossmeisl, J.; Nørskov, J. K., How copper catalyzes the electroreduction of carbon dioxide into hydrocarbon fuels. *Energy & Environmental Science* **2010**, *3* (9), 1311-1315.

40. Bartel, C. J.; Weimer, A. W.; Lany, S.; Musgrave, C. B.; Holder, A. M., The role of decomposition reactions in assessing first-principles predictions of solid stability. *npj Computational Materials* **2019**, *5* (1), 4.

41. Lide, D. R., *CRC handbook of chemistry and physics*. CRC press: 2004; Vol. 85.

42. Atkins, P. W.; De Paula, J.; Keeler, J., *Atkins' physical chemistry*. Oxford university press: 2018.

43. Akhade, S. A.; McCrum, I. T.; Janik, M. J., The impact of specifically adsorbed ions on the copper-catalyzed electroreduction of CO<sub>2</sub>. *Journal of The Electrochemical Society* **2016**, *163* (6), F477.

44. Pérez-Gallent, E.; Marcandalli, G.; Figueiredo, M. C.; Calle-Vallejo, F.; Koper, M. T., Structure- and Potential-Dependent Cation Effects on CO Reduction at Copper Single-Crystal Electrodes. *Journal of the American Chemical Society* **2017**, *139* (45), 16412-16419.

45. Ringe, S.; Clark, E. L.; Resasco, J.; Walton, A.; Seger, B.; Bell, A. T.; Chan, K., Understanding cation effects in electrochemical CO<sub>2</sub> reduction. *Energy & Environmental Science* **2019**, *12* (10), 3001-3014.

46. Singh, M. R.; Kwon, Y.; Lum, Y.; Ager III, J. W.; Bell, A. T., Hydrolysis of Electrolyte Cations Enhances the Electrochemical Reduction of CO<sub>2</sub> over Ag and Cu. *Journal of the American Chemical Society* **2016**, *138* (39), 13006-13012.

47. Resasco, J.; Chen, L. D.; Clark, E.; Tsai, C.; Hahn, C.; Jaramillo, T. F.; Chan, K.; Bell, A. T., Promoter effects of alkali metal cations on the electrochemical reduction of carbon dioxide. *Journal of the American Chemical Society* **2017**, *139* (32), 11277-11287.

48. Bockris, J. O. M.; Nagy, Z., Symmetry factor and transfer coefficient. A source of confusion in electrode kinetics. *Journal of Chemical Education* **1973**, *50* (12), 839.

49. Guidelli, R.; Compton Richard, G.; Feliu Juan, M.; Gileadi, E.; Lipkowski, J.; Schmickler, W.; Trasatti, S., Defining the transfer coefficient in electrochemistry: An assessment (IUPAC Technical Report). In *Pure and Applied Chemistry*, 2014; Vol. 86, p 245.

50. Kresse, G.; Furthmüller, J., Efficiency of ab-initio total energy calculations for metals and semiconductors using a plane-wave basis set. *Computational Materials Science* **1996**, *6* (1), 15-50.

51. Methfessel, M.; Paxton, A. T., High-precision sampling for Brillouin-zone integration in metals. *Physical Review B* **1989**, *40* (6), 3616-3621.

52. Attard, G. A.; Brew, A., Cyclic voltammetry and oxygen reduction activity of the Pt{110}-(1×1) surface. *Journal of Electroanalytical Chemistry* **2015**, *747*, 123-129.

53. Kittel, C.; McEuen, P.; McEuen, P., *Introduction to solid state physics*. Wiley New York: 1996; Vol. 8.

54. Calle-Vallejo, F.; Koper, M. T., Theoretical Considerations on the Electroreduction of CO to C<sub>2</sub> Species on Cu(100) Electrodes. *Angewandte Chemie International Edition* **2013**, *52* (28), 7282-7285.

55. Peterson, A. A.; Nørskov, J. K., Activity descriptors for CO<sub>2</sub> electroreduction to methane on transition-metal catalysts. *The Journal of Physical Chemistry Letters* **2012**, *3* (2), 251-258.

56. Shi, C.; Hansen, H. A.; Lausche, A. C.; Nørskov, J. K., Trends in electrochemical CO<sub>2</sub> reduction activity for open and close-packed metal surfaces. *Physical Chemistry Chemical Physics* **2014**, *16* (10), 4720-4727.

57. Calle-Vallejo, F.; Krabbe, A.; García-Lastra, J. M., How covalence breaks adsorption-energy scaling relations and solvation restores them. *Chemical Science* **2017**, *8* (1), 124-130.
58. Hanselman, S.; Koper, M. T. M.; Calle-Vallejo, F., Computational Comparison of Late Transition Metal (100) Surfaces for the Electrocatalytic Reduction of CO to C<sub>2</sub> Species. *ACS Energy Letters* **2018**, *3* (5), 1062-1067.
59. He, Z.-D.; Hanselman, S.; Chen, Y.-X.; Koper, M. T. M.; Calle-Vallejo, F., Importance of Solvation for the Accurate Prediction of Oxygen Reduction Activities of Pt-Based Electrocatalysts. *The Journal of Physical Chemistry Letters* **2017**, *8* (10), 2243-2246.
60. Clayborne, A.; Chun, H.-J.; Rankin, R. B.; Greeley, J., Elucidation of Pathways for NO Electroreduction on Pt(111) from First Principles. *Angewandte Chemie International Edition* **2015**, *54* (28), 8255-8258.
61. Kurth, S.; Perdew, J. P.; Blaha, P., Molecular and solid-state tests of density functional approximations: LSD, GGAs, and meta-GGAs. *International Journal of Quantum Chemistry* **1999**, *75* (4-5), 889-909.
62. Janthon, P.; Luo, S.; Kozlov, S. M.; Viñes, F.; Limtrakul, J.; Truhlar, D. G.; Illas, F., Bulk Properties of Transition Metals: A Challenge for the Design of Universal Density Functionals. *Journal of Chemical Theory and Computation* **2014**, *10* (9), 3832-3839.
63. Christensen, R.; Hansen, H. A.; Vegge, T., Identifying systematic DFT errors in catalytic reactions. *Catalysis Science & Technology* **2015**, *5* (11), 4946-4949.
64. Hori, Y.; Murata, A.; Takahashi, R.; Suzuki, S., Electrochemical reduction of carbon monoxide to hydrocarbons at various metal electrodes in aqueous solution. *Chemistry Letters* **1987**, *16* (8), 1665-1668.
65. Hori, Y.; Kikuchi, K.; Murata, A.; Suzuki, S., Production of methane and ethylene in electrochemical reduction of carbon dioxide at copper electrode in aqueous hydrogencarbonate solution. *Chemistry Letters* **1986**, *15* (6), 897-898.
66. Hori, Y.; Murata, A.; Takahashi, R., Formation of hydrocarbons in the electrochemical reduction of carbon dioxide at a copper electrode in aqueous solution. *Journal of the Chemical Society, Faraday Transactions 1: Physical Chemistry in Condensed Phases* **1989**, *85* (8), 2309-2326.
67. Kuhl, K. P.; Cave, E. R.; Abram, D. N.; Jaramillo, T. F., New insights into the electrochemical reduction of carbon dioxide on metallic copper surfaces. *Energy & Environmental Science* **2012**, *5* (5), 7050-7059.
68. Kortlever, R.; Shen, J.; Schouten, K.; Calle-Vallejo, F.; Koper, M., Catalysts and reaction pathways for the electrochemical reduction of carbon dioxide. *The journal of physical chemistry letters* **2015**, *6* (20), 4073-4082.
69. Nitopi, S.; Bertheussen, E.; Scott, S. B.; Liu, X.; Engstfeld, A. K.; Horch, S.; Seger, B.; Stephens, I. E. L.; Chan, K.; Hahn, C.; Nørskov, J. K.; Jaramillo, T. F.; Chorkendorff, I., Progress and Perspectives of Electrochemical CO<sub>2</sub> Reduction on Copper in Aqueous Electrolyte. *Chemical Reviews* **2019**, *119* (12), 7610-7672.
70. Hori, Y.; Murata, A.; Takahashi, R.; Suzuki, S., Electroreduction of carbon monoxide to methane and ethylene at a copper electrode in aqueous solutions at ambient temperature and pressure. *Journal of the American Chemical Society* **1987**, *109* (16), 5022-5023.
71. Gattrell, M.; Gupta, N., A review of the aqueous electrochemical reduction of CO<sub>2</sub> to hydrocarbons at copper. *Journal of Electroanalytical Chemistry* **2006**, *594* (1), 1-19.
72. Zheng, Y.; Vasileff, A.; Zhou, X.; Jiao, Y.; Jaroniec, M.; Qiao, S.-Z., Understanding the Roadmap for Electrochemical Reduction of CO<sub>2</sub> to Multi-Carbon Oxygenates and Hydrocarbons on Copper-Based Catalysts. *Journal of the American Chemical Society* **2019**, *141* (19), 7646-7659.

73. Kortlever, R.; Peters, I.; Balemans, C.; Kas, R.; Kwon, Y.; Mul, G.; Koper, M. T. M., Palladium–gold catalyst for the electrochemical reduction of CO<sub>2</sub> to C1–C5 hydrocarbons. *Chemical Communications* **2016**, 52 (67), 10229-10232.
74. Kaneco, S.; Katsumata, H.; Suzuki, T.; Ohta, K., Electrochemical reduction of CO<sub>2</sub> to methane at the Cu electrode in methanol with sodium supporting salts and its comparison with other alkaline salts. *Energy & fuels* **2006**, 20 (1), 409-414.
75. Hori, Y.; Takahashi, R.; Yoshinami, Y.; Murata, A., Electrochemical reduction of CO at a copper electrode. *The Journal of Physical Chemistry B* **1997**, 101 (36), 7075-7081.
76. Schouten, K.; Kwon, Y.; Van der Ham, C.; Qin, Z.; Koper, M., A new mechanism for the selectivity to C1 and C2 species in the electrochemical reduction of carbon dioxide on copper electrodes. *Chemical Science* **2011**, 2 (10), 1902-1909.
77. Wuttig, A.; Liu, C.; Peng, Q.; Yaguchi, M.; Hendon, C. H.; Motobayashi, K.; Ye, S.; Osawa, M.; Surendranath, Y., Tracking a common surface-bound intermediate during CO<sub>2</sub>-to-fuels catalysis. *ACS central science* **2016**, 2 (8), 522-528.
78. Bertheussen, E.; Verdaguer-Casadevall, A.; Ravasio, D.; Montoya, J. H.; Trimarco, D. B.; Roy, C.; Meier, S.; Wendland, J.; Nørskov, J. K.; Stephens, I. E. L.; Chorkendorff, I., Acetaldehyde as an Intermediate in the Electroreduction of Carbon Monoxide to Ethanol on Oxide-Derived Copper. *Angewandte Chemie International Edition* **2016**, 55 (4), 1450-1454.
79. Schouten, K. J. P.; Qin, Z.; Gallent, E. P. r.; Koper, M. T., Two Pathways for the Formation of Ethylene in CO Reduction on Single-Crystal Copper Electrodes. *Journal of the American Chemical Society* **2012**, 134 (24), 9864-9867.
80. Ledezma-Yanez, I.; Gallent, E. P.; Koper, M. T.; Calle-Vallejo, F., Structure-sensitive electroreduction of acetaldehyde to ethanol on copper and its mechanistic implications for CO and CO<sub>2</sub> reduction. *Catalysis Today* **2016**, 262, 90-94.
81. Kim, Y.-G.; Javier, A.; Baricuatro, J. H.; Soriaga, M. P., Regulating the product distribution of CO reduction by the atomic-level structural modification of the Cu electrode surface. *Electrocatalysis* **2016**, 7 (5), 391-399.
82. Pérez-Gallent, E.; Marcandalli, G.; Figueiredo, M. C.; Calle-Vallejo, F.; Koper, M. T., Structure-and Potential-Dependent Cation Effects on CO Reduction at Copper Single-Crystal Electrodes. *Journal of the American Chemical Society* **2017**, 139 (45), 16412-16419.
83. Varela, A. S.; Ju, W.; Reier, T.; Strasser, P., Tuning the catalytic activity and selectivity of Cu for CO<sub>2</sub> electroreduction in the presence of halides. *ACS Catalysis* **2016**, 6 (4), 2136-2144.
84. Schmid, B.; Reller, C.; Neubauer, S. S.; Fleischer, M.; Dorta, R.; Schmid, G., Reactivity of Copper Electrodes towards Functional Groups and Small Molecules in the Context of CO<sub>2</sub> Electro-Reductions. *Catalysts* **2017**, 7 (5), 161.
85. Delacourt, C.; Ridgway, P. L.; Kerr, J. B.; Newman, J., Design of an electrochemical cell making syngas (CO+H<sub>2</sub>) from CO<sub>2</sub> and H<sub>2</sub>O reduction at room temperature. *Journal of The Electrochemical Society* **2008**, 155 (1), B42-B49.
86. De Jesús-Cardona, H.; del Moral, C.; Cabrera, C. R., Voltammetric study of CO<sub>2</sub> reduction at Cu electrodes under different KHCO<sub>3</sub> concentrations, temperatures and CO<sub>2</sub> pressures. *Journal of Electroanalytical Chemistry* **2001**, 513 (1), 45-51.
87. Li, Y.; Chan, S. H.; Sun, Q., Heterogeneous catalytic conversion of CO<sub>2</sub>: A comprehensive theoretical review. *Nanoscale* **2015**, 7 (19), 8663-8683.
88. Seh, Z. W.; Kibsgaard, J.; Dickens, C. F.; Chorkendorff, I.; Nørskov, J. K.; Jaramillo, T. F., Combining theory and experiment in electrocatalysis: Insights into materials design. *Science* **2017**, 355 (6321), ead4998.

89. Handoko, A. D.; Wei, F.; Jenndy; Yeo, B. S.; Seh, Z. W., Understanding heterogeneous electrocatalytic carbon dioxide reduction through operando techniques. *Nature Catalysis* **2018**, *1* (12), 922-934.
90. Pérez-Gallent, E.; Figueiredo, M. C.; Calle-Vallejo, F.; Koper, M. T. M., Spectroscopic Observation of a Hydrogenated CO Dimer Intermediate During CO Reduction on Cu(100) Electrodes. *Angewandte Chemie* **2017**, *129* (13), 3675-3678.
91. Durand, W. J.; Peterson, A. A.; Studt, F.; Abild-Pedersen, F.; Nørskov, J. K., Structure effects on the energetics of the electrochemical reduction of CO<sub>2</sub> by copper surfaces. *Surface Science* **2011**, *605* (15), 1354-1359.
92. Calle-Vallejo, F.; Loffreda, D.; Koper, M. T.; Sautet, P., Introducing structural sensitivity into adsorption–energy scaling relations by means of coordination numbers. *Nature chemistry* **2015**, *7* (5), 403-410.
93. Li, H.; Li, Y.; Koper, M. T.; Calle-Vallejo, F., Bond-making and breaking between carbon, nitrogen, and oxygen in electrocatalysis. *Journal of the American Chemical Society* **2014**, *136* (44), 15694-15701.
94. Tymoczko, J.; Calle-Vallejo, F.; Schuhmann, W.; Bandarenka, A. S., Making the hydrogen evolution reaction in polymer electrolyte membrane electrolyzers even faster. *Nature communications* **2016**, *7*.
95. Calle-Vallejo, F.; Martínez, J. I.; García-Lastra, J. M.; Sautet, P.; Loffreda, D., Fast prediction of adsorption properties for platinum nanocatalysts with generalized coordination numbers. *Angewandte Chemie International Edition* **2014**, *53* (32), 8316-8319.
96. Tang, W.; Peterson, A. A.; Varela, A. S.; Jovanov, Z. P.; Bech, L.; Durand, W. J.; Dahl, S.; Nørskov, J. K.; Chorkendorff, I., The importance of surface morphology in controlling the selectivity of polycrystalline copper for CO<sub>2</sub> electroreduction. *Physical Chemistry Chemical Physics* **2012**, *14* (1), 76-81.
97. Hirunsit, P., Electroreduction of carbon dioxide to methane on copper, copper–silver, and copper–gold catalysts: a DFT study. *The Journal of Physical Chemistry C* **2013**, *117* (16), 8262-8268.
98. Hirunsit, P.; Soodsawang, W.; Limtrakul, J., CO<sub>2</sub> electrochemical reduction to methane and methanol on copper-based alloys: theoretical insight. *The Journal of Physical Chemistry C* **2015**, *119* (15), 8238-8249.
99. Hansen, H.; Shi, C.; Lausche, A.; Peterson, A.; Nørskov, J., Bifunctional Alloys for the Electroreduction of CO<sub>2</sub> and CO. *Physical Chemistry Chemical Physics* **2016**, *18* (13), 9194-9201.
100. Tripkovic, V.; Vanin, M.; Karamad, M.; Björketun, M. r. E.; Jacobsen, K. W.; Thygesen, K. S.; Rossmeisl, J., Electrochemical CO<sub>2</sub> and CO reduction on metal-functionalized porphyrin-like graphene. *The Journal of Physical Chemistry C* **2013**, *117* (18), 9187-9195.
101. Nie, X.; Esopi, M. R.; Janik, M. J.; Asthagiri, A., Selectivity of CO<sub>2</sub> Reduction on Copper Electrodes: The Role of the Kinetics of Elementary Steps. *Angewandte Chemie International Edition* **2013**, *52* (9), 2459-2462.
102. Nie, X.; Luo, W.; Janik, M. J.; Asthagiri, A., Reaction mechanisms of CO<sub>2</sub> electrochemical reduction on Cu (111) determined with density functional theory. *Journal of Catalysis* **2014**, *312*, 108-122.
103. Hussain, J.; Skúlason, E.; Jónsson, H., Computational Study of Electrochemical CO<sub>2</sub> Reduction at Transition Metal Electrodes. *Procedia Computer Science* **2015**, *51*, 1865-1871.
104. Luo, W.; Nie, X.; Janik, M. J.; Asthagiri, A., Facet dependence of CO<sub>2</sub> reduction paths on Cu electrodes. *ACS Catalysis* **2015**, *6* (1), 219-229.

105. Calle-Vallejo, F.; Koper, M. T., Theoretical considerations on the electroreduction of CO to C2 species on Cu (100) electrodes. *Angewandte Chemie* **2013**, *125* (28), 7423-7426.
106. Cheng, T.; Xiao, H.; Goddard, W. A., Nature of the active sites for CO reduction on copper nanoparticles; suggestions for optimizing performance. *Journal of the American Chemical Society* **2017**, *139* (34), 11642-11645.
107. Garza, A.; Bell, A. T.; Head-Gordon, M., On the Mechanism of CO<sub>2</sub> Reduction at Copper Surfaces: Pathways to C<sub>2</sub> Products. *ACS Catalysis* **2018**.
108. Montoya, J. H.; Peterson, A. A.; Nørskov, J. K., Insights into C-C Coupling in CO<sub>2</sub> Electroreduction on Copper Electrodes. *ChemCatChem* **2013**, *5* (3), 737-742.
109. Montoya, J. H.; Shi, C.; Chan, K.; Nørskov, J. K., Theoretical insights into a CO dimerization mechanism in CO<sub>2</sub> electroreduction. *The journal of physical chemistry letters* **2015**, *6* (11), 2032-2037.
110. Abild-Pedersen, F.; Greeley, J.; Studt, F.; Rossmeisl, J.; Munter, T.; Moses, P. G.; Skulason, E.; Bligaard, T.; Nørskov, J. K., Scaling properties of adsorption energies for hydrogen-containing molecules on transition-metal surfaces. *Physical review letters* **2007**, *99* (1), 016105.
111. Calle-Vallejo, F.; Martínez, J.; García-Lastra, J. M.; Rossmeisl, J.; Koper, M., Physical and chemical nature of the scaling relations between adsorption energies of atoms on metal surfaces. *Physical review letters* **2012**, *108* (11), 116103.
112. Jovanov, Z. P.; Hansen, H. A.; Varela, A. S.; Malacrida, P.; Peterson, A. A.; Nørskov, J. K.; Stephens, I. E.; Chorkendorff, I., Opportunities and challenges in the electrocatalysis of CO<sub>2</sub> and CO reduction using bifunctional surfaces: A theoretical and experimental study of Au–Cd alloys. *Journal of Catalysis* **2016**, *343*, 215-231.
113. Hori, Y.; Kikuchi, K.; Suzuki, S., Production of CO and CH<sub>4</sub> in electrochemical reduction of CO<sub>2</sub> at metal electrodes in aqueous hydrogencarbonate solution. *Chemistry Letters* **1985**, *14* (11), 1695-1698.
114. Kuhl, K. P.; Hatsukade, T.; Cave, E. R.; Abram, D. N.; Kibsgaard, J.; Jaramillo, T. F., Electrocatalytic conversion of carbon dioxide to methane and methanol on transition metal surfaces. *Journal of the American Chemical Society* **2014**, *136* (40), 14107-14113.
115. Hori, Y.; Takahashi, I.; Koga, O.; Hoshi, N., Electrochemical reduction of carbon dioxide at various series of copper single crystal electrodes. *Journal of Molecular Catalysis A: Chemical* **2003**, *199* (1), 39-47.
116. Li, Y.; Sun, Q., Recent advances in breaking scaling relations for effective electrochemical conversion of CO<sub>2</sub>. *Advanced Energy Materials* **2016**, *6* (17).
117. Schouten, K. J. P.; Pérez-Gallent, E.; Koper, M. T., The influence of pH on the reduction of CO and CO<sub>2</sub> to hydrocarbons on copper electrodes. *Journal of Electroanalytical Chemistry* **2014**, *716*, 53-57.
118. Murata, A.; Hori, Y., Product selectivity affected by cationic species in electrochemical reduction of CO<sub>2</sub> and CO at a Cu electrode. *Bulletin of the Chemical Society of Japan* **1991**, *64* (1), 123-127.
119. Chen, L. D.; Urushihara, M.; Chan, K.; Nørskov, J. K., Electric field effects in electrochemical CO<sub>2</sub> reduction. *ACS Catalysis* **2016**, *6* (10), 7133-7139.
120. Schouten, K. J. P.; Calle-Vallejo, F.; Koper, M., A step closer to the electrochemical production of liquid fuels. *Angewandte Chemie International Edition* **2014**, *53* (41), 10858-10860.
121. Li, C. W.; Ciston, J.; Kanan, M. W., Electroreduction of carbon monoxide to liquid fuel on oxide-derived nanocrystalline copper. *Nature* **2014**, *508* (7497), 504-507.
122. Verdaguier-Casadevall, A.; Li, C. W.; Johansson, T. P.; Scott, S. B.; McKeown, J. T.; Kumar, M.; Stephens, I. E.; Kanan, M. W.; Chorkendorff, I., Probing the active surface

sites for CO reduction on oxide-derived copper electrocatalysts. *Journal of the American Chemical Society* **2015**, *137* (31), 9808-9811.

123. Lee, S.; Kim, D.; Lee, J., Electrocatalytic Production of C3-C4 Compounds by Conversion of CO<sub>2</sub> on a Chloride-Induced Bi-Phasic Cu<sub>2</sub>O-Cu Catalyst. *Angewandte Chemie* **2015**, *127* (49), 14914-14918.

124. Favaro, M.; Xiao, H.; Cheng, T.; Goddard, W. A.; Yano, J.; Crumlin, E. J., Subsurface oxide plays a critical role in CO<sub>2</sub> activation by Cu (111) surfaces to form chemisorbed CO<sub>2</sub>, the first step in reduction of CO<sub>2</sub>. *Proceedings of the National Academy of Sciences* **2017**, *114* (26), 6706-6711.

125. Liu, C.; Lourenço, M. P.; Hedström, S.; Cavalca, F.; Diaz-Morales, O.; Duarte, H. A.; Nilsson, A.; Pettersson, L. G., Stability and Effects of Subsurface Oxygen in Oxide-Derived Cu Catalyst for CO<sub>2</sub> Reduction. *The Journal of Physical Chemistry C* **2017**, *121* (45), 25010-25017.

126. Garza, A.; Bell, A. T.; Head-Gordon, M., Is Subsurface Oxygen Necessary for the Electrochemical Reduction of CO<sub>2</sub> on Copper? *The Journal of Physical Chemistry Letters* **2018**.

127. Piqué, O.; Viñes, F.; Illas, F.; Calle-Vallejo, F., Elucidating the Structure of Ethanol-Producing Active Sites at Oxide-Derived Cu Electrocatalysts. *ACS Catalysis* **2020**, *10* (18), 10488-10494.

128. Fields, M.; Hong, X.; Nørskov, J. K.; Chan, K., Role of Subsurface Oxygen on Cu Surfaces for CO<sub>2</sub> Electrochemical Reduction. *The Journal of Physical Chemistry C* **2018**, *122* (28), 16209-16215.

129. Liu, S.; White, M. G.; Liu, P., Mechanism of Oxygen Reduction Reaction on Pt(111) in Alkaline Solution: Importance of Chemisorbed Water on Surface. *The Journal of Physical Chemistry C* **2016**, *120* (28), 15288-15298.

130. Tripkovic, V., Thermodynamic assessment of the oxygen reduction activity in aqueous solutions. *Physical Chemistry Chemical Physics* **2017**, *19* (43), 29381-29388.

131. Magnussen, O. M.; Groß, A., Toward an Atomic-Scale Understanding of Electrochemical Interface Structure and Dynamics. *Journal of the American Chemical Society* **2019**, *141* (12), 4777-4790.

132. Gray, C. M.; Saravanan, K.; Wang, G.; Keith, J. A., Quantifying solvation energies at solid/liquid interfaces using continuum solvation methods. *Molecular Simulation* **2017**, *43* (5-6), 420-427.

133. Árnadóttir, L.; Stuve, E. M.; Jónsson, H., The effect of coadsorbed water on the stability, configuration and interconversion of formyl (HCO) and hydroxymethylidyne (COH) on platinum (111). *Chemical Physics Letters* **2012**, *541*, 32-38.

134. Basdogan, Y.; Maldonado, A. M.; Keith, J. A., Advances and challenges in modeling solvated reaction mechanisms for renewable fuels and chemicals. *WIREs Computational Molecular Science* **2020**, *10* (2), e1446.

135. Zhang, X.; Sewell, T. E.; Glatz, B.; Sarupria, S.; Getman, R. B., On the water structure at hydrophobic interfaces and the roles of water on transition-metal catalyzed reactions: A short review. *Catalysis Today* **2017**, *285*, 57-64.

136. Henderson, M. A., The interaction of water with solid surfaces: fundamental aspects revisited. *Surface Science Reports* **2002**, *46* (1), 1-308.

137. Carrasco, J.; Hodgson, A.; Michaelides, A., A molecular perspective of water at metal interfaces. *Nature Materials* **2012**, *11*, 667.

138. Kolb, M. J.; Farber, R. G.; Derouin, J.; Badan, C.; Calle-Vallejo, F.; Juurlink, L. B. F.; Killelea, D. R.; Koper, M. T. M., Double-Stranded Water on Stepped Platinum Surfaces. *Physical Review Letters* **2016**, *116* (13), 136101.

139. Verdaguer, A.; Sacha, G. M.; Bluhm, H.; Salmeron, M., Molecular Structure of Water at Interfaces: Wetting at the Nanometer Scale. *Chemical Reviews* **2006**, *106* (4), 1478-1510.
140. Montemore, M. M.; Andreussi, O.; Medlin, J. W., Hydrocarbon adsorption in an aqueous environment: A computational study of alkyls on Cu(111). *The Journal of Chemical Physics* **2016**, *145* (7), 074702.
141. Schnur, S.; Groß, A., Properties of metal–water interfaces studied from first principles. *New Journal of Physics* **2009**, *11* (12), 125003.
142. Heenen, H. H.; Gauthier, J. A.; Kristoffersen, H. H.; Ludwig, T.; Chan, K., Solvation at metal/water interfaces: An ab initio molecular dynamics benchmark of common computational approaches. *The Journal of Chemical Physics* **2020**, *152* (14), 144703.
143. de Morais, R. F.; Kerber, T.; Calle-Vallejo, F.; Sautet, P.; Loffreda, D., Capturing Solvation Effects at a Liquid/Nanoparticle Interface by Ab Initio Molecular Dynamics: Pt201 Immersed in Water. *Small* **2016**, *12* (38), 5312-5319.
144. Cheng, T.; Xiao, H.; Goddard, W. A., Reaction Mechanisms for the Electrochemical Reduction of CO<sub>2</sub> to CO and Formate on the Cu(100) Surface at 298 K from Quantum Mechanics Free Energy Calculations with Explicit Water. *Journal of the American Chemical Society* **2016**, *138* (42), 13802-13805.
145. Zhang, X.; DeFever, R. S.; Sarupria, S.; Getman, R. B., Free Energies of Catalytic Species Adsorbed to Pt(111) Surfaces under Liquid Solvent Calculated Using Classical and Quantum Approaches. *Journal of Chemical Information and Modeling* **2019**, *59* (5), 2190-2198.
146. Saleheen, M.; Zare, M.; Faheem, M.; Heyden, A., Computational Investigation of Aqueous Phase Effects on the Dehydrogenation and Dehydroxylation of Polyols over Pt(111). *The Journal of Physical Chemistry C* **2019**, *123* (31), 19052-19065.
147. Saleheen, M.; Heyden, A., Liquid-Phase Modeling in Heterogeneous Catalysis. *ACS Catalysis* **2018**, *8* (3), 2188-2194.
148. Marenich, A. V.; Cramer, C. J.; Truhlar, D. G., Universal Solvation Model Based on Solute Electron Density and on a Continuum Model of the Solvent Defined by the Bulk Dielectric Constant and Atomic Surface Tensions. *The Journal of Physical Chemistry B* **2009**, *113* (18), 6378-6396.
149. Mathew, K.; Sundararaman, R.; Letchworth-Weaver, K.; Arias, T. A.; Hennig, R. G., Implicit solvation model for density-functional study of nanocrystal surfaces and reaction pathways. *The Journal of Chemical Physics* **2014**, *140* (8), 084106.
150. Fishman, M.; Zhuang, H. L.; Mathew, K.; Dirschka, W.; Hennig, R. G., Accuracy of exchange-correlation functionals and effect of solvation on the surface energy of copper. *Physical Review B* **2013**, *87* (24), 245402.
151. Scalmani, G.; Frisch, M. J., Continuous surface charge polarizable continuum models of solvation. I. General formalism. *The Journal of Chemical Physics* **2010**, *132* (11), 114110.
152. Gauthier, J. A.; Ringe, S.; Dickens, C. F.; Garza, A. J.; Bell, A. T.; Head-Gordon, M.; Nørskov, J. K.; Chan, K., Challenges in Modeling Electrochemical Reaction Energetics with Polarizable Continuum Models. *ACS Catalysis* **2019**, *9* (2), 920-931.
153. Wang, L.-P.; Van Voorhis, T., A Polarizable QM/MM Explicit Solvent Model for Computational Electrochemistry in Water. *Journal of Chemical Theory and Computation* **2012**, *8* (2), 610-617.
154. Tomasi, J.; Mennucci, B.; Cammi, R., Quantum Mechanical Continuum Solvation Models. *Chemical Reviews* **2005**, *105* (8), 2999-3094.
155. Cramer, C. J.; Truhlar, D. G., A Universal Approach to Solvation Modeling. *Accounts of Chemical Research* **2008**, *41* (6), 760-768.

156. Cossi, M.; Rega, N.; Scalmani, G.; Barone, V., Energies, structures, and electronic properties of molecules in solution with the C-PCM solvation model. *Journal of Computational Chemistry* **2003**, *24* (6), 669-681.
157. Klamt, A., The COSMO and COSMO-RS solvation models. *WIREs Computational Molecular Science* **2011**, *1* (5), 699-709.
158. Klamt, A.; Schüürmann, G., COSMO: a new approach to dielectric screening in solvents with explicit expressions for the screening energy and its gradient. *Journal of the Chemical Society, Perkin Transactions 2* **1993**, (5), 799-805.
159. Klamt, A., Conductor-like Screening Model for Real Solvents: A New Approach to the Quantitative Calculation of Solvation Phenomena. *The Journal of Physical Chemistry* **1995**, *99* (7), 2224-2235.
160. Sinnecker, S.; Rajendran, A.; Klamt, A.; Diedenhofen, M.; Neese, F., Calculation of Solvent Shifts on Electronic g-Tensors with the Conductor-Like Screening Model (COSMO) and Its Self-Consistent Generalization to Real Solvents (Direct COSMO-RS). *The Journal of Physical Chemistry A* **2006**, *110* (6), 2235-2245.
161. Grochowski, P.; Trylska, J., Continuum molecular electrostatics, salt effects, and counterion binding—A review of the Poisson–Boltzmann theory and its modifications. *Biopolymers* **2008**, *89* (2), 93-113.
162. Fattebert, J.-L.; Gygi, F., First-principles molecular dynamics simulations in a continuum solvent. *International Journal of Quantum Chemistry* **2003**, *93* (2), 139-147.
163. Petrosyan, S. A.; Rigos, A. A.; Arias, T. A., Joint Density-Functional Theory: Ab Initio Study of Cr<sub>2</sub>O<sub>3</sub> Surface Chemistry in Solution. *The Journal of Physical Chemistry B* **2005**, *109* (32), 15436-15444.
164. Gunceler, D.; Letchworth-Weaver, K.; Sundararaman, R.; Schwarz, K. A.; Arias, T. J. M.; Science, S. i. M.; Engineering, The importance of nonlinear fluid response in joint density-functional theory studies of battery systems. **2013**, *21* (7), 074005.
165. Sicinska, D.; Paneth, P.; Truhlar, D. G., How Well Does Microsolvation Represent Macrosolvation? A Test Case: Dynamics of Decarboxylation of 4-Pyridylacetic Acid Zwitterion. *The Journal of Physical Chemistry B* **2002**, *106* (10), 2708-2713.
166. Pliego, J. R.; Riveros, J. M., The Cluster–Continuum Model for the Calculation of the Solvation Free Energy of Ionic Species. *The Journal of Physical Chemistry A* **2001**, *105* (30), 7241-7247.
167. Zhang, Q.; Asthagiri, A., Solvation effects on DFT predictions of ORR activity on metal surfaces. *Catalysis Today* **2019**, *323*, 35-43.
168. Steinmann, S. N.; Sautet, P.; Michel, C., Solvation free energies for periodic surfaces: comparison of implicit and explicit solvation models. *Physical Chemistry Chemical Physics* **2016**, *18* (46), 31850-31861.
169. Granda-Marulanda, L. P.; Builes, S.; Koper, M. T. M.; Calle-Vallejo, F., Influence of Van der Waals Interactions on the Solvation Energies of Adsorbates at Pt-Based Electrocatalysts. *ChemPhysChem* **2019**, *20* (22), 2968-2972.
170. Ben-Naim, A., Further Theoretical Background. In *Solvation Thermodynamics*, Ben-Naim, A., Ed. Springer US: Boston, MA, 1987; pp 123-204.
171. Granda-Marulanda, L. P.; Builes, S.; Koper, M. T. M.; Calle-Vallejo, F., Influence of Van der Waals Interactions on the Solvation Energies of Adsorbates at Pt-Based Electrocatalysts. *ChemPhysChem* doi:10.1002/cphc.201900512.
172. Ben-Naim, A., *Solvation thermodynamics*. Springer: Boston, MA, 1987.
173. Calle-Vallejo, F.; F. de Morais, R.; Illas, F.; Loffreda, D.; Sautet, P., Affordable Estimation of Solvation Contributions to the Adsorption Energies of Oxygenates on Metal Nanoparticles. *The Journal of Physical Chemistry C* **2019**, *123* (9), 5578-5582.

174. Shiotari, A.; Sugimoto, Y.; Kamio, H., Characterization of two- and one-dimensional water networks on Ni(111) via atomic force microscopy. *Physical Review Materials* **2019**, *3* (9), 093001.
175. Reichardt, C., Solvatochromic Dyes as Solvent Polarity Indicators. *Chemical Reviews* **1994**, *94* (8), 2319-2358.
176. Reichardt, C.; Welton, T., Empirical Parameters of Solvent Polarity. In *Solvents and Solvent Effects in Organic Chemistry*, 2010; pp 425-508.
177. Cheng, T.; Xiao, H.; Goddard, W. A., Free-Energy Barriers and Reaction Mechanisms for the Electrochemical Reduction of CO on the Cu(100) Surface, Including Multiple Layers of Explicit Solvent at pH 0. *The Journal of Physical Chemistry Letters* **2015**, *6* (23), 4767-4773.
178. Liu, X.; Xiao, J.; Peng, H.; Hong, X.; Chan, K.; Nørskov, J. K., Understanding trends in electrochemical carbon dioxide reduction rates. *Nature Communications* **2017**, *8* (1), 15438.
179. Schouten, K. J. P.; Kwon, Y.; van der Ham, C. J. M.; Qin, Z.; Koper, M. T. M., A new mechanism for the selectivity to C1 and C2 species in the electrochemical reduction of carbon dioxide on copper electrodes. *Chemical Science* **2011**, *2* (10), 1902-1909.
180. Bodenschatz, C. J.; Xie, T.; Zhang, X.; Getman, R. B., Insights into how the aqueous environment influences the kinetics and mechanisms of heterogeneously-catalyzed COH\* and CH<sub>3</sub>OH\* dehydrogenation reactions on Pt(111). *Phys. Chem. Chem. Phys.* **2019**, *21* (19), 9895-9904.
181. Hussain, J.; Jónsson, H.; Skúlason, E., Faraday efficiency and mechanism of electrochemical surface reactions: CO<sub>2</sub> reduction and H<sub>2</sub> formation on Pt(111). *Faraday Discussions* **2016**, *195* (0), 619-636.
182. Nie, X.; Luo, W.; Janik, M. J.; Asthagiri, A., Reaction mechanisms of CO<sub>2</sub> electrochemical reduction on Cu(111) determined with density functional theory. *Journal of Catalysis* **2014**, *312*, 108-122.
183. Hussain, J.; Jónsson, H.; Skúlason, E., Calculations of Product Selectivity in Electrochemical CO<sub>2</sub> Reduction. *ACS Catalysis* **2018**, *8* (6), 5240-5249.
184. Huang, Y.; Handoko, A. D.; Hirunsit, P.; Yeo, B. S., Electrochemical Reduction of CO<sub>2</sub> Using Copper Single-Crystal Surfaces: Effects of CO\* Coverage on the Selective Formation of Ethylene. *ACS Catal* **2017**, *7* (3), 1749-1756.
185. Schouten, K. J. P.; Pérez Gallent, E.; Koper, M. T., Structure sensitivity of the electrochemical reduction of carbon monoxide on copper single crystals. *ACS Catalysis* **2013**, *3* (6), 1292-1295.
186. Ma, M.; Trzeźniewski, B. J.; Xie, J.; Smith, W. A., Selective and Efficient Reduction of Carbon Dioxide to Carbon Monoxide on Oxide-Derived Nanostructured Silver Electrocatalysts. *Angewandte Chemie International Edition* **2016**, *55* (33), 9748-9752.
187. Todoroki, N.; Tei, H.; Tsurumaki, H.; Miyakawa, T.; Inoue, T.; Wadayama, T., Surface Atomic Arrangement Dependence of Electrochemical CO<sub>2</sub> Reduction on Gold: Online Electrochemical Mass Spectrometric Study on Low-Index Au(hkl) Surfaces. *ACS Catalysis* **2019**, *9* (2), 1383-1388.
188. Hoshi, N.; Kato, M.; Hori, Y., Electrochemical reduction of CO<sub>2</sub> on single crystal electrodes of silver Ag(111), Ag(100) and Ag(110). *Journal of Electroanalytical Chemistry* **1997**, *440* (1), 283-286.
189. Akira, M.; Yoshio, H., Product selectivity affected by cationic species in electrochemical reduction of CO<sub>2</sub> and CO at a Cu electrode. *Bulletin of the Chemical Society of Japan* **1991**, *64* (1), 123-127.

190. Grimme, S.; Antony, J.; Ehrlich, S.; Krieg, H., A consistent and accurate ab initio parametrization of density functional dispersion correction (DFT-D) for the 94 elements H-Pu. *The Journal of Chemical Physics* **2010**, *132* (15), 154104.
191. Xiang, K.; Zhu, F.; Liu, Y.; Pan, Y.; Wang, X.; Yan, X.; Liu, H., A strategy to eliminate carbon deposition on a copper electrode in order to enhance its stability in CO<sub>2</sub>RR catalysis by introducing crystal defects. *Electrochemistry Communications* **2019**, *102*, 72-77.
192. Kas, R.; Kortlever, R.; Yilmaz, H.; Koper, M. T. M.; Mul, G., Manipulating the Hydrocarbon Selectivity of Copper Nanoparticles in CO<sub>2</sub> Electroreduction by Process Conditions. *ChemElectroChem* **2015**, *2* (3), 354-358.
193. Song, H.; Im, M.; Song, J. T.; Lim, J.-A.; Kim, B.-S.; Kwon, Y.; Ryu, S.; Oh, J., Effect of mass transfer and kinetics in ordered Cu-mesostructures for electrochemical CO<sub>2</sub> reduction. *Applied Catalysis B: Environmental* **2018**, *232*, 391-396.
194. Argyle, M. D.; Bartholomew, C. H., Heterogeneous catalyst deactivation and regeneration: a review. *Catalysts* **2015**, *5* (1), 145-269.
195. Shi, C.; Chan, K.; Yoo, J. S.; Nørskov, J. K., Barriers of Electrochemical CO<sub>2</sub> Reduction on Transition Metals. *Organic Process Research & Development* **2016**, *20* (8), 1424-1430.
196. Rendón-Calle, A.; Builes, S.; Calle-Vallejo, F., Substantial improvement of electrocatalytic predictions by systematic assessment of solvent effects on adsorption energies. *Applied Catalysis B: Environmental* **2020**, *276*, 119147.
197. Tang, M. T.; Peng, H.; Lamoureux, P. S.; Bajdich, M.; Abild-Pedersen, F., From electricity to fuels: Descriptors for C1 selectivity in electrochemical CO<sub>2</sub> reduction. *Applied Catalysis B: Environmental* **2020**, *279*, 119384.
198. DeWulf, D. W.; Jin, T.; Bard, A. J., Electrochemical and Surface Studies of Carbon Dioxide Reduction to Methane and Ethylene at Copper Electrodes in Aqueous Solutions. *Journal of The Electrochemical Society* **1989**, *136* (6), 1686.
199. Lee, J.; Tak, Y., Electrocatalytic activity of Cu electrode in electroreduction of CO<sub>2</sub>. *Electrochimica Acta* **2001**, *46* (19), 3015-3022.
200. Jermann, B.; Augustynski, J., Long-term activation of the copper cathode in the course of CO<sub>2</sub> reduction. *Electrochimica Acta* **1994**, *39* (11), 1891-1896.
201. Hori, Y.; Konishi, H.; Futamura, T.; Murata, A.; Koga, O.; Sakurai, H.; Oguma, K., "Deactivation of copper electrode" in electrochemical reduction of CO<sub>2</sub>. *Electrochimica Acta* **2005**, *50* (27), 5354-5369.
202. Sun, Z.; Sartin, M. M.; Chen, W.; He, F.; Cai, J.; Chen, Y.-X., Stability of Product Generation during CO Reduction on Copper. *The Journal of Physical Chemistry C* **2019**, *123* (35), 21467-21477.
203. Wuttig, A.; Surendranath, Y., Impurity Ion Complexation Enhances Carbon Dioxide Reduction Catalysis. *ACS Catalysis* **2015**, *5* (7), 4479-4484.
204. Luo, W.; Nie, X.; Janik, M. J.; Asthagiri, A., Facet Dependence of CO<sub>2</sub> Reduction Paths on Cu Electrodes. *ACS Catalysis* **2016**, *6* (1), 219-229.
205. Guidelli, R.; Compton Richard, G.; Feliu Juan, M.; Gileadi, E.; Lipkowski, J.; Schmickler, W.; Trasatti, S., Defining the transfer coefficient in electrochemistry: An assessment (IUPAC Technical Report). *Pure Appl. Chem.* **2014**, *86* (2), 245.
206. Birdja, Y. Y.; Pérez-Gallent, E.; Figueiredo, M. C.; Göttle, A. J.; Calle-Vallejo, F.; Koper, M. T. M., Advances and challenges in understanding the electrocatalytic conversion of carbon dioxide to fuels. *Nature Energy* **2019**, *4* (9), 732-745.
207. Akhade, S. A.; Nidzyn, R. M.; Rostamikia, G.; Janik, M. J., Using Brønsted-Evans-Polanyi relations to predict electrode potential-dependent activation energies. *Catalysis Today* **2018**, *312*, 82-91.